TÉCNICO LISBOA

Development of a Micromachining Centre and Fabrication and Characterization of Watchmaking Parts

Gonçalo de Almeida Domingos

Thesis to obtain the Master of Science Degree in

Materials Engineering

Supervisors: Prof. Alberto Eduardo Morão Cabral Ferro
Prof. Pedro Alexandre Rodrigues Carvalho Rosa

Examination Committee

Chairperson: Prof. Maria Emília da Encarnação Rosa
Supervisor: Prof. Pedro Alexandre Rodrigues Carvalho Rosa
Member of the Committee: Prof. Pedro Miguel Gomes Abrunhosa Amaral

October 2020

Acknowledgements

To my supervisors, Professors Alberto Ferro and Pedro Rosa, for their continued support during my work and for having believed in me and giving me a chance to work on a thesis which encompasses my passion for machine tools and watchmaking.

A special thanks to Francisco Vaz Pato, who shares a similar passion for machines. For his help throughout the development of the machine, for lending his improved encoder for the x-axis and for kindly sponsoring the bearing change for the Proteo headstock. Without him, it would have been much harder to finish this thesis.

An equally special thanks to Pedro Santos, for his good-hearted nature while dealing with my thesis problems, as well as his help during the manufacturing of the necessary parts.

To Afonso Gregório, without whom and our discussions about the results and trials, my thesis would not have been the same.

To Alcino Reis, who always made sure NOF was at my disposal to realize whatever works were needed, and to Diogo, André, Fábio, Flávio and Mr. Zé, who all have great experience working in NOF and kindly shared some of it with me.

To all my colleagues, Victor, Fábio, Miguel, David and João, who made working at M3 more entertaining.

Finally, to my family and my closest friends, in particular Rostolho Salú, who to this day continue to believe in me and in my pursuit of happiness through chasing my passions.

Institutional acknowledgements

This work was supported by FCT, through IDMEC, under LAETA, project UIDB/50022/2020. The project MAMTool entitled “Machinability of Additive Manufactured Parts for Tooling Industry” funded by the Programa Operacional Competitividade e Internacionalização, and Programa Operacional Regional de Lisboa funded by FEDER and National Funds (FCT) is acknowledged (Reference PTDC/EME-EME/31895/2017). Laboratory of Machining and Micro Manufacturing, Instituto Superior Técnico, for proposing the theme of this dissertation and for performing the laboratorial experiments analysed in this work.

Abstract

In mechanical watchmaking, time is measured through the use of an oscillator, composed of the balance wheel and balance staff, whose pivots run on a pair of jeweled bearings. These pivots have characteristic dimensions of around 100 μm, must possess high hardness ($\sim$ 50 HRC), a very fine surface finish ($R_a \sim$ 0.1 μm) and high dimensional accuracy on the diameter (+0 /-3 μm). The goal of this thesis was to improve an existing 5 axis machining centre with a modern CNC controller and a specific electro-mechanical framework for watchmaking research. The first part of this thesis focused on the improvements made to the machining centre, both on its mechanical and metrological front and on the application of a new electronic and control structure. Following these improvements, to simulate the manufacture of the pivots, a series of micro-turning trials were conducted by turning small diameter (between 300 and 100 micron) micro-pins. The trials were designed so that the effect of the operating parameters, depth of cut, feed rate and the presence of lubricant, on the surface finish and dimensional accuracy of the micro-pins could be studied. The results obtained show that the dimensional accuracy is substantially influenced by the metrological characteristics of the machine and the surface finish by the operating parameters, with best results (R_a = 0.240 μm) obtained without lubricant and low depths of cut and feed rates.

Keywords— watchmaking, balance staff, micro-turning, surface finish, R_a, CNC

Resumo

Na relojoaria mecânica, o tempo é medido através do uso de um oscilador, composto pelo balanço e um varão cujos pivôs rodam sobre um par de rolamentos de rubi. Estes pivôs têm dimensões características da ordem de 100 μm, possuem elevada dureza ($\sim$ 50 HRC), um acabamento superficial muito fino (R_a $\sim$ 0,1 μm) e uma alta exactidão dimensional no diâmetro (+0 /-3 μm). O objetivo desta tese foi melhorar um centro de maquinagem de 5 eixos pré-existente com um controlador CNC moderno e uma estrutura eletromecânica especificamente para a pesquisa na área da relojoaria. A primeira parte da tese foca-se nas melhorias realizadas no centro de maquinagem, tanto na sua componente mecânica e metrológica, como na aplicação da nova estrutura eletrónica e de controlo. Após essas melhorias, de forma a simular a fabricação dos pivôs, uma série de ensaios de micro-torneamento foi realizada ao tornear micro-pinos de pequeno diâmetro (entre 300 e 100 μm). Os ensaios foram desenhados de forma a que o efeito dos parâmetros operacionais, profundidade de corte, avanço e a presença de lubrificante, no acabamento superficial e na precisão dimensional dos micro-pinos pudessem ser estudados. Os resultados obtidos mostram que a precisão dimensional é substancialmente influenciada pelos características metrológicas da máquina e o acabamento superficial pelos parâmetros operativos, com melhores resultados (R_a = 0,240 μm) obtidos sem lubrificante e baixos valores de profundidade de corte e avanço.

Palavras chave— relojoaria, micro-torneamento, acabamento superficial, R_a, CNC

Contents

List of Figures

List of Tables

Glossary

$A_{interaction}$ The interaction area during turning operation; a product of a_p and *f*; units of mm^2. 40, 45, 46, 48, 53

I The moment of inertia of a body; its opposition to a torque altering its rotational speed around an axis; units of $kg{\cdot}m^2$. 1

T The oscillating period; the time taken to complete on full oscillation; units of *s*. 1

a_p Depth of cut. A parameter in turning operation, which corresponds to the radial distance that the tool is engaged with the material; units of *mm*. viii, x, xi, 14, 16, 17, 32–34, 37, 39, 42–51, 53–56, 58, 59

f Feed rate. A parameter in turning operation, which corresponds to the axial distance per revolution that the tool is engaged with the material; units of *mm/rev.*. viii, x, xi, 14, 16, 17, 32–34, 39, 42–46, 48–51, 53–59

k The stiffness; the degree to which a body resists deformation by and applied force; units of $\frac{N \cdot m}{\text{rad.}}$. 1

F_c The cutting force, also expressed as F_z; units of *N*. 17, 56, 58

k_s The specific cutting force, an extrinsic property. It is related to the energy required to fuel the processes that take place during metal cutting (fracture, friction and plastic deformation); units of N/mm^2. viii, 56–59

R_a Arithmetic average of the roughness profile of a workpiece; units of μm. iv, vii, x, 14, 16, 17, 32, 38, 43, 44, 46–51, 53–55, 58, 60

r_b The cutting tool nose radius; units of *mm*. viii, 32, 33, 50, 59

r_{edge} The cutting tool edge radius; units of *mm*. 17, 49

1 Introduction

Horology has accompanied humanity throughout its history. From the simple counting of the days to today's optical clocks, which derive their accuracy from narrow bandwidth electronic transitions of atoms, horology kept pace with time and innovation. Still, perhaps due to the great works and innovations of many renowned watchmakers from the past, such as Huygens, Breguet, Arnold, Earnshaw and perhaps the greatest watchmaker of the last century, George Daniels, the mechanical wristwatch, with its infinite intricacy and complexity, and the passion necessary for its development, still excites a new generation about this unique art.

Although the emergence of the portable watch came to be because of the development of the *mainspring* in the 15th century, the main form of energy storage in mechanical watches (even to this day), it was not until the 16th century that the first pocket watches came to exist. Arguably, one of the defining inventions in watchmaking history was the *balance spring*, developed around the 1650s and credited to both Huygens and Hooke, which consists in a finely coiled, hair thin spring which, when connected to the *balance wheel* (fig.1.1a), increased its time regulating characteristics. While the regulating organs before this introduction were simple balance wheels, the interaction between the balance wheel and the balance spring effectively turns them into an harmonic oscillator, with a precisely defined oscillating period (T), dependent on both the balance wheel inertia (I) and the balance spring stiffness (k) through eq.1.1

$$T = 2\pi \left(\sqrt{\frac{I}{k}} \right) \tag{1.1}$$

A typical mechanical watch gear train is shown in fig. 1.1a. The torque stored in the mainspring is transmitted through a series of gears and pinions, from the mainspring barrel, to the center wheel, third wheel, fourth wheel and finally down to the escape wheel. Here, the periodic oscillation of the balance wheel pushes a lever which lets the escape wheel ”escape” one tooth at a time. This in turn releases the mainspring and actuates the whole gear train.

The ratio of gears is designed so that it provides enough torque reduction that gear teeth and shaft pivots (which are progressively more delicate as we go down the gear train) are not over stressed. Also, this gear reduction is advantageous because the fast oscillations of the balance wheel are directly divided into the more slow running second, minute and hour movements.

The effectiveness of a watch as a timekeeper is however not only dependent on the balance wheel. Ideally, this oscillator would remain undisturbed throughout its oscillating cycle, which would ensure that the time taken during one oscillation would remain constant (a characteristic called *isochronism*). However, the balance wheel runs in a cylindrical shaft, called the *balance staff* (shown in fig.1.1b), with two

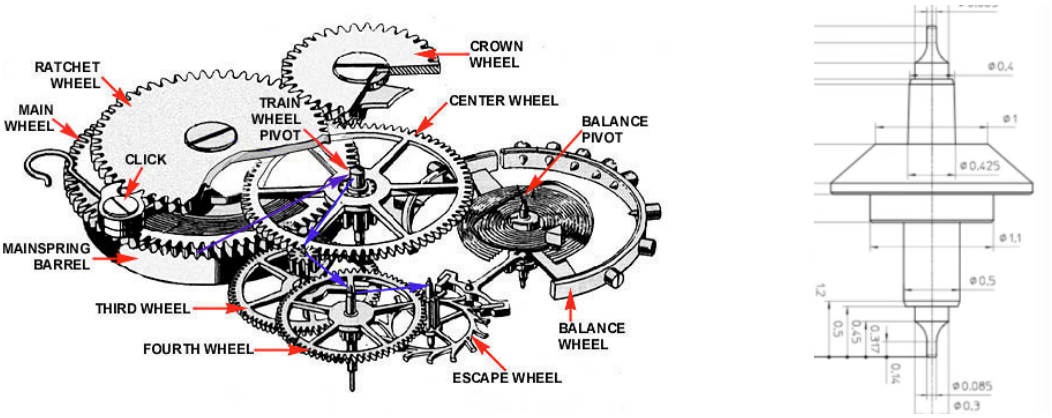

(a) (b)

Figure 1.1: (a) A conventional mechanical watch gear train [21] (b) An example of a balance staff [5]

fine pivots, *balance pivots*, running on a pair of bearings, which contribute to most of its energy dissipation, due to the continuous oscillation and the high frequency stop and start motion. A significant improvement, directly targeted at decreasing this loss of energy and improving timekeeping, was the introduction of jeweled bearings. First adapted for use in balance staff pivots, referring to fig.1.2b, the conical pivot ① was constrained axially (vertical in the figure) by running its *seat* ③ on the *endstone* ⑤. The radial (horizontal in the figure) constrain was accomplished by running the pivot main bearing surface ② against the *pierced jewel* ⑥. Afterwards, a simpler arrangement was adapted to all pinion shaft pivots, seen in fig.1.2a, where a single pierced jewel ② constrains the pivot ① radially and axially through the pivot shaft shoulder ③. While previously, the several parts of a watch ran on metal/metal bearings/shaft, jeweled bearings, made initially from naturals gems, such as ruby, sapphire and diamond, and today from synthetic ruby, grown through a variety of methods, such as the Czochralski or Verneuil method, revolutionized traditional watchmaking. Their advantages reside in their extreme hardness, their dissimilar nature to the metal pivot and the ease of reaching near perfect polishes on the running surface (in the form of the *arithmetic surface roughness*, R_a = 0.025 to 0.05 μm). All these characteristics decrease wear and, due to the extremely fine finish achievable, the coefficient of friction of steel on sapphire is 0.1 - 0.15 [2]. Their breakaway torque is so low, that in one particular case, a jeweled bearing was part of a mechanical torque meter capable of measuring the thrust of a fruit fly [2]. To achieve the minimum breakaway torque, the pivot surface should also have similar surface finish, (R_a = 0.05 to 0.1 μm), while having sufficient hardness ($\approx$ 50 HRC) to increase their useful life [2].

While the pair jewel/hardened steel pivot have a low coefficient of friction, lubrication is still applied to further decrease friction and wear. Lubrication tends to degrade over time, which means that watches have to be serviced at regular intervals. The ”Holy Grail” of watchmaking has always been for the movement to function without lubrication. As of today, with the introduction of novel materials, we are a step closer to reaching that goal.

The requirement that the balance staff pivot must possess high hardness and a high degree of surface finish may seem trivial, since today conventional metal processing machines regularly produce tough to machine, high hardness (up to 70 HRC) components while maintaining a tight shape and dimensional

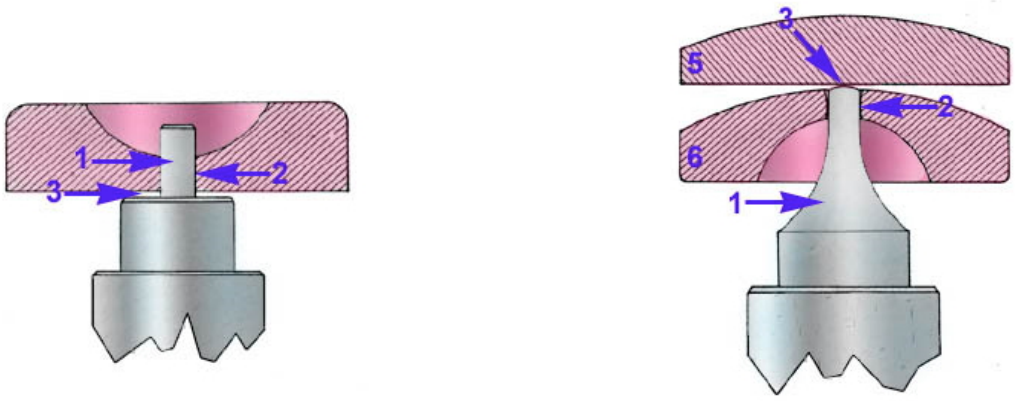

(a) (b)

Figure 1.2: (a) A conventional mechanical watch pinion shaft pivot and (b) balance staff pivot [22]

accuracies ($\approx 2\mu m$) [30]. However, to complicate these requirements, the characteristic dimension of pinion shaft and balance staves pivots are around 200 and 80 - 100 μm, respectively. For the balance staff pivot, that is the characteristic dimension of a human hair.

The purpose of this thesis is to redesign an existing turning machine, with an improved kinematic chain, a modern CNC controller and a specific electro-mechanical framework, and use it to manufacture several micro-pins with diameter ranging from 300 down to 100 μm through micro-turning operations, as a demonstrator of the machine capability to produce parts similar to balance staff pivots and others relevant for watchmaking research. These pins will further be characterized regarding their dimensional accuracy on the diameter and their surface finish in the form of the parameter R_a, resulting from the metrological characteristics of the redesigned machine and the operational parameters during the micro-turning operations.

This thesis is organized in several chapters. Chapter 2 briefly describes the turning machine, from the traditional watchmaker lathe to the modern multi-axis machine, and its the mechanical, metrological and electronic elements. The effect of the turning operation on R_a is also derived, and a review of the state of the art in the manufacturing of micro-pins is made. Chapter 3 describes the construction and particulars of the the existing machining center, Proteo, and details the improvements made to its mechanical, electrical and electronic components, and the implementation of the CNC controller. Chapter 4 details the experimental methodology of the ensuing trials. Chapter 5 presents the metrological characterization of the improved machine, as well as the results obtained in terms of the diameter and surface roughness of the fabricated micro-pins, with a detailed analysis of the results, the development of an hypothesis and subsequent validation through statistical means. An analysis of the forces experienced during the trials is also made. Finally, a conclusion of the entire work is made in Chapter 6.

2 Machine tools for watchmaking

2.1 Watchmaker lathe

Traditionally, balance staff fabrication has always been done on conventional turning machines, called *lathes*.

The lathe has always been critical to the watchmaking art since most critical and functional parts in a watch movement, such as the pinion shafts, balance staves, gears and wheels, are axisymmetric. As such, much of the work of the traditional watchmaker was done at his bench using a *watchmakers lathe*. Several configurations of the watchmaker lathe exist, depending on the type of work that is done.

The watchmaker turns

An uncommon type of lathe, the *watchmaker turns* (fig. 2.1) are dedicated to the finishing of pivots in balance staves or pinion shafts. The turns, also called dead center lathe, does not resemble a modern lathe. Instead, the work is positioned between two hardened steel centres, which have a small recess to accept both ends of the shaft being finished.

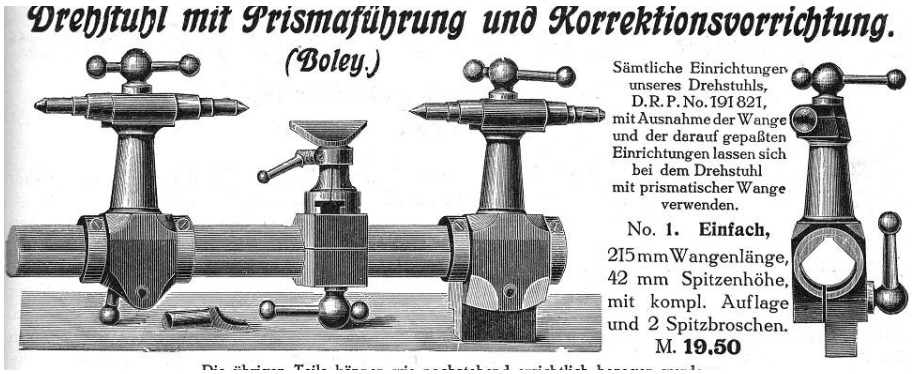

Figure 2.1: A watchmaker turns, from Boley, with an old style bevelled bed, introduced in the 1890s [4]

The watchmaker would position the balance staff or pinion shaft between centres and proceed to remove material and give shape to the pivots ***by hand***, using a finely sharpened graver. In this fashion, when the work was removed from the turns for examination of its dimensions and finish, any necessary adjustment could be made, since re-positioning the the balance staff or pinion shaft between centres can be done without loss of precision, due to *elastic averaging* contact between the shaft and centre mating surfaces. Further, by working between centres, concentricity between both pivots is maintained. Still to this day, on smaller watchmaking workshops and high end manufacturers (low quantity production), the turns are used in finishing balance staff pivots.

The watchmaker lathe

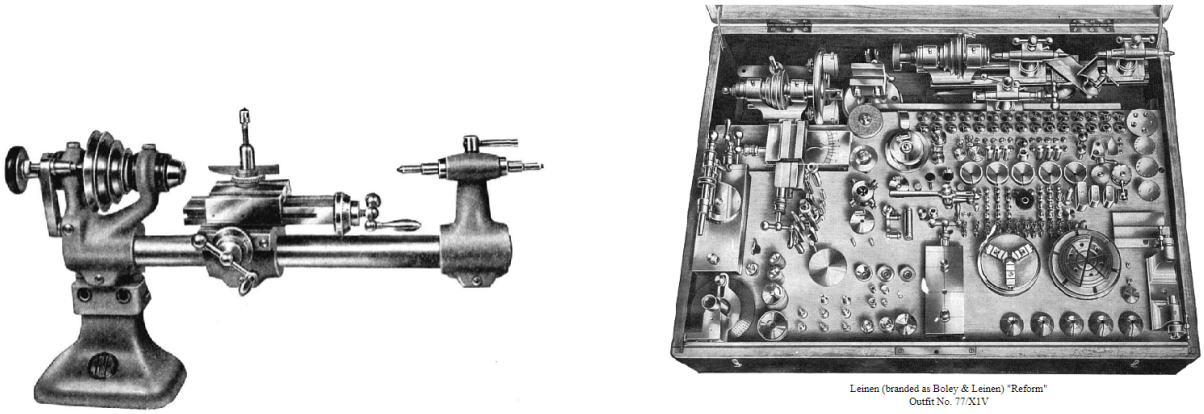

(a) (b)

Figure 2.2: (a) Watchmaker lathe from Bergeon (Model C, with compound slide rest) (b) Leinen WW bed watchmaker lathe, Outfit No. 77/X1V, with an extensive range of accessories [4]

The workhorse of the traditional watchmaker, it came in several variants, from the smaller round bar bed (fig. 2.2a) to the more recent rigid WW style bed. In contrast to the watchmaker turns, holding the workpiece was done by clamping its outside diameter using a *collet*. Although not as accurate as the watchmaker turns when it came to maintaining concentricity between pinion shaft and balance staff pivots, the versatility and simplicity of being able clamp all sorts of workpieces with varying diameters, as well as the improved rigidity were significant improvements for the watchmaker. This style of lathe enabled virtually all parts necessary to produce a complete watch movement, ranging from pinion shafts, gears, balance staves to screws, to be produced, since complete outfits with numerous accessories extended its capabilities beyond that of a simple lathe (fig. 2.2b).

2.2 Modern machine tools

Naturally, with the increasing demand for mass produced and high quality products, the watch industry quickly outgrew the watchmaker lathe. The shift towards automation was a necessity: the large production numbers of watch parts precluded the use of manual operated machines, since they neither afforded the necessary quantities nor *repeatability* in dimension and finish, a necessity in mass produced watch movements. The advances in the machine tool industry were in great part due to the watchmaking industry, and are visible today in the form of highly complex, highly automated machines, which consist of a tight interconnected framework of linear and rotary guidance axes, actuation devices, sensors and control units. One feature that these modern machine tools retain from their predecessors is their versatility. Similar to the watchmaker lathe and its complete outfit of accessories, machine tools today are capable of numerous different operations, through the use of multiple axes and tools. A brief introduction of the several machine systems will be made in the following sections.

2.2.1 Linear and rotary axes

The main element of any machine tool are its linear and rotary guidance elements, which define an *axis*, a direction in 3D space where movement is constrained to occur (X,Y,Z,A,B,C). A machine tool can then be seen as a conjunction of axes, working together to performed a programmed task.

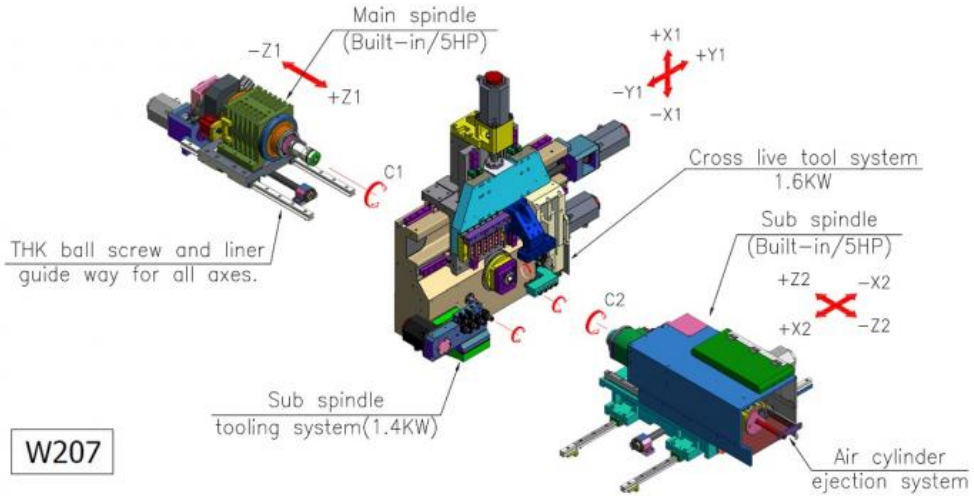

Figure 2.3: An example of a modern machine tool, a 7-axis swiss-style lathe [10]

From fig. 2.3, several of these axes can be identified: (i) the main spindle axes, Z1 and C1: at the left of fig. 2.3, the main spindle defines two axes, the linear Z1 axis and the C1 rotary axis. In this case the main axis carries the work to be machined along the Z1 direction, and rotates it along C1. This provides both turning capabilities, as well as indexing operations to be made; (ii) tooling, X1, Y1 and rotary tooling: at the center of fig. 2.3, this structure carries all the tooling needed to machine the work. It also defines two linear axes, X1 and Y1, which allow for the tool to approach and machine the work carried by the spindle axes (through the X1 axis), as well as to index the several tools mounted, through a sideways shift along Y1. Rotary tooling, at the lower left, is fixed to the main structure; (iii) sub-spindle axes, X2, Z2 and C2: the sub-spindle axes system is essentially similar to the main spindle axes, with the addition of a second linear axis, X2. This allows for secondary operations on the backside of a part. At the heart of these axes reside three major components, which will be introduced in the following sections.

2.2.2 Guidance elements - bearings

Bearings constraint any motion to the required degrees of freedom necessary. Therefore, ultimately, the linear or rotary motion accuracy is dependent on their high degree of quality.

In linear or rotary form, most of them work based on two different principles: **(i)** sliding contact (plain) bearings (fig. 2.5): these are the simplest form of bearings, and find application from general machinery to very accurate machines. In linear variants, their load carrying mechanism is based on the physical contact between two surfaces, which slide in relation to one another, separated by a thin film of lubrication (solid,liquid or mist). In the case of rotary configurations, the main mechanism of load support is not due

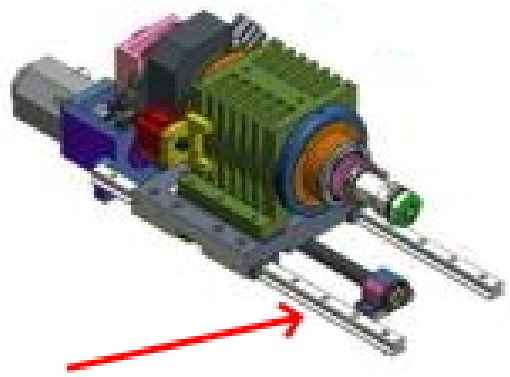

Figure 2.4: The linear bearings (red arrow) of the main spindle axis from fig. 2.3

to contact between surfaces, since shaft and bearing would seize up from the increase in temperature due to the extreme friction forces, but due to the *hydrodynamic* effect.

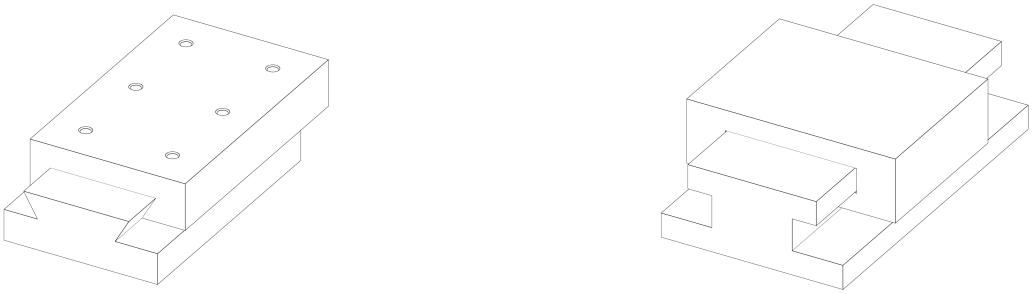

(a) Dovetail guide

(b) Boxway guide

Figure 2.5: Two common linear sliding contact bearings.

The pressure needed to lift of the shaft surface from the journal is generated by dragging the lubricating film through viscous forces into the convergent gap, i.e, the region where shaft and bearing surface are converging to. An applied load forces the shaft out of center and closes the clearance in the same direction of the applied load. This leads to an increase in the pressure in that region which counteracts the load force; **(ii)** rolling element bearings (fig. 2.6): these are based on the rolling of balls or cylindrical rollers along a raceway, which direct their motion. They quickly became a standard in industry due to standardization in their manufacture, ease of replacement when compared to sliding contact bearings and their higher speed allowances. Besides well know rotary configurations, the mainly used linear configuration are the recirculating ball/roller bearings (picture in fig. 2.6a), where balls/rollers are contained within the moving carriage, which are designed with return channels inside it, so that re-circulation is possible, enabling unlimited linear travels.

The choice between these two types of bearings is dependant on numerous factors, such as

- ***Loads applied***: Sliding contact bearings, by virtue of their contact type (large area), can sustain extremely large loads. On the contrary, ball/roller bearings, due to their point/line contact characteristic, offer less load capacity. Preloading rolling elements bearings increases their load capacity, since the deformation of the raceway increases the area of contact;

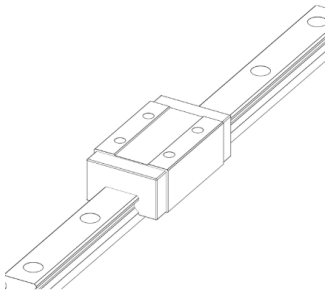

(a) Linear profile rail

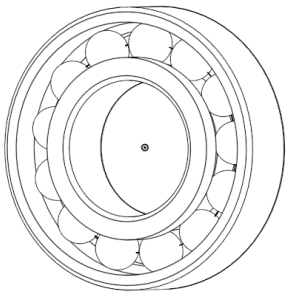

(b) Deep groove ball bearing

Figure 2.6: Typical rolling contact bearing elements used in machine tools

- ***Accuracy***: Depends on the method of finishing. In linear variants, ground sliding contact bearings can achieve straight line accuracies of 5 - 10 μm, while hand finished (scrapped or lapped) can produce submicron accuracy [25]. Rotary plain bearings are easier to produce to exacting standards, since round parts are easier to manufacture than flat ones. In the hydrodynamic regime, they also benefit from an averaging effect of the bore surface imperfections by the closed lubricant pocket effect, which prevents the surfaces from touching. Balls in rolling bearings can be produced to submicron levels of accuracy (in diameter and roundness), although rollers are more difficult. Precision grade linear and rotary rolling bearings are equally capable of submicron accuracies.

- ***Friction***: Sliding contact bearings, even with film lubrication, have high static and dynamic coefficients of friction. At higher sliding velocities, hydrodynamic forces lift up the bearing decreasing the dynamic friction coefficient. Given that static friction coefficient is higher than the dynamic one, during transitions from standstill to moving regimes, a constant moving force will cause a rise in acceleration. This effect is especially noticed during reversal of motion, which can cause reversal and contour errors. This is called the stick slip effect, or stiction. In rotary bearings, if operated in the hydrodynamic region, very low friction is experience (at low speeds). Rolling elements benefit, from their low contact area (depending on their preload), from very low friction coefficients. Dry running, lightly preloaded bearings can have near vanishing friction coefficients (0.0006 - 0.0012), though more commonly around (0.002 - 0.003) [29]. Their similar static and dynamic coefficient of friction means that stiction is barely existent;

- ***Damping***: In sliding contact bearings, due to the large contact areas and the presence of either a lubrication film or solid lubricants, a high damping capacity is achieved due to squeeze film effect: the varying loads lead to a compression of the lubricating layer, which suffers viscous flow, dissipating energy. On the contrary, point/line contact rolling bearings have very low damping;

- ***Resolution***: In sliding contact bearings, resolution is limited since friction coefficients at rest and during motion are different and high, increasing the necessary force for actuation and stiction. Rolling bearings do not suffer from both these effects, and therefore have a theoretically higher resolution;

- ***Wear, lifetime and maintenance***: Sliding contact bearings can have virtually zero to very high

wear rates, depending on load, materials, interface type and type of motion. Linear guideways have poorly predictable wear behaviour. Rotary bearings in the hydrodynamic regime experience virtually no wear; a well know example of this is the case of the hydrodynamic thrust bearing developed by Albert Kingsbury for an hydroelectric turbine unit which had to support a combined load of 225 tons. While previous roller bearings failed after 2 months of use, Kingsbury hydrodynamic thrust bearings, after installation in 1912 and subsequent routine inspections, were predicted to have a lifetime of 1320 *years* [1]. Rolling element bearings, due to low area of contact and low friction, permit maintenance free operation throughout their lifetime (millions of cycles);

- ***Heat***: Sliding contact bearings can suffer from either low or high heat generation dependant on speed of linear or reciprocating movement. Rotary bearings may experience high heat production at high speeds due to high frictional forces which heat up the working fluid. This leads to a reduction in clearance between bearing surface and shaft, which leads to further heating of the fluid, a kind of thermal runaway process. Rolling elements, especially in dry running, produce very little heat;
- ***Power consumption***: None for both during operation (except during periodic lubrication through hydraulic operation in sliding contact bearings)
- ***Limiting speed and acceleration***: Very low for sliding contact bearings. Very high speeds in rolling element bearings, particularly ones with ball elements.

2.2.3 Rotary and linear actuators

The role of the actuating element is to move or rotate an axis along its zero stiffness direction. Rotary actuators, also called motors, have many variants, depending on the type of supply used (DC or AC), on the shape of back electromotive force (sinusoidal or trapezoidal) and type of commands issued to it (analog, through voltage, or digital, through pulses). The simplest of them are DC brushed motors with permanent magnets. The rotating motion is produced by alternating the current direction in the motor coils, which produces a rotating magnetic field. The interaction of this moving magnetic field with the static magnetic field produced by the permanent magnets generates rotary motion. The change in current direction, or *commutation*, is performed mechanically, through a commutator split ring and graphite brushes. Therefore, the speed of these motors is simply controlled by applying different voltage levels to its terminals.

While motors provide direct rotary motion to a rotary axis, to actuate a linear axis, a rotary-to-linear transformation of the motor movement must be made. The simplest elements to perform this function are screws and today, most of screw linear actuators are based on rolling element (ball) contact, and are named ballscrews.

A ballscrew substitutes the sliding contact of conventional screws with the rolling motion of balls inside a ball nut. They have very high efficiencies (up to 90%) due to the very low static/dynamic friction coefficient, which improves an axis linear resolution. Since ballscrews define the accuracy of a linear axis (since their pitch, given in mm/rev., is the reference for the translation of motor rotations to linear

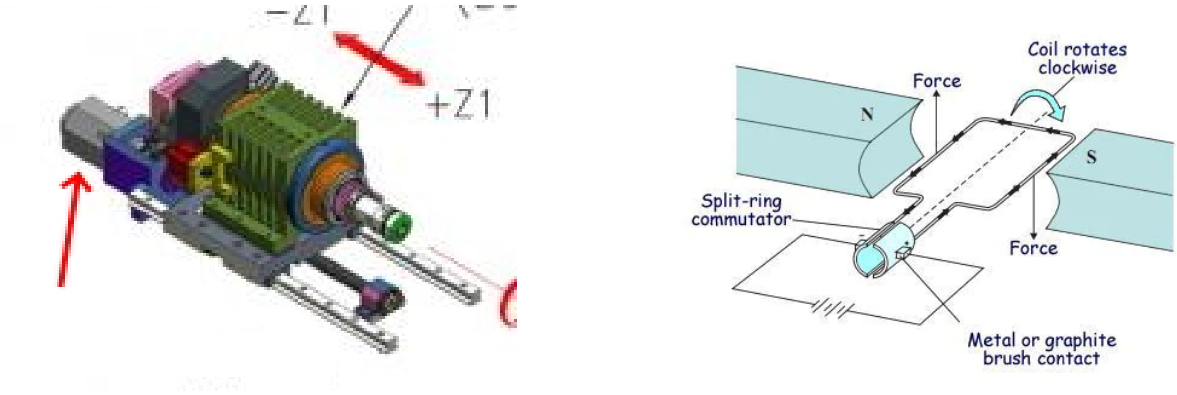

(a) (b)

Figure 2.7: (a) The motor which actuates the linear movement of the main spindle axis (b) A 2-pole brushed motor operation [23].

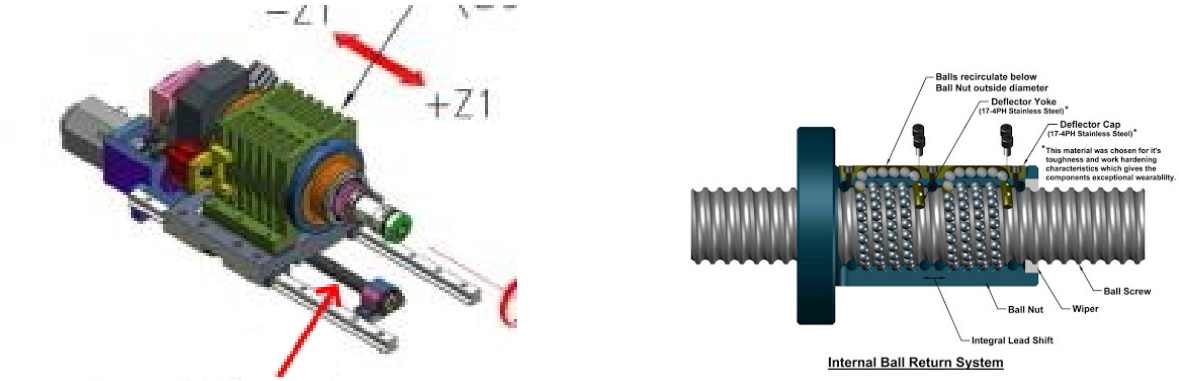

(a) (b)

Figure 2.8: (a) The linear actuator (ballscrew) of the main spindle axis. (b) A closeup of the structure of a ballscrew [6]

displacement), ballscrews are specified with two parameters, which are the fluctuation in regards to the reference travel distance over 300 mm of travel and during the course of a full rotation of the ballscrew (or 2π). In table 2.1, the various accuracy grades of ballscrews are presented.

	Precision ground					Rolled
Accuracy grade	C0	C1	C2	C3	C5	C7
Fluctuation/2π	3	4	5	6	8	-
Fluctuation/300 mm	3.5	5	7	8	18	50

Table 2.1: Accuracy grades of ballscrew (fluctuations in μm) [28]

2.2.4 Electric sensors

While motors and linear actuators comprise a fundamental part of a motion axis, a fundamental characteristic of precision machine tools is that the position of the axes should be *known*. A motor or a ballscrew do not provide positional feedback. This is the job of the encoder. A motor coupled to an encoder is called a *servo* motor, a motor which faithfully reproduces the commands given to it.

Optical encoders

An optical encoder (fig. 2.9b) is based on the principle of counting successive obscured and illuminated areas on a photo-diode, produced when a light source shines through or is reflected from a binary mask (fig. 2.9a). Optical encoders can have digital outputs, either in incremental or absolute forms, or analogue outputs, typically with sine/cosine waves outputs. The following discussion will be limited to digital incremental encoders, the most common type.

(a) (b)

Figure 2.9: (a) Incremental encoder disk, no index track (b) Typical incremental encoder assembly

A typical incremental encoder works as follows: a collimated light source is shone onto a section of the encoder disk (or scale, if linear displacements are to be measured). The encoder disk, which is composed of a number ***N*** of slits (transparent regions), selectively lets light through these.

The phased photo-diode array assembly includes a mask which selects and allows multiple obscured and illuminated regions to reach the photo-diode array. Employing multiple photo-diode sites allows to average out any errors in slit widths and spacing and also increase signal intensity, improving signal-to-noise (SNR) figures.

An electronic stage converts the photo-diode signal into a square wave pulse stream which can be interfaced to common microcontrollers or digital logic, easily enabling displacement measurements (see fig. 2.10b).

To obtain information regarding direction of rotation (or linear travel), a second output must be generated which is 90° out of phase. This is cleverly done by using the multiple outputs of the photo-diode array, which are composed of multiple in-phase and 90° out of phase signals. By analysing which pulse stream goes logic high first, the direction can be determined.

Digital encoder resolution is proportional to N of slits and to diameter of disk (more space for slits). Usually expressed in *bits* or pulses per rev, *PPR*. Typical resolutions range from 8 bits (256 *PPR*) for lower end encoders up to over 30 *bits* (approx. 1 billion PPR) in ultra precision applications [18].

The same encoders also exist in linear formats. These are used extensively in the industry as they provide direct measurement of linear travels, and therefore introduce no errors due to backlash in the actuation devices (motors, leadscrews, ballscrews, pulleys, bearings, etc...). Instead of using a coded disk, a coded linear scale is used. The same working principles apply.

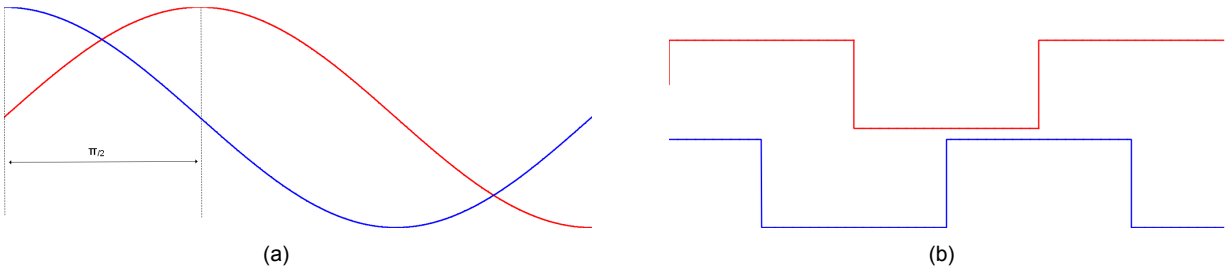

Figure 2.10: (a) In-phase and 90° out of phase signals (sine and cosine, in red and blue respectively) (b) Quadrature signals derived from sine/cosine pairs through zero cross detection

2.2.5 Control framework

Finally, to actuate all these axes and *coordinate* their motion to realize a useful function, there needs to exist a central processing unit, called the *motion coordinator*, which interprets the commanded movements, written either by hand or through *computer aided manufacturing* (CAM) software, which translates part geometry into a general motion plan.

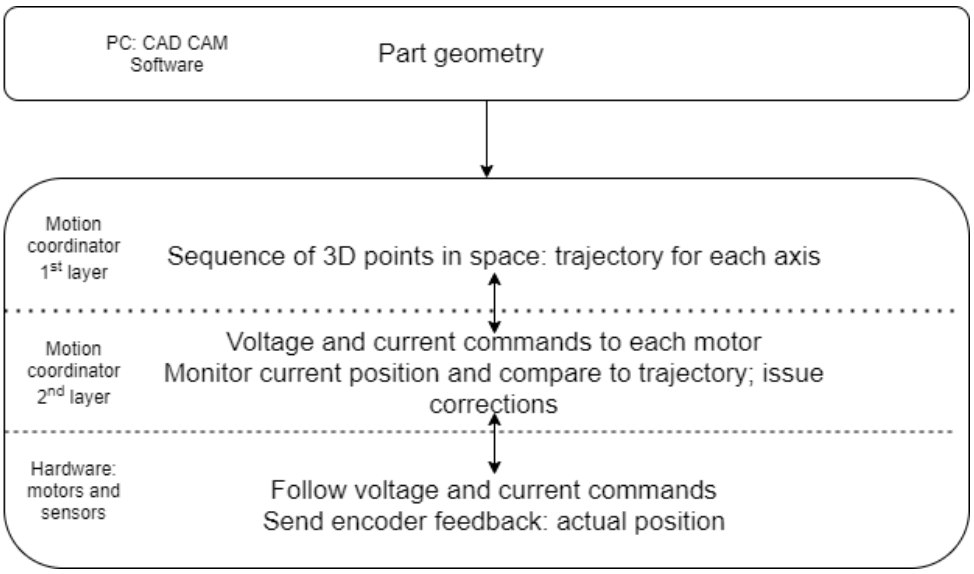

Figure 2.11: Control framework

The control framework has typically two layers: the control board (first layer) and the servo amplifier (second layer). The rough motion plan is, in the first layer of the motion coordinator, converted into a sequence of positions in 3D space separated by a given time increment, a *trajectory*, through which each axis must pass to realize its function. This trajectory is then translated by a second layer of the motion coordinator, into commands which motors can interpret (voltage and current). In the second layer, the feedback from the encoders, the position of each axis, is also an input so that the actual position can be compared to the commanded position, and compensation for any deviation can be issued.

2.3 Metrology: types of errors

Since most machine tools are required to perform some sort of motion in 3-dimensional space to accomplish their task it is fundamental that this motion is well define (or at least well characterized). Inevitably, since manufacturing any element of a machine tool is limited to a degree far off perfection, errors will be present, which will limit its performance. Errors present in elements discussed in the previous sections, such as bearings, motors , mechanical actuators and encoders all trickle down to generate compounded errors. Therefore its important to identify which errors can be present in any kind of machine, and try to recognize which sources cause them, so as to try and avoid them. In the following sections, some of these errors will be presented [12]

2.3.1 Errors associated with linear axes and/or mounting surfaces

Runout in linear axes: straightness and flatness

Errors associated with deviations in a perpendicular direction to a perfect straight line travel of a linear axis (in the XY and XZ planes). That is, a straightness error in a X-axis will produce an error in the Y-axis and vice-versa; a flatness error in a X-axis will produce an error in the Z-axis.

Angular runout in linear axes: Roll, pitch and yaw errors

Errors associated with unwanted rotation of the center point of an axis. Assuming linear motion in the X-direction, roll errors are due to rotation around the X-axis, pitch errors around the Y-axis and yaw errors around the Z-axis.

Squareness errors of linear axes

Errors associated with deviations from perpendicularity between two linear axes. That is, an unwanted change in an axis position due to actuation of another.

Friction and stick slip (stiction) errors

The minimum incremental motion of a linear or rotary axis is limited by their friction: generating a small move might require a force/torque which is smaller than the needed to overcome static friction. Stiction is present in sliding bearings during reversal of motion, and corresponds to the transition from sliding to static friction. The sudden increase in friction might lead to lost motion if the system does not have feedback.

Inertial errors

Errors associated with trying to synchronously accelerate differing or varying masses.

Contouring error

Compounded error from all of the previous errors. Translates into poor following accuracy of a theoretical path along 3-dimensional space.

2.3.2 Errors associated with rotary axes

Out-of-round

Error associated with the deviation from perfect roundness in cylindrical elements (shafts, pin, holes). Difficult to quantify since these errors are local, i.e, they can be different along the major length of the element. Part of contour errors.

Runout

Error associated with the tilting between the principal axis of rotation and the axis of the rotating element (workpiece or tool).

2.3.3 Errors associated with actuation devices

Pitch errors

Errors associated with form deviations along the length of actuation mechanisms such as lead and ball screws, which modify their intended travelled distance per revolution. These can be *progressive*, i.e, the cumulative error increase linearly with each rotation, *periodic*, i.e, the cumulative error has some short range order, for instance, during one revolution of the screw, or *erratic*, where there is no correlation between the cumulative error and the distance travelled.

Backlash errors

Errors associated with the existence of clearance in actuation mechanisms such as screws, necessary for their operation. Upon reversal of movement, the actuating flank of teeth in gears or screws and nuts changes, but during that action no useful motion is produced.

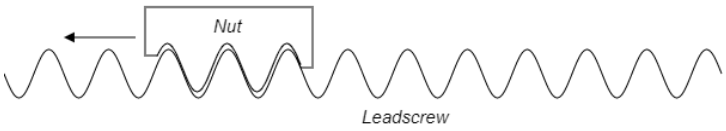

Figure 2.12: Backlash error

2.4 The effect of turning operations on R_a

The R_a theoretical figure, for a conventional turning operating can be calculated easily, when taking into account the conditions of the turning operation, namely, the *depth of cut* a_p and the *feed rate*, f. Fig.

2.13a presents the conditions encountered during this operation.

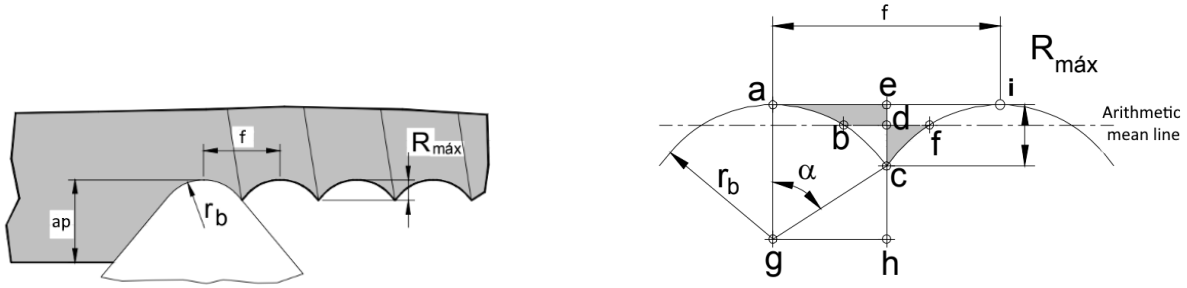

(a) (b)

Figure 2.13: (a) The effect of a_p and f on R_a (b) R_a theoretical derivation

A closer examination at the profile generated by the moving tool, presented in fig.2.13b, reveals the following relationship,

$$\overline{gh}^2 + \overline{ch}^2 = \overline{gc}^2 \tag{2.1}$$

with each of these terms having the following relationships

$$\overline{gh} = \frac{f}{2}\,; \quad \overline{ch} = r_b - R_{\text{máx}}\,; \quad \overline{gh} = r_b \tag{2.2}$$

Substituting in eq. 2.1, we obtain

$$\left(\frac{f}{2}\right)^2 + \left(r_b - R_{\text{máx}}\right)^2 = r_b^2 \tag{2.3}$$

Expanding eq. 2.3, and assuming $R_{\text{máx}}^2 \ll 1$, we obtain

$$R_{\text{máx}} = \frac{f^2}{8r_b} \tag{2.4}$$

The general relationship between $R_{\text{máx}}$ and R_a is not as trivial to obtain. The general formula for R_a

$$R_a = \frac{1}{f}\int_0^f \left|y(x)\right| dx \tag{2.5}$$

Since $y(x)$, the *height of the surface profile* (arcs $\overline{ac}$ and $\overline{ci}$) , is given by

$$y(x) = \begin{cases} \sqrt{r_b^2 - x^2} & \text{if } x \in \left[0, \frac{f}{2}\right] \\ \sqrt{r_b^2 - (x-f)^2} & \text{if } x \in \left]\frac{f}{2}, f\right] \end{cases} \tag{2.6}$$

its integral is not straightforward to compute. However, referring to fig.2.13b, if α is small, then the arcs $\overline{ac}$ and $\overline{ci}$ can be approximated by straight lines, with characteristic equations,

$$y(x) = \begin{cases} \frac{R_{\text{máx}}}{\frac{f}{2}} x & \text{if } x \in \left[0, \frac{f}{2}\right] \\ \frac{R_{\text{máx}}}{\frac{f}{2}} (f - x) & \text{if } x \in \left]\frac{f}{2}, f\right] \end{cases} \tag{2.7}$$

Both are easy to evaluate with eq. 2.5, which equates to

$$R_a = \frac{R_{\text{máx}}}{4} = \frac{f^2}{32 r_b} \tag{2.8}$$

2.5 State of the art in micro-pin turning

On a research level, several works report on the manufacture of micro-pins through micro-turning operations. In [9], the effects of a_p, f, spindle speed and cutting strategy on R_a and dimensional accuracy of 500 μm micro-pins were studied. Using a precision micro-machining machine, with 1μm accuracy and 0.1 μm resolution, and a cemented carbide tool, the results show that R_a has a strong dependence on a_p and f, with R_a decreasing with decreasing a_p. In the optimal operation zone (a_p = 0.2 mm and f = 0.008 mm/rev.) values of 0.33 μm were obtained, while dimensional accuracy varied from - 4 to - 32 μm.

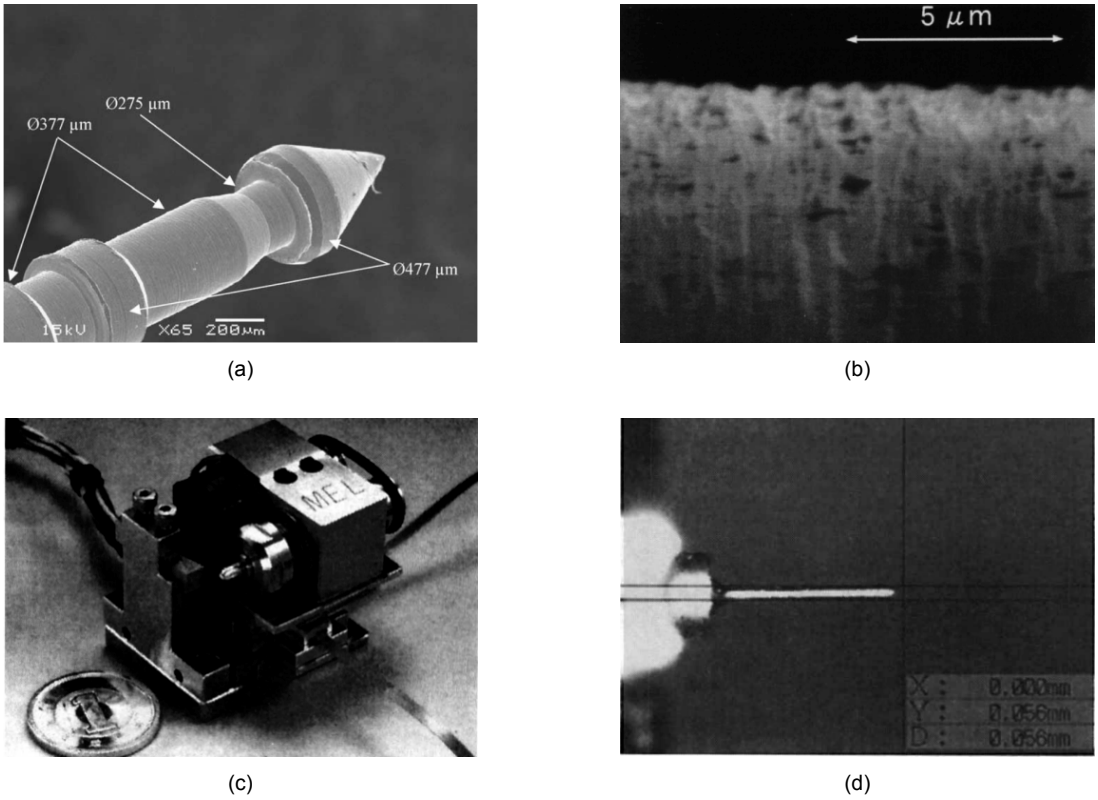

(a) (b)

(c) (d)

Figure 2.14: (a) Compound brass micro-pin [15] (b) Surface asperity of a micro-pin using a diamond tool [8] (c) Developed micro-lathe [14] (d) Micro-pin ($56\mu m$ diameter)

A self-developed, high precision micro-machine was used in [8] for the turning of micro-pins using a micro single point diamond tool. The developed machine, with a spindle runout less than 1 μm and linear axes with a resolution of 4 nm was capable of producing micro-pins with diameter down to 10's μm and R_a below 1 μm (fig. 2.14b), using a_p = 5 μm and f = 0.012 μm/rev. Measured forces were below 10 mN.

In [14], a micro-lathe measuring just 32x28x30 mm and weighing 98 g (fig. 2.14c) was developed, with a linear axis resolution of 62.5 nm. Using a 0.1 mm nose radius diamond tool, micro-pins 600 μm long and with a diameter of $\sim$ 50 μm (fig. 2.14d) were machined with R_a = 0.06 μm in the optimal

operating zone (a_p = 20 μm and f = 0.2 μm/rev.).

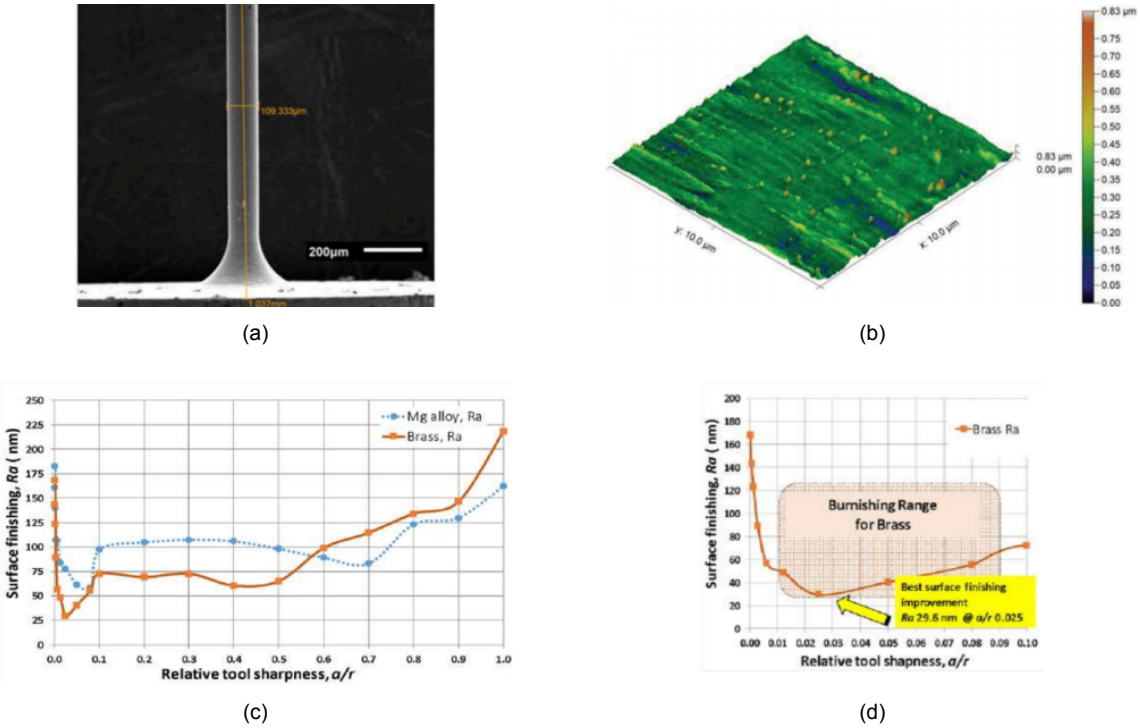

(a) (b)

(c) (d)

Figure 2.15: (a) Brass micro-pin and (b) Corresponding surface topography [24] (c) R_a vs. $\frac{f}{r_{edge}}$ (d) Closeup of burnishing zone for brass [17] [24]

Micro-turning of brass micro-pins was performed in [15] [16], using a submicron accuracy, 0.1 μm resolution machine tool and 0.1 mm nose radius tools. a_p varied between 20 and 5 μm, while f varied between 10 and 3 μm/rev. .Compound micro-pins of 1.76 mm of length (fig. 2.14a) were successfully fabricated, with a smallest diameter of 275 μm. Estimated R_a, in a measuring length of 9.5 μm was at 0.1 μm, while F_c peaked at around 1.5 N.

Brass micro-pins with 100 μm diameter (fig. 2.15a) were micro-turned on a micro-lathe[24] using a 0.2mm nose radius PCD tool and low depths of cut, with an R_a of $0.055 \mu m$ (fig. 2.15b), coincident with lowest cutting forces.

In [7], brass micro-pins of 800 μm diameter and 6 mm long were turned with a cemented carbide tool with 0.1mm nose radius in a precision micro-turning machine, with a_p from 10 to 100 μm and f ranging from 2 to 20 μm/rev. An optimal solution at $a_p \approx 100$ μm and $f \approx 11$ μm/rev. was found where R_a = 0.031 μm. It was also found that a_p was the strongest predictor of R_a.

Recently, the effect of the *cutting tool edge radius* r_{edge} on the surface roughness of micro-turned parts was studied [17]. The governing parameter in defining the surface roughness is found to be the ratio between f and r_{edge}, with three cutting mechanisms identified as shearing at approximately $\frac{f}{r_{edge}}$ = 1, extrusion between $\frac{f}{r_{edge}}$ = 0.1 - 0.5 and burnishing between $\frac{f}{r_{edge}}$ = 0.01 - 0.1. A reduction in R_a of 72.5% and 86.5% was observed when transitioning from shear to extrusion and shear to burnishing, respectively.

3 Micro-machine tool: Proteo

The existing machine was originally designed as small envelope machining centre, capable of realizing synchronized movements in four simultaneous axis, allowing turning operations with gang-tooling and tool orientation, as well as four sided machining operations. Additionally it has a manually indexable fifth axis, which enables further positional milling operations. Figure 3.1 shows the configuration of the machine. The machine coordinates and axes are defined as follows: the headstock ① (to which the workpiece is mounted) is carried by the Z carriage ②, which travels horizontally in the Z direction; the cross slide ③ travels horizontally in the X direction and carries the Y carriage ④; the Y carriage travels in the Y direction and carries the fourth and fifth axis assembly ⑤; this assembly can rotate around the A axis and can be manually positioned such that its axis of rotation is aligned vertically with the Y axis (as in the picture) or aligned horizontally with the Z axis.

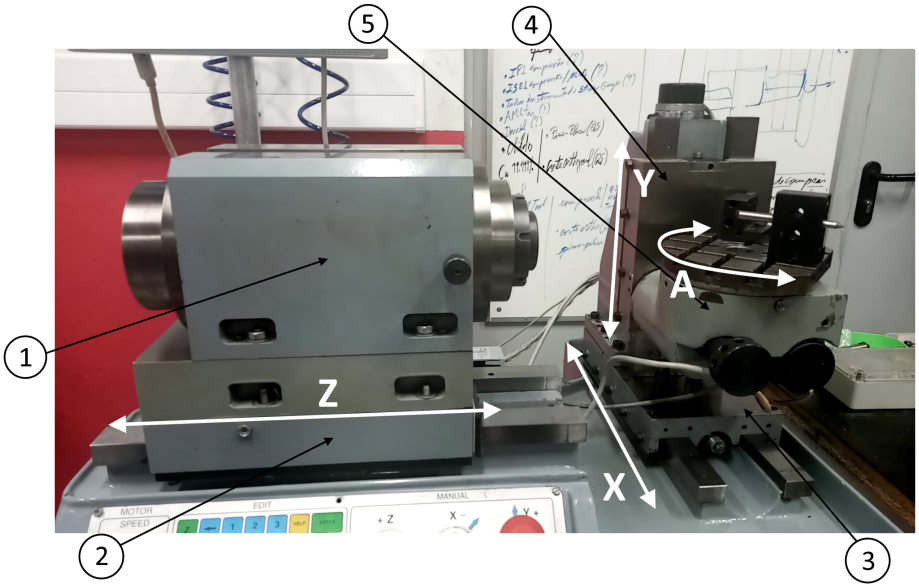

Figure 3.1: Developed micromachining centre

3.1 Micro-machine tool configuration

3.1.1 Linear (X,Y and Z) axes

The general construction of the linear axes is common to all of them, and is shown in fig. 3.2 (a cutaway view of the Z axis). The carriage ⑤ is supported by two hardened steel guideways ④. Their design is such that linear travel is constrained only on one of these hardened steel guideways (the rightmost on fig. 3.2, henceforth referred to as *master rail*) , the other being used only to support vertically the

carriage and giving higher moment load resistance (henceforth referred to as *guide rail*). The carriage is preloaded laterally by a lateral gib (16), which is pushed into the master rail by several screws (14), which force the carriage to take up the clearance available at the master rail. The carriage is preloaded vertically by its own weight and by vertical gibs (3), which close any clearance available. Both types of gibs are made of cast iron. Not seen in fig.

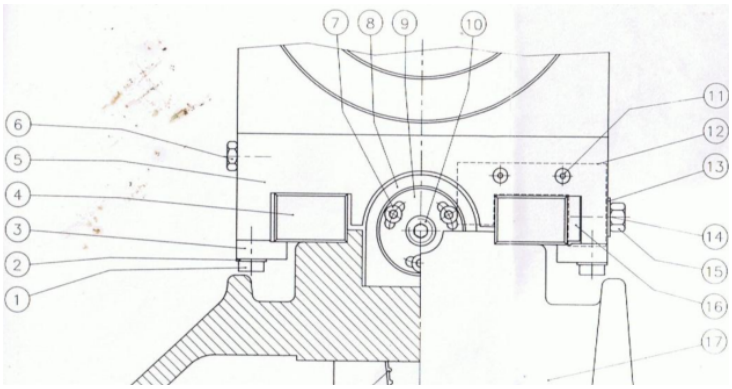

Figure 3.2: X, Y and Z axes sliding bearing guideways (front view) [26]

3.2, both master and guide rails (4) are bolted down to the machine base by multiple bolts and, in the case of the master rail, two reamed blind holes match precision ground dowel pins driven into the base, which provides it some location repeatability upon mounting and higher stiffness.

The lubrication method is manual injection of oil based lubricant through port (6). A channel drilled along the width of the carriage casting feeds two cross drilled holes, each positioned above master and guide rails.

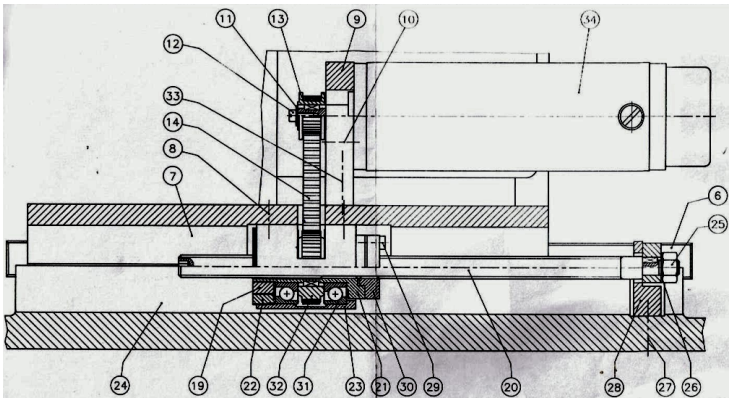

Figure 3.3: Driving mechanism of each axis (lateral view) [26]

The driving mechanism is common to all three linear axis. Schematized in fig. 3.3 for the X axis, a DC servo motor (34) actuates through pulley (14) a toothed wheel (32), which makes part of a shaft (21) containing the ballscrew nut. To guarantee no axial play, the shaft rides on two precision angular contact bearings (31), preloaded axially (to the right) against a shoulder on the assembly casing (23) by a bearing blocking assembly (19) and (22). The whole ballnut assembly is rigidly fixed to the moving carriage (7).

Similarly, the ballscrew (20) is rigidly mounted onto a retaining block (28) by a thread nut (25). The retaining block is in turn fixed to the machine base (24) by two screws (27). Therefore, by rotating the DC

servo motor, the ballnut rotates in the same direction, propelling the moving carriage left or right.

3.1.2 Fourth (A) and fifth axis assembly

The fourth axis can be used both as an indexing or synchronized axis, and is of relatively simple design. It has a table (10) which rides on a precision crossed roller ring (not pictured), directly bolted onto it and to the indexer casting (12). A servo motor (15) drives a 10 toothed pulley (28). This, in turn, drives, through a 20 toothed pulley (25), a ball bearing (20) (23) supported worm shaft (19).

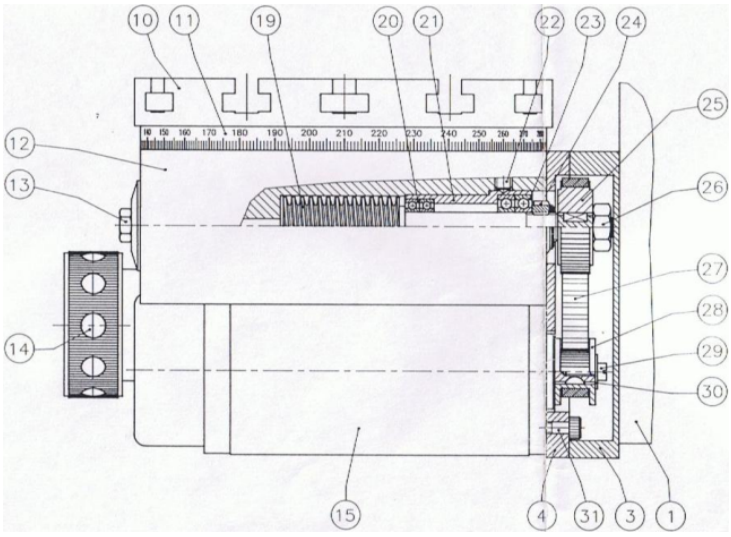

Figure 3.4: Fourth axis construction [26]

The worm mates with a bronze worm wheel (not picture), which is bolted onto the table (10). The mechanism to remove backlash due to radial clearance (in the direction of the paper, referring to fig. 3.4) between worm and worm wheel is somewhat insufficient. The indexer casting three bolt locations for the crossed roller ring are not symmetric, and only at one of the three possible positions does the worm engage with very little rotary play. No further provision to take up more radial clearance is designed into it. After years of use, no longer a backlash free operation is possible.

The fourth and fifth axis assembly can be indexed in the fifth axis manually, by rotating over a ground shaft passing through the casting, which is locked by a knurled knob (14), and mates onto a triangular toothed crown base, which establishes the indexing degree. By unclamping (14), it is possible to tilt the indexer by a predefined amount, allowing to vary the tilt between 0 ° and 90 °. The table has several t-slots included, which make mounting tools quite easy.

3.1.3 Headstock

The headstock of the Proteo houses a W20 collet style spindle riding on matched angular contact bearings at the nose end (22) and a deep groove ball bearing (11) at the back side. The design is characteristic of medium speed, medium loads. The angular contact bearings at the nose provide both axial and radial protection against loads experienced during machining operations, and are tightly preloaded by a precision bearing lock nut (25) against a shoulder on the spindle shaft. The back bearing is arranged to

provide support to the spindle shaft and to add moment support. From fig. 3.5, it is not axially fixed to it, allowing for some thermal growth during operation. It can also be seen that the spindle is powered by a DC motor, with mechanical commutation through graphite brushes (15) and a commutator ring (16), which provide current to the correct coil in the armature (18). The stationary magnetic field is not generated by permanent magnets, but instead with a field coil and magnetic circuit assembly in (17) and (19), respectively.

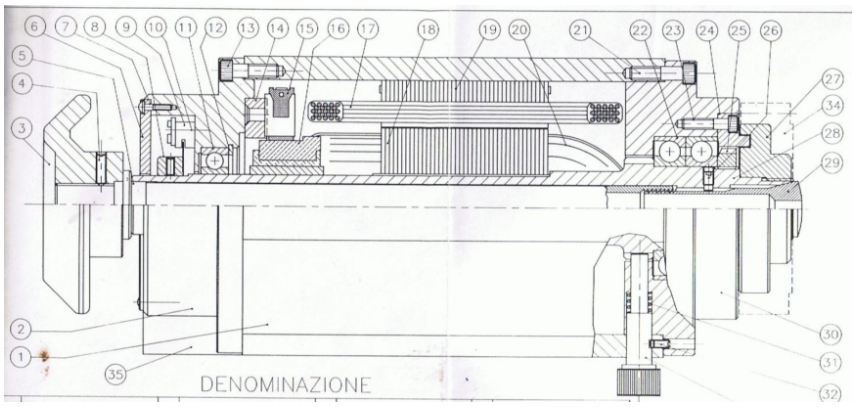

Figure 3.5: Proteo headstock configuration [26]

Provision for cooling of the motor assembly is through injection of compressed air through a side channel in the headstock casting, travelling from the left to the right, which is then directed inwards (downwards, when looking at fig. 3.5) to the armature and field coils region. The lower pressure at the left side due to the venting holes (right side is provided with a labyrinth seal, increasing resistance to airflow) drives the expanding cooling air from the right to the left, cooling the whole spindle and motor assembly.

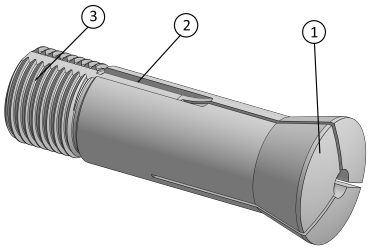

Figure 3.6: W20 collet, detail of number 29 in fig. 3.5

The mechanism to rigidly fix a tool or workpiece to the spindle is simple: the cone present on the rightmost end of the spindle serves as a reference surface. A collet, show in figure 3.6 has a mating cone and is slotted in three positions, 120° apart, producing in effect a three jaw chuck ①. This means that when the collet is pushed tightly to the left by a drawbar (numbered ⑤ in fig. 3.5) clamped to its threaded end ③, its cone is forced into the spindle cone, deflecting the three jaws, which move inwards radially, clamping a tool or workpiece.

The axial slot in the collet ② guides it by riding a pin (26) on the spindle. This effectively prevents rotation of the collet during clamping, which can induced premature failure due to heavy clamping forces and sliding friction. While the spindle is provided with a threaded nose (which usually carries a labyrinth

seal, (27)), enabling using of other chucking devices, such as conventional three, four and six jaw chucks, this should be regarded as the main form of clamping provided by the spindle.

3.2 Mechanical assessment and improvement

The existing machining center required some redesign to bring it to working condition. Evident without any disassembly were the years of use without any proper cleaning, with accumulated grit, dirt and oil on critical and non critical surfaces. Also, upon first detailed inspection, two of the linear axis had severe binding which limited linear travel to below that specified in the manual. It was therefore decided to move on with disassembly.

The whole machining centre was taken apart. First, the original control cabinet was removed. Then, the fourth and fifth axis assembly was removed from the Y-axis linear stage. The headstock was removed from the Z-axis linear stage and the Y-axis from the X-axis linear stage, and both were placed aside for later examination. The machine as it stood now was simply the machine base, with two linear carriages still assembled, the X and Z ones. These were then taken apart, which provided access to the master and guiding rails of both linear axis. The cause for the binding observed during the first inspection was now apparent: years of use without proper oiling and cleaning of the guideways had caused excessive wear on the master rails, which now had their shape severely bowed (> 100 μm), as verified by placing them against a surface plate and using a precision dial indicator. Examining the gibs also showed that, during these years of operation, preload had been adjusted by tightening the gib securing bolts. Given the uneven wear, this produced uneven pressure along the gib, which by now had conformed to the shape of the master rail, and as such presented significant bow. This was unacceptable for any kind of precision operation to be undertaken in the machine. As such, it was decided, given the relative ease of access to a surface grinder and milling machine, to grind the master rail side surfaces for parallelism and produce new gibs.

After this examination, the headstock condition was assessed. Overall, its condition was good. The motor was tested, and proved to be able to run. Needed was a new mechanism for drawbar closing, since the original was pneumatically operated. However, given that this is perhaps the most critical part of the machine, further inspection was left for later. The fourth and fifth axis, after disassembly, did not present any significant problems. They just needed some superficial cleaning. In the following sections, the work done to address these problems is detailed.

3.2.1 Linear axes: grinding the master rails

The hardened steel master rails of both the X and Z axes, which provide the reference surfaces for defining the straightness of travel in their corresponding direction (X and Z), had significant wear in their sides . The top surfaces of both master and guiding rail had some wear, but not enough that it was deemed necessary to grind these surfaces. To do so would also pose a complicated problem: if both top and side surfaces of the master rail were ground, this would mean that absolute squareness should be

maintained between them; furthermore, it would mean that the carriage itself would have to be ground or scraped after the rails where ground and mounted. Both procedures are extremely time consuming and require access either to a profile surface grinder (which would have to be set-up to grind each carriage at a time, with high costs involved) or to highly skilled technicians which know to scrape and check for flatness and squareness.

The grinding operations on the master rails were performed as follows: first, the flatter side of each guideway was identified in a granite surface plate with the aid of a dial indicator indicating to 10 μm (fig. 3.7a). This was the side that was put into contact with the magnetic chuck of the surface grinder, which now acted as a master surface. Upon applying magnetic force, the opposite side of the guideway was checked with the help of an indicator, while moving the transverse axis of the surface grinder. Considerable deflection was measured as the magnetic force was applied and removed along the length of the master rail. If the grinding operation was performed anyways, upon removal of the magnetic force, the guideway would go back to the original state, and consequently both surfaces would not be parallel. Therefore the procedure followed was to find the low spots by successively applying and removing magnetic force, and marking them.

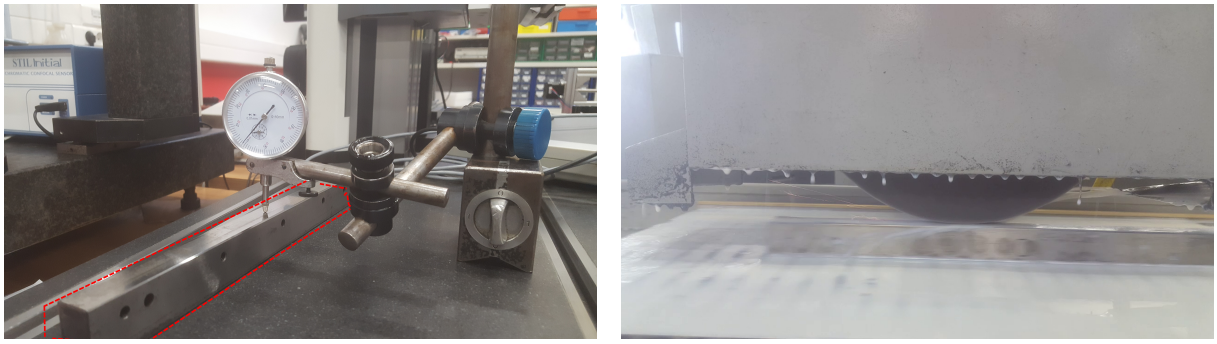

(a) (b)

Figure 3.7: (a) Master rail (circled in red): checking for flatness (b) Grinding the master rail

These low spots were then shimmed with thin gauge stainless foil (in some spots down to 5 μm thick foils) so that deflection was minimized (it was not possible to obtain better than 10 μm of deflection). Considerable time went to trying to find the best shim stock and position of the guideway. The surface of the magnetic chuck was also not perfectly parallel to the transverse travel (as checked with a dial indicator), with significant variation (at places greater than 10 μm of deviation), which was, however, impossible to avoid. A compromise was found, and the grinding operation was performed (fig. 3.7b) until sparking could be observed all across the surface of the master rail. This meant the entire surface was flat. The guideway was removed and repositioned so that the newly ground surface served as the master against the magnetic chuck and the opposite side was the surface to be ground. Grinding took place in the same way, until sparks were observed across the whole surface. The result were two master rails with as close to parallel ($\approx$ 10 μm or 400 mm) sides as the author could accomplish, given the state of the grinder and his operating experience (which was none until this work).

3.2.2 Linear axes: production of preload gibs

The existing cast iron gibs, due to the incorrect preload adjustment through the side screws, coupled with with the high wear, were severely warped. It was therefore necessary to produce new ones.

Some ideas were put on the table, which were better suited to reduce the wear problem compared to the original gibs, since they require limited maintenance: *Teflon* lined gibs, where a high rigidity steel backing layer, with *Teflon* liner would ensure maintenance free operation for some time. Problems include the manufacturing, bonding of the layers and scheduled intervals to replace them; graphite-inserted gib, where again, using an high rigidity backing layer with blind holes drilled, where small pucks of graphite could be bonded to. In essence, similar to commercial offerings such as round oil free bushing. Graphite, as a dry lubricant, does not require periodic oiling, and such a design is easier to manufacture than previous proposal.

Although any of these solutions would be ideal, fabrication is not straightforward. Therefore a compromise was made. In an attempt to alleviate the wear problem in the future, brass was used instead of cast iron. It has better sliding properties against hardened steel, comparable stiffness and machines readily. Bronze, although ideal, was not readily available in bar stock form in the workshop. It is also far easier to machine the geometry, which is advantageous since the author had no previous experience operating a milling machine.

The gibs were produced on a conventional milling machine (fig. 3.8a). First the flat bar stock was saw cut into three blanks on a band saw. To test the machining operation with the available tools, the Z-axis gib was produced first. It was clamped sideways and half of material removal needed for the required height was done. The workpiece was unclamped and rotated 180° and the final stock was removed. This was in an effort to minimize distortion. The ends were then machine with an endmill to produce the required length.

The final operation was face milling to the required thickness. Given the high aspect ratio of the workpiece, this was done in multiple clampings. A small stock removal (up to 0.25mm) was removed at each step, with subsequent 180° reorientation to remove the same thickness from the opposite side. These operations were performed until the desired thickness was achieved. The final piece still had present a small bow (much smaller than the bar stock). To try to circumvent this, it was recommend to first thermal relief the sawed blanks at over 400°C, on a industrial oven available at the laboratory.

This route was followed for the X and Y axes gibs. Both were gang machine to reach the required height and length, using the same procedure of similar stock removal on opposite sides. The last operation, facing, was performed individually on each gib, with alternate shallow facing passes on opposite surfaces, which required multiple clampings, until the required thickness was reached. In the end, although a considerable time was expended on all the operations, no bow was present. All of the gibs are located on the carriage by a simple blind hole, which mates with one of the gib adjusting screws of the carriage. To produce these blind holes, the gibs were clamped onto the table of another conventional milling machine which had digital readout on all the axis. Workpieces were aligned along the X travel of the machine, and the center point of the blind hole was taken using a center finder tool. First the X

(a) (b)

Figure 3.8: (a) Milling of the brass gibs (b) Locating hole drilling

distance was measured by touching the center finder to the edge of the gib, resetting the X ruler to zero, and performing the same procedure for the Y ruler. Then it was a matter of navigating the XY table to the coordinate of the hole. A pilot hole was made (fig. 3.8b) and drilling to the required depth was done with brass drills and with the help of the Z readout.

3.2.3 Headstock: production of drawbar

The original headstock used a pneumatic drawbar mechanism to actuate the opening and closing of the collets. The pneumatic closing assembly however was incomplete, and therefore an adaption of the existing drawbar was made so that manual closing could be used instead. Manual closing is also more suitable, since no provision for automated loading and unloading of tools or workpieces was originally designed into the machine, which limits the usefulness of and automatic drawbar mechanism. Furthermore, rotating mass in the spindle is reduced, improving dynamics, and closing pressure can be adjusted to hold very delicate parts without distortion.

Fabrication of the parts to accomplish the same function was quite straightforward. A spacing ring in aluminium was turned (fig. 3.9a) on the outside diameter so that it matched the spindle outer diameter, and the interior diameter was bored with 0.25mm clearance to the draw bar outside diameter. Its length was designed such that interference between it and the spindle OD was generated when threading the drawbar into the collet. This provides the axial retraction force needed to close collets. To be able to thread the drawbar into the collet, an aluminium disk was face turned to act as a handwheel. It was followed by drilling and boring of a pilot hole in its center. Finally, the pilot hole was threaded M20x1.5, the available thread in the drawbar (fig. 3.9b). The snug fit of the machined thread prevents unscrewing upon actuation. Some bearing retaining compound was also used. The complete drawbar is shown in figs. 3.10a and 3.10b.

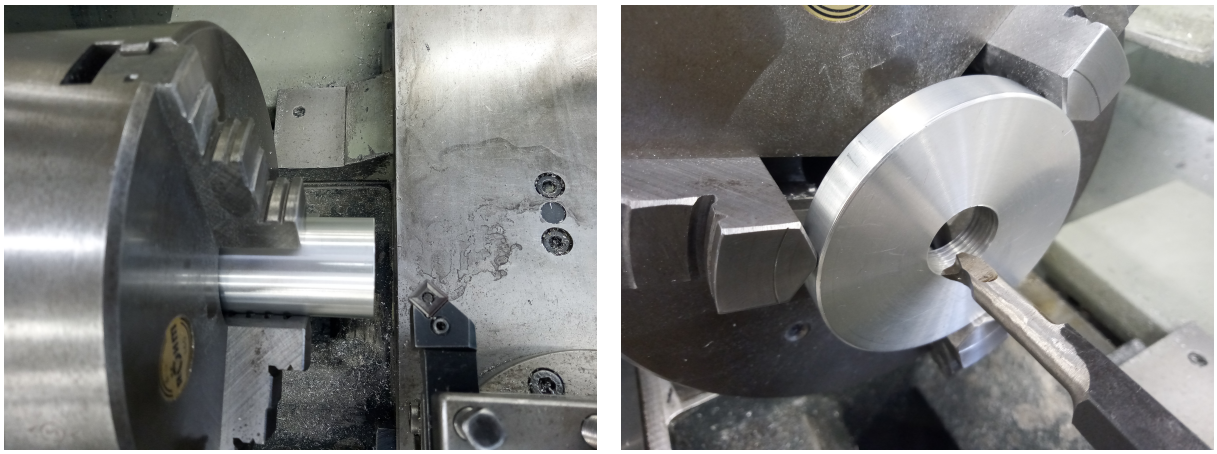

(a) (b)

Figure 3.9: (a) Spacing ring turning (b)Threading the drawbar handwheel

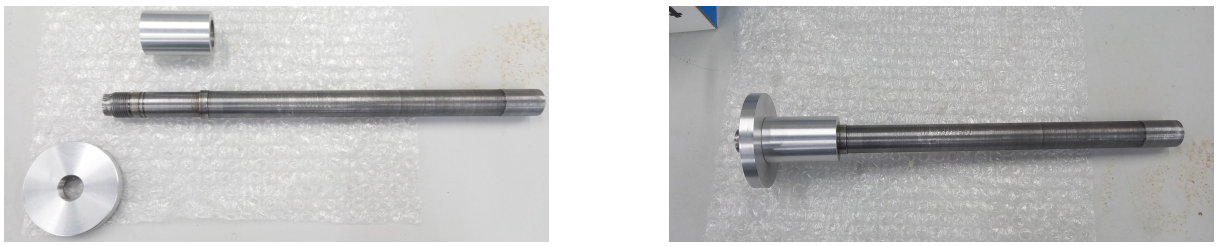

(a) (b)

Figure 3.10: (a) Drawbar disassembled and (b) assembled

3.2.4 Headstock: bearing revision

Since part of the machine was being revised, it was decided that at least the front matched angular contact bearing pair (numbered (22) in fig. 3.5) should be replaced. The back bearing was not replaced since it does not suffer as great a load and does not significantly alter the running characteristics of the spindle.

Ideally, after any bearing change, the spindle cone must be checked for concentricity. Although bearings tolerances are very tight, changing them produces a change in orientation between the cone geometrical axis of rotation and the true axis of rotation determined by the bearings inner ring. Unfortunately, it was not possible to perform a cone regrind since access to a small and precise grinding spindle that could be mounted onto the fourth axis was not available. The bearing substitution was kindly provided by Francisco Vaz Pato, and assembly took place at TAP workshop by experienced mechanics.

3.3 Electronic framework design

What initially prompted this improvement was the failing electronic framework of the existing machining centre. The spindle did not always function properly, nor did some of the linear axis. Most likely, these were due to failing electronics. Also, during disassembly, a major flaw was evident in the main transformer, which powered the whole machine. The toroidal transformer had its insulation fail between

several windings and was beyond repair.

Originally, the Proteo machine was designed as a closed loop system. Position feedback was taken at each of the motor shafts, which gave an indirect reading of the position of each of the linear and rotary axis of the machine. Two configurations were considered for the machine after the retrofit. The first was to maintain the closed loop characteristic, with the original servo motors, and the second was to replace them with steppers, and drive the machine in open loop (without position feedback). It was decided, given that it required zero mechanical rework of the motor supports and coupling to the ball screws, as well as having a potential higher resolution, to keep it as closed loop. Therefore it was necessary to find a suitable CNC controller for the machine, as well as new servo amplifiers and auxiliary equipment.

In A.1, a simplified schematic of the electronic framework is presented.

3.3.1 Servo motors

The original servo motors were in good condition. Preliminary testing showed that the servo motors were running freely, and the original encoder signals (A,B and I) had good wave forms and sufficient SNR to be able to be detected. Again, no original specifications were given in the original manual. From the dimensions, and through comparison with similar motors from a manufacturer (Pittman), it was expected that these would top out at 24V. Given that the DC supply available was capable of 42V, no problem was encountered.

3.3.2 Servo amplifiers

The original electronic cards which controlled the whole machine were highly integrated, contrary to nowadays industrial machine tools, which separate both layers of the motion coordinator (recall section 2.2.5) into two distinct hardware platforms, the CNC controller (1^{st} layer) and the servo amplifiers (2^{nd} layer).

This made it impossible to salvage the original servo amplifiers. Given the limited budget for the entire machine, four servo amplifiers from CNCDrive (model DG4S-16035, in fig. 3.11a) were acquired. These are simple, DC brushed servo motor amplifiers, with quadrature encoder input, and purely positional control. They have a digital Step/Dir interface, which is standardized, and can be interfaced to most hardware control cards. They are responsible for accepting the commanded position from the CNC controller and monitoring and issuing corrections to the actual position of the motors.

3.3.3 CNC controller

The ideal solution would be to implement an industrial grade controller from any of the major CNC controllers manufacturers, such as Fanuc, Siemens or Heidenhain. This would also serve as a good platform for beginners training to operate bigger machines, given this type of controller prevalence. However, the cost of such solutions is prohibitive (the cost of the simplest CNC controller from Siemens, the 808D, for example, is upwards of 7000 euro).

(a) (b)

Figure 3.11: (a) Servo amplifier (b) Mesa CNC controller hardware cards

Therefore, a more cost effective solution was needed. There are several CNC controller software packages, each running on varied hardware, for the hobbyist and enthusiast market. Thee three main ones are Centroid CNC12, Mach4 and LinuxCNC. At the end the choice went to LinuxCNC due to some advantages: unlike the other two, it can be configured for any kind of machine, not only machining centres, which opens up further possibilities for the Proteo machine; it is provided at no cost; it is an open CNC controller, to which any kind of modifications can be made by the end user to implement different functions (in practise, a machine can be reconfigured purely in software to realize a different task); has several advanced features (such as geometrical correction, backlash compensation, ...) and can drive up to 9 axis simultaneously; it supports multiple hardware platforms.

Since the selected servo amplifiers operate through Step/Dir interface, some kind of hardware interface board needs to be used so that these control signals can be generated. While software step generation (generated by the controlling PC, using a standard parallel port) is possible, pulse frequency and synchronization is limited and should be reserved to lower performance applications. Hardware cards that can interface to LinuxCNC are somewhat limited. The most popular cards used with LinuxCNC, and with the best available documentation, are from Mesa, a company which produces several types of cards, based on *field programmable logic arrays*, or FPGAs.

The general architecture of Mesa motion control cards is the following: an FPGA card with an high speed high bandwidth link to the computer CPU (such as PCIe) ensures a low latency communication from the host computer to FPGA hardware. This is absolutely necessary since CNC control needs to be real-time based, and any latency or missed instruction will cause positioning errors. The FPGA is used to generate all the hardware blocks necessary to create and interpret the many signals necessary to actuate motors and read sensors. For instance, to generate the Step/Dir signals that are needed to communicate to the servo amplifiers , hardware pulsed width modulation (PWM) generators are needed. To read high speed (of the order of MHz) quadrature encoders, high speed counters and decoders are necessary.

However, having all the necessary hardware configured in the FPGA motion control card is not sufficient. While internally, CPUs and FPGA operate on logic level signals (1.2V, 3.3V and/or 5V), all of the electronic components necessary, such as the servo amplifiers, sensors and actuators, need to operate

on higher voltage buses. For instance, inputs and outputs are generally powered at +24V, spindle control is done with up to +10V and servo amplifiers need an isolated +5V line. Therefore, a *buffer* card between the FPGA and these electronic components is needed. It should provide isolation, buffer the signals and translate from high to logic level. It also should route them from the convenient screw down terminals to the high speed bus connection between itself and the FPGA card. Cards which have these functions are called *daughter* cards by Mesa.

Since the Proteo machine did not require a large number of inputs and outputs, a simple solution was found which uses just two Mesa cards (fig. 3.11b):

- 5i25: The FPGA card, which connects to the PC through its internal PCIe slot. It provides support for two daughter cards. It has enough logic building block to be able to support up to 10 axis control and thousands of multiplexed (RS422) inputs/outputs (I/O).
- 7i76: A daughter card, which provides terminals for 5 Step/Dir axes, spindle control and encoder and 48 points of I/O. Further, it has an RS-422 interface which can connected to multiple RS-422 enabled daughter cards, increasing almost indefinitely the available I/O pool.

Both cards were within budget, and provided enough expansibility to connect many types of actuator and sensors, if need should arise in the future.

3.3.4 Upgrade of rotary encoder for X axis

Upon assembly of the servo amplifiers, it was necessary to perform tuning of the linear and rotary guideways. It was at this point that the resolution limit of the original encoders was made apparent. While theoretically they could output a resolution of 2 μm per pulse, the fact is that to produce an accurate response to an issued command, a significant number of pulses must be read so that the servo amplifier can plan a movement. In a sense, this problem is the same as trying to measure a length of around 1.111 meter, for instance, with a ruler with a minimum graduation of 1 meter. While the ruler will indicate 1 meter, in fact its accuracy is off 0.111 meters. To obtain good results, resolution should be 10-100x better than the measured variable, as a rule of thumb.

As a side note, the author had the opportunity to attend the 11th Moldplas expo, a technology showing room of machine tools for the mold-making industry. Most of the manufacturers visited (DMG, Hermle, Roeders) reported using linear encoders with 10 *nm* resolution, for a minimum program step of 1 μm.

At 100x the resolution, a minimum incremental motion of 200 μm is obtained for this machine , much higher than is desired for micromachining operations, where depths of cut can be much smaller than this. At this point, an eight times higher count encoder from CUI (fig.3.12a) was tested in the x-axis, which produced a much smoother and accurate motion.

Encoder types and resolution have a significant influence on axes minimum incremental motion

A white paper by Aerotech [13] puts this problem in evidence. Four comparable linear stages are examined in terms of its *minimum incremental motion* (MIM), a term not often stated in datasheets of machine

tool axes. In particular, a comparison is made between a stage with a ballscrew and rotary encoder (as is the configuration of the Proteo machine), with an interpolated resolution of 0.3 nm per encoder count, and a stage with both linear motor and encoders, again with an interpolated resolution of 0.3 nm on the linear scale. While theoretically both stages possess the same resolving power, the MIM of the ballscrew stage is 50 nm (around 167 encoder counts), while the MIM of the linear encoder stage is 1.5 nm (5 encoder counts). The direct measurement of the position, along with the elimination of most of the mechanical inertia and recoil effects from the elasticity of the ballscrew has a marked effect on the MIM. Ideally, the current configuration of the Proteo could be maintained and its MIM and accuracy improved by the addition of a linear scale. It was however outside the budget available to this project.

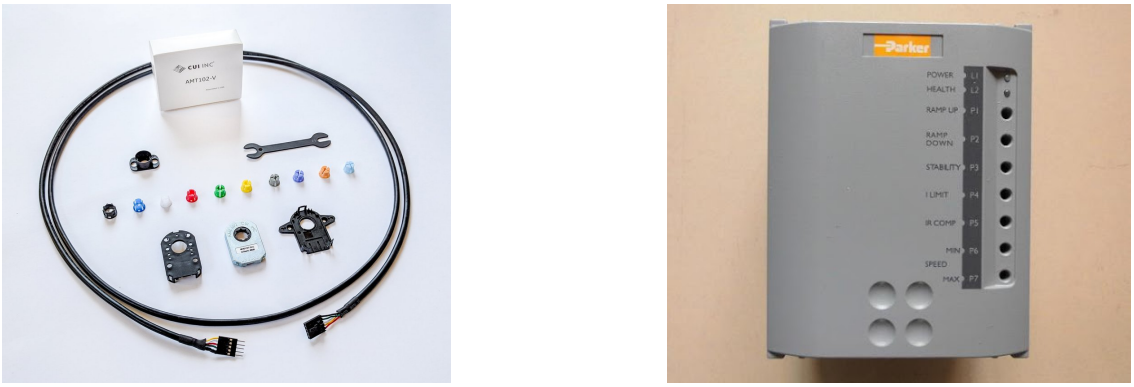

(a) (b)

Figure 3.12: (a) AMT 102 encoder (b) Parker SSD DC drive

3.3.5 Spindle: DC drive

From the manual of the original machine, no specifications were given for both in terms of operating points (voltage and current) for the spindle. By visual inspection, it was found that the spindle motor was DC fed. The original overall power footprint was estimated from the original toroidal transformer, which was rated at 1000W, and powered every circuit, including the spindle DC drive. From there, it was estimated that the spindle should need no more than 250W during normal operation.

A modern DC drive from Parker was acquired (fig.3.12b). However, upon first testings, a significant problem became apparent: due to losses in the windings, an higher current than available from the purchased DC drive is necessary to reach the higher speeds that the spindle was rated for (up to 3000 rpm). This problem cannot effectively be resolved simply by purchasing a more powerful DC drive (which was out of the budget). If an even higher current passes through the armature, an higher heat output is generated. The temperature increase at the back of the spindle as it stands now is moderate (comfortable to touch). Therefore to reach higher speeds, besides a newer DC drive, some new method of cooling must be installed. This design has quite poor cooling performance, as was noticed during testing. Expanding air is free to flow inside the chamber containing the motor assembly, where it can reside for a long period of time. Furthermore the long routing channel for the injection of the air is of rudimentary design.

3.3.6 Home position sensors

Almost all the original homing sensors, necessary to reference the position of the axes, were in good condition, with good signal strength and form. Only the fourth axis sensor was inoperable, since its mounting position promoted the fraying and breaking of its cable.

4 Experimental methodology

4.1 Performance criteria

Balance staves manufactured today, using state of the art machining techniques and machines, satisfy strict design criteria to ensure proper operation over their lifetime. Three important technical specifications for their correct operation are: **(i)** their pivots should have diameters of 85 - 100 μm, with an h4 tolerance (+0/-3μm [3]), and length of similar dimensions [5]; **(ii)** surface roughness values below 0.1 μm R_a [2]; **(iii)** hardness values around 50 HRC for through hardened steel alloys, higher for nitrided staves [2]. To meet all three demands with the developed machine would be unfeasible. The third criteria in particular would demand a significantly more powerful spindle drive than the available. On account of to the current limit described in the previous section, the available cutting power delivered to the spindle unit by the DC drive was verified to be insufficient to produce satisfactory results even when cutting mild steel.

Therefore, the hardness design criteria was dropped, and trials were realized with the following performance criteria: **(i)** geometry was simplified, with pins taking a cylindrical shape with diameter of 300μm, with an h4 tolerance (+0/-3μm), and a length of around 4 mm; **(ii)** their surface roughness R_a should be at most 0.4 μm, ideally closer to 0.1 μm; **(iii)** the material chosen was a free cutting brass alloy (CuZn39Pb3). First, the geometry was changed so that it was simpler to fabricate the micro-pins. Secondly, the target diameter and length were set so that they proved to be sufficiently large that a portable surface roughness meter (Mahr M300) could be used to measure R_a. Thirdly, since the available machine and tools were not designed for micromachining, the surface roughness value R_a was relaxed. Finally, to decrease the chance that trials would fail due to overloading the spindle drive, the material chosen was a free cutting brass alloy.

4.2 Trial conditions

In order to study the effect of the operational parameters on the surface roughness and dimensional accuracy of the micro-pins, several trials were conducted over a region which encompassed different combinations of a_p and f, limited by the manufacturer recommendations for the cutting tool (whose characteristics are presented in table 4.1).

Manufacturer	Type	Coating	Style	Nose angle	r_b (mm)	a_p (mm)	f (mm/rev.)
Palbit	Cemented carbide	Uncoated	Positive (7°)	55°	0.2	0.05 - 3.0	0.05 - 0.12

Table 4.1: Tool characteristics

The tool was selected since it was available at the laboratory; it is a positive style tool, which produces lower cutting forces and lower vibration;it had a low r_b, which produces lower radial forces; and had a low nose angle, which decreases cutting forces and vibration [20].

The trial map (represented in table 4.2) was defined with the following considerations: although the manufacturer states that a_p as low as 0.05 mm are possible, most of the contact area between the workpiece and the tool at values below r_b is made at the nose of the tool, increasing radial forces. When the tool is engaged at depths well over r_b, most of the contact area is along the cutting edge, and the radial forces shift into axial ones [20], which is favourable to the manufacture of small, slender parts. Therefore, a_p was chosen to vary between 0.5 and 2.5 mm, with increment of two r_b (0.4 mm). Further, due to limitations of the machine in achieving very low f, this parameter was selected to vary between 0.005 to 0.160 mm/rev., with a an increment of 2x the previous value.

	a_p (mm)					
	0.5	0.9	1.3	1.7	2.1	2.5
0.005	x	x	x	x	x	x
0.010	x	x	x	x	x	x
0.020	x	x	x	x	x	x
0.040	x	x	x	x	x	x
0.080	x	x	x	x	x	x
0.160	x	x	x	x	x	x
f (mm/rev.)						

Table 4.2: Trial map

The tool was mounted onto the machine and the tool-holder so that its cutting edge was orthogonal to the direction of motion (fig. 4.1), since this decreases the radial force [20] experienced during micro-turning, and as a result, the experienced deflection of the micro-pins.

(a) (b)

Figure 4.1: Tool mounting configuration (a) top view (b) frontal view

Trials were also realized at constant cutting speed, with the spindle speed fixed at 1000 rpm. This proved to be the maximum achievable by trial and error without having to worry about over current tripping the DC drive, invalidating the trial.

4.3 Trial strategy

Since the intention was to fabricate micro-pins, a single cutting pass was planned to be executed over the length of the micro-pin, in order to minimize the deflection and avoid deformation due to excessive forces generated in relation to the micro-pin cross section. In particular, each trial consisted of several steps: first, a small brass cylinder (around 15 mm length) was sawn off the supplied bar. Afterwards, it was chucked in the spindle collet system and facing (transverse motion) and turning (longitudinal motion) operations were realized. This allowed for the correct determination of the cutting tool center point (in the Z and X direction, respectively) in regards to the cylinder. Next, based on the desired depth of cut, the cylinder was turned down to the correct initial diameter

$$D = 0.3 + 2a_p \ (mm) \tag{4.1}$$

and confirmed with a micrometer. Finally, show schematically in fig.4.2, a simple G-Code program was executed, which conducted the final transverse motion to define the required a_p and afterwards fed the tool axially into the cylinder at the specified f. At the end, the tool and was retracted and the pin removed.

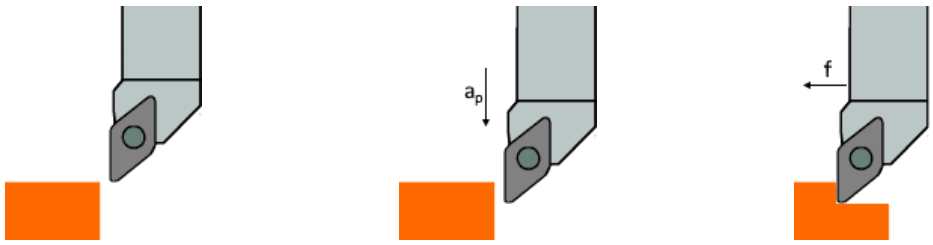

Figure 4.2: Steps in obtaining a micro-pin (a) Final diameter zeroed (b) Defining Transverse motion to define a_p (c) Feeding tool at f

4.4 Measurements

4.4.1 Force

During every trial, forces applied to the micro-pins were measured through the use of a piezo dynamometer from Kistler (typ. 9121) (fig. 4.4a). Due to a dependence of the F_x component on the location of the center of pressure, this force was not monitored. The dynamometer was connected to a charge amplifier, set to the correct scale and gain, with the time constant set at ”long” since we’re interested in quasi-static measurements. Following the charge amplifier, a DAQ from NI (USB-6001) was used to read the analog voltage and this information was captured through a custom developed LabView program. The method to determine the forces was to extract the background information (due to the ”long” time constant, the measured force values tend to drift with time) and subtract it from the original curve (fig. 4.3).

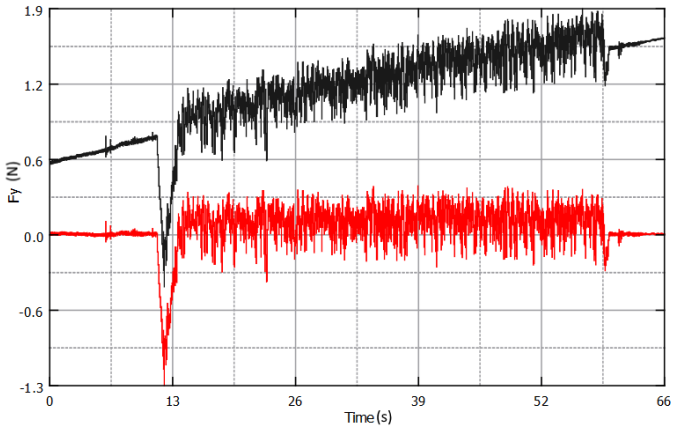

Figure 4.3: Drift and large swings example. At the top, original waveform with long range drift. On the bottom, in red, with the removed trend. Both waveforms still have large high frequency swings.

Then, the average values of F_y and F_z where taken. This was done because both these forces can have large swings of amplitude in a very short time, with significant overshoot (fig. 4.3). These fast voltage swings are not thought to be representative of the forces experienced, but a side effect of the type of sensor used and fast data acquisition rate (5 kHz).

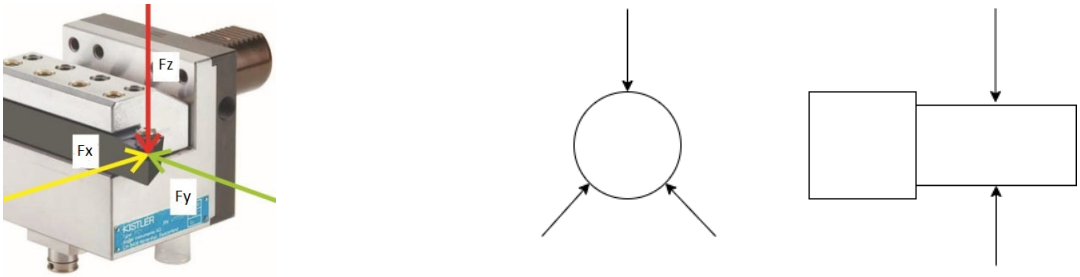

(a) (b)

Figure 4.4: (a) Dynamometer and principal forces decomposition (b) Surface roughness three testing lengths and diameter measurement

4.4.2 Surface roughness and diameter

Each individual pin was mounted on a rotating jig, which allowed for the measurement of the surface roughness on different lines across the machined length. Three measurements were made, each 120° apart. The results were averaged since the evaluation length (2.4 mm) was shorter than desired. Due to its small overall length and diameter, it was extremely difficult to dismount the pin without decreasing its length even more. and, as a result, its diameter was measured in the same mounting jig, with a micrometer (fig. 4.4b).

5 Results and discussion

5.1 Metrological characterization of the machine

After the improvements were made to the existing machining centre, and prior to the micro-pin trials, a simple metrological assessment of the machine was performed. Since only two axis are used during the trials, the Z and X axes, and due to lack of equipment to test all errors detailed in section 2.3, tests were only performed to check for squareness between them (which causes cylindrical pins to become tapered), the positional accuracy of the X axis (which affects the turned diameter) and the runout of the spindle (which affects the turned diameter along the length of the pins).

5.1.1 Squareness error

After assembling the headstock onto the Z axis guide, alignment was performed to decrease coupling errors between the X and Z axis. To check for squareness, a precision ground pin was mounted to the spindle, and a dial test indicator reading to 1 μm to the base of the machine. By positioning the tip of the dial indicator on the ground pin, and performing to and fro motions with the Z axis, the squareness error was determined. By careful alignment of the headstock assembly, the final error measured was 35 μm over 35 mm of travel (visible in fig.5.1, from left to right). Over the length of the micro-pin, 4 mm, this meant a difference of 4 μm, sufficiently low given the magnitude of other errors.

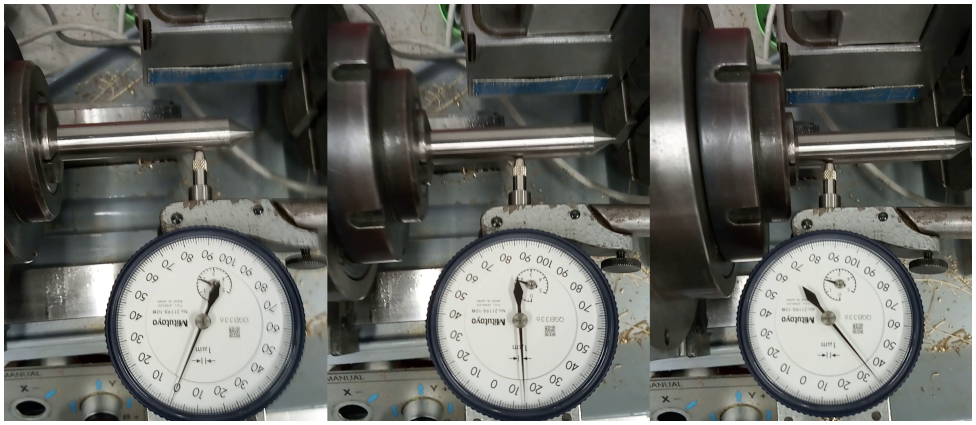

Figure 5.1: Squareness error between z and x axis: left, 0 μm; center, 14 μm, right, 35 μm

5.1.2 Accuracy of the X axis

Since the critical dimension of the micro-pins was their diameter, the X axis of the machine was tested to check for unidirectional accuracy. This is done because only this axis is responsible (given the small

squareness error between the Z and X axis) for any deviations in the micro-pin diameter. A dial test indicator was fixed to the base of the machine and its spindle was positioned perpendicular to the X axis (refer to A.2). By only using machine movements in one direction, any influence of the backlash in the ballscrew is eliminated, and only errors in its pitch and undershoot due to encoder low resolution influence its accuracy. By commanding the X axis to move with similar step sizes a_p to those of table 4.2, the actual measured movement with the dial indicator was averaged over 30 measurements (μ), and the difference $\delta a_p = a_p - \mu$, the undershoot, was calculated and is presented in table 5.1, as is its standard deviation, σ.

	a_p *(mm)*					
	0.5	0.9	1.3	1.7	2.1	2.5
$\delta a_p \pm \sigma$	0.021 $\pm$ 0.009	0.016 $\pm$ 0.004	0.013 $\pm$ 0.004	0.013 $\pm$ 0.003	0.011 $\pm$ 0.003	0.010 $\pm$ 0.002

Table 5.1: The undershoot and its standard deviation in *mm*, rounded to the nearest μm

As expected, as the step size increased, the undershoot in position decreases, as does the variability of this value. This is due to the fact that since larger step sizes contain more physical encoder counts, the control algorithm can plan the response with finer detail, and the trajectory produced follows the theoretical path better.

5.1.3 Runout error

To evaluate the runout figure of the spindle, the dial test indicator was mounted onto the base of the machine, and a precision ground pin mounted in the spindle. By placing the tip of the dial indicator perpendicular to the pin, and rotating the spindle while the Z and X axes were motionless (similar to the setup for measuring the squareness, in fig.5.1), the measured runout was 20 μm at a projected length of 5 mm. No adjustment could be performed to decrease this error.

Closing thoughts on the metrological characteristics of the machine

The results from this section show that the developed machine is not geometrically optimized for the development of micro-precision works. Compared to the machines used in the reviewed literature from section 3 (table 5.2), the presently developed machine is significantly worse on all accounts.

Source	*Spindle speed (rpm)*	*Runout (μm)*	*Linear resolution (μm)*	*Accuracy (μm)*
[8]	3000 - 15000	< 1	0.004	-
[14]	up to 15000	< 1	0.0625	0.2
[15] [16]	2000	-	0.1	< 1
[9]	up to 5000	-	0.1	1
This work	100 - 1500	20	2	21 (worst case)

Table 5.2: Comparison between developed machine and those of literature

Particularly, the linear axis resolution is nearly three orders of magnitude worse than the best documented resolution, with a corresponding effect on achievable accuracy. In all reviewed works, a re-

lationship between linear resolution and accuracy exists, with achievable accuracies of around 10x the available resolution, in agreement to this work. While no account of the squareness error is given in the reviewed literature, the value achieved in this work is acceptable given the defined length of the micro-pins, although for more general work this might not be the case.

5.2 Machining trials: Overall view

Trials were conducted within the operating map defined in the previous chapter (table 4.2) and the results obtained will be presented in the following sections. Cells marked with a cross were trials where either micro-pins could not be fabricated or where no trials were conducted based on previous results. Measured diameters are rounded up to the nearest μm, forces to the nearest 0.01 N and R_a to the nearest 0.001 μm. All micro-pin photographs can be consulted in Appendix A.

5.2.1 Machining trials: Diameter

Table 5.3 contains the measured diameter for each micro-pin fabricated at different levels of a_p and *f*.

	a_p (mm)					
	0.5	0.9	1.3	1.7	2.1	2.5
0.005	324	320	314	309	297	295
0.010	320	325	318	309	295	276
0.020	328	325	322	305	285	275
0.040	330	336	326	327	x	x
0.080	366	371	415	x	x	x
0.160	x	379	x	x	x	x
f (mm/rev.)						

Table 5.3: Measured diameters (μm) for the various fabricated micro-pins

Using the deflection formula for the deflection of a simply supported beam subject to a radial force F_y [11] (fig. 5.2), given by

$$\Delta y = \frac{128 F_y L^3}{6 E \pi D^4} \tag{5.1}$$

the theoretical deflection was obtained (table 5.4), using E = 100 GPa for brass, L = 4 mm and

$$D = 0.3 + 2a_p \text{ (mm)} \tag{5.2}$$

Recalling from chapter 6, where the force measurement methodology was introduced, F_y is taken as the average of the measurement during the trial. The fact is that there are trials where F_y is initially low (due to deflection) and increases until the end of the trial (where deflection is essentially zero). So there is an overestimation of the deflection. This however proves not to be a critical point since the contribution of deflection due to F_y to the deviation in the diameter of the micro-pin is small compared to the following effect.

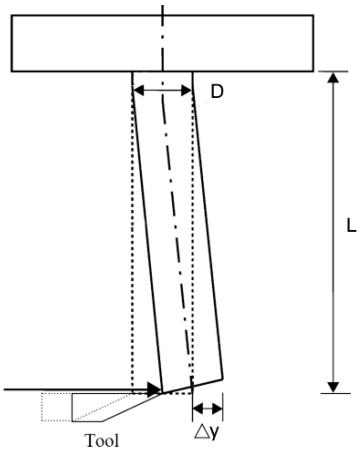

Figure 5.2: Deflection of micro-pins with large overhang

	a_p (mm)						F_y (N)					
	0.5	0.9	1.3	1.7	2.1	2.5	0.5	0.9	1.3	1.7	2.1	2.5
0.005	301	300	300	300	300	300	0.72	-0.24	-0.93	-1.49	-5.89	-6.54
0.010	300	300	300	300	300	300	0	-1.17	-2.18	-2.88	-5.48	- 5.68
0.020	301	301	300	300	300	300	-0.84	-2.70	-4.37	-5.45	-8.69	-10.10
0.040	304	301	301	300	x	x	-2.68	-5.50	-8.52	-11.48	x	x
0.080	310	303	301	x	x	x	-6.81	-11.48	-16.24	x	x	x
0.160	x	305	x	x	x	x	x	-22.75	x	x	x	x
f (mm/rev.)												

Table 5.4: Calculated diameters (μm) accounting for deflection and measured radial force F_y

In section 5.1.2, on the metrological characterization of the machine regarding the accuracy of the X axis, since the machine undershoots the targeted a_p, the final diameter is also affected by this lack of accuracy (recall eq. 5.2). The true turned diameter, due to this effect, can increase by up to two times the *instantaneous* undershoot, that is, the undershoot of the specific trial. The values presented in section 5.1.2 are the *mean* value of an ensemble of instantaneous undershoots, with corresponding standard deviation. Therefore, the variation in diameter of a trial due to the effect of the undershoot is (with 1-σ confidence)

$$\delta D \leq 2(\delta a_p \pm \sigma) \tag{5.3}$$

The corrected values are presented in the table 5.5

Overall there is a good correspondence between measured and calculated values when taking into account both deflection and undershoot. Only trials at f = 0.080 and a_p = 0.9 and 1.3, and at f = 0.160 mm/rev. have measured diameters which exceed what was expected. Analyzing the constant f = 0.080 mm row in table 5.3, a general increase in diameter with a_p can be seen, leading to cells were no micro-pins could be produced. At f = 0.160 mm, a similar behaviour is present, although at a_p = 0.5 and 1.3 no pins could be fabricated. The following hypotheses are put forward:

	a_p (mm)					
	0.5	0.9	1.3	1.7	2.1	2.5
0.005	343 ± 18	332 ± 8	326 ± 8	326 ± 6	322 ± 6	320 ± 4
0.010	342 ± 18	332 ± 8	326 ± 8	326 ± 6	322 ± 6	320 ± 4
0.020	343 ± 18	333 ± 8	326 ± 8	326 ± 6	322 ± 6	320 ± 4
0.040	346 ± 18	333 ± 8	327 ± 8	326 ± 6	x	x
0.080	352 ± 18	335 ± 8	327 ± 8	x	x	x
0.160	x	337 ± 8	x	x	x	x
f (mm/rev.)						

Table 5.5: Calculated diameters (μm) accounting for deflection and undershoot

Hypothesis 1: Coupling effects

Although the dynamometer, which is itself the tool holder, is extremely rigid (600N/μm), its connection to the X axis guide is mechanically poor (fig. 5.3, circled in red, two bolts providing hold down torque, but no pinned joint or register to locate it), which means that it has low stiffness. Further, a long *structural loop* (fig. 5.3, yellow dashed line) exists between the tool and the spindle, which contributes to the overall low stiffness of the machine.

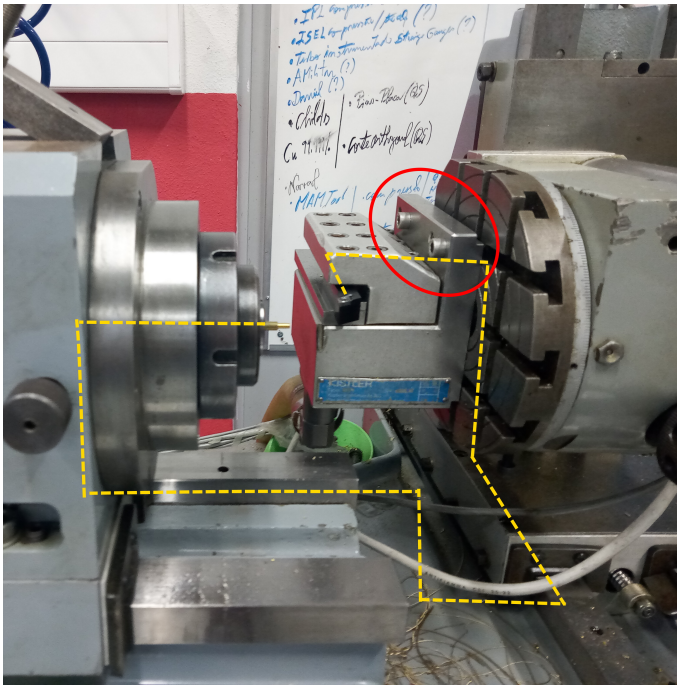

Figure 5.3: Mechanical connection between dynamometer and machine (dashed red), and structural loop between tool and workpiece (dashed yellow)

Simultaneously, when the tool is fed into the workpiece, its *interaction area* $A_{interaction}$ with the workpiece is dependent on two factors, the feed rate f and the depth of cut a_p. An increase in this interaction area clearly leads to a better coupling between the forces generated during turning and the dynamometer - X axis guide interface (and the whole machine). This improved coupling effectively transfers part of the forces experienced during machining to actuate this interface, which generates vibrations of the tool in all directions. The result of this is that the tool center position is not exactly determined and as a

consequence the diameters of the micro-pins are not as tightly controlled.

This vibration was noticed during the trials, especially at high a_p and/or high f, so much so that in certain trials the **whole machine** would vibrate quite noticeably. After a certain degree of vibration is imparted onto the tool, pins make contact outside the cutting edge of the tool and break off. This explains the increase of the diameter along the f = 0.080 mm row. The particular case f = 0.160 mm row is similar: the vibration is now worse, since f doubled compared to the previous case. At the lowest a_p, the pin has such a small cross section that it immediately snaps off, and at a_p = 1.3 mm, the combined effects of high a_p and high f force it to contact the tool outside the cutting edge, again snapping it off.

Hypothesis 2: Incorrect tool center height

The tool center height affects the true turned diameter. When the tool is perfectly positioned such that the cutting edge is along the center-line of the workpiece, the turned diameter is true to the commanded position. If the tool is either high or low, final turned diameter is bigger than the commanded one. Due to the small diameter of the micro-pin, it was not easy to adjust nor measure the vertical offset from the ideal position, although it was optically verified that the tool was below centre (see fig. 5.4). This error source was therefore not quantified.

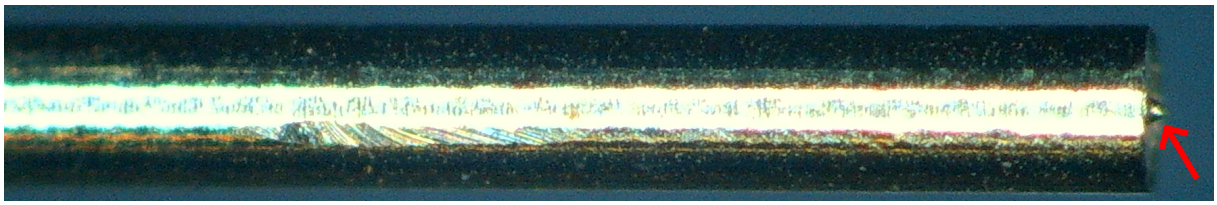

Figure 5.4: Tool center height misalignment: small ”nipple” at the end of the micro-pin

Hypothesis 3: Error in measurement

Particularly for the six trials at a_p = 2.1 and 2.5 mm (which were realized back to back), where the measured diameter is below 300 μm, the only possibility is that during the first operation to determine the zero of the tool, the incorrect diameter was taken with the micrometer.

5.2.2 Machining trials: Lower diameters

As a test, 8 extra trials were conducted to check if pins with diameter closer to the ideal 85 μm pivot diameter could be achieved. Two types of micro-pins were manufactured, with targeted diameters of 150 μm (in table 5.6) and 100 μm (in table 5.7), in the low a_p (0.5 - 0.9 mm) and low f (0.005 - 0.010 mm/rev.) (low vibration) region. Maximum acceptable diameters were calculated as before in section 5.2.1.

Measured values for both these series of trials are within the maximum acceptable diameter.

	a_p (mm)		F_y (N)	
	0.5	0.9	0.5	0.9
0.005	155 (214 $\pm$ 18)	177 (187 $\pm$ 8)	1.79	0.6
0.010	161 (223 $\pm$ 18)	165 (190 $\pm$ 8)	1.44	-0.03
f (mm)				

Table 5.6: Measured (and maximum acceptable) diameters (μm) for 150 μm trials

	a_p (mm)		F_y (N)	
	0.5	0.9	0.5	0.9
0.005	117 (150 $\pm$ 18)	128 (133 $\pm$ 8)	1.81	0.74
0.010	109 (150 $\pm$ 18)	123 (133 $\pm$ 8)	1.58	-0.04
f (mm)				

Table 5.7: Measured (and maximum acceptable) diameters (μm) for 100 μm trials

Closing thoughts on diameter trials

Generated micro-pins (in fig. 5.5 a comparison between different diameter micro-pins) are generally within the maximum acceptable diameter, calculated taking into account both deflection and undershoot. One of the performance criteria was that the diameter tolerance should be h4. This is because a tolerance of h4 (+0/-3 μm for the fabricated micro-pins, independent of diameter), given a positive tolerance of H6 (+5/-0 μm) for the jewel, assures a 7 $^\circ$ maximum lean of the balance staff in its jewel, the ideal case according to [3]. Clearly, the results are far from what is necessary for the correct functioning of the pair pivot/jewel bearing, since the produced pins had tolerance limits of

- 300 μm trials: +115/-25 μm
- 150 μm trials: +27/+5 μm
- 100 μm trials: +28/+9 μm

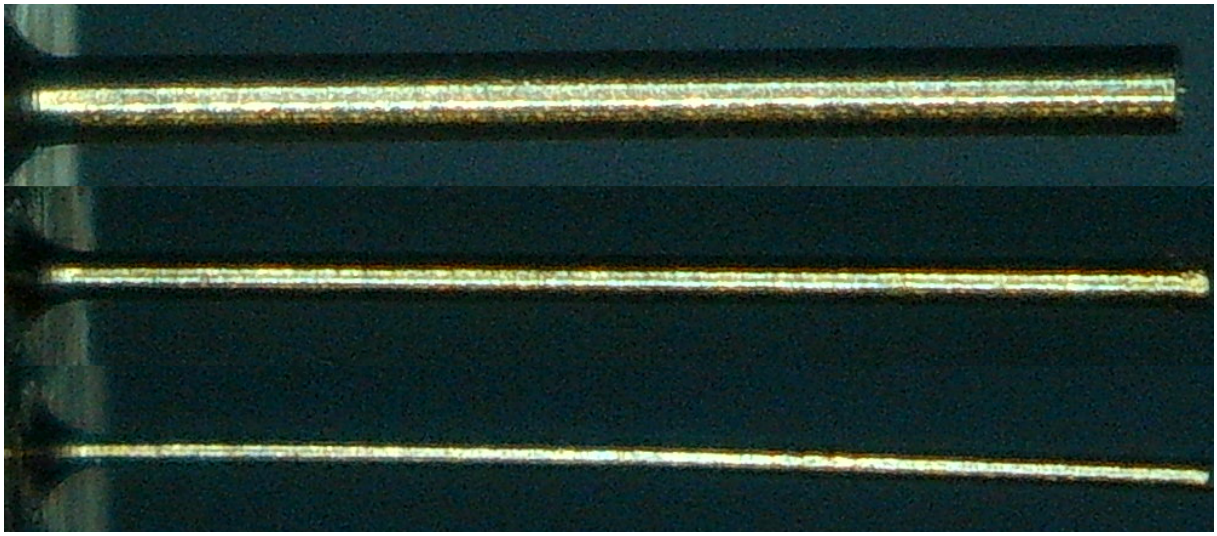

Figure 5.5: Fabricated micro-pins diameter: 300, 150 and 100 μm (from top to bottom)

No direct comparison of the results obtained can be made with the available literature since no detailed methodology on how the micro-turning operation is realized and how the cutting tool center point is zeroed for this operation is presented. However, in this work, the effects of undershoot of the X axis and the uncertainty in the tool center position are the main factors determining the final micro-pin diameter, both severely limiting the application of the present machine in micro precision mechanics. In particular, the main cause for the undershoot is the current resolution of the encoder of the X axis. While it is 4x the resolution in the Z axis, it is still quite insufficient. From the previous section results, it is expected that a 100-fold increase in resolution can bring a 100-fold reduction of the undershoot, which would result in an accuracy of around 0.2 μm (with a depth of cut of 500 μm). This, combined with an operation at low a_p and f (low vibration), could possibly make the micro-pins compliant with the h4 requirement.

Straightness

Although not specified as a performance criteria since balance staff pivots are much shorter than 4 mm, straightness of the fabricated micro-pins depended on their diameter and the level of vibration. No attempt was made to try and quantify this error, since no suitable method was found to do so. Straighter pins were obtained at low a_p and low f. Lower diameter pins were less straight than larger diameter pins at the same a_p and f.

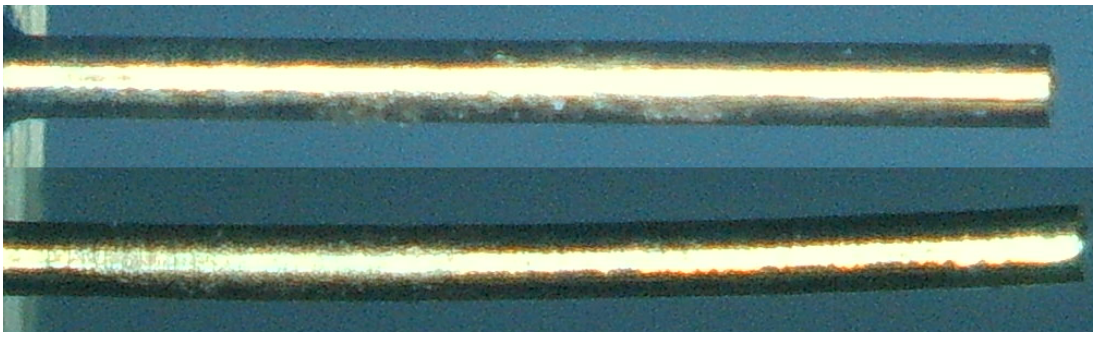

Figure 5.6: Straightness of micro-pins. Constant f, a_p = 0.9 (top) and = 2.1 (bottom)

5.2.3 Machining trials: Surface roughness R_a

The measured R_a values are presented in table 5.8. where it can be seen that, generally, R_a increases with increasing a_p and/or f.

While the dependence on f was expected (and seen in figs. 5.7a and 5.7b), on the contrary, the dependence on a_p was not. R_a, which is given by

$$Ra_{theo.} = \frac{f^2}{32 r_b} \tag{5.4}$$

derived from purely geometrical arguments (see. fig. 2.13a) suggests no such dependence. Further, the obtained values are significantly different from the predicted ones by eq. 5.4.

	a_p (mm)						
	theo.	0.5	0.9	1.3	1.7	2.1	2.5
0.005	0.004	0.280	0.252	0.310	0.340	0.944	2.099
0.010	0.016	0.268	0.240	0.374	0.591	1.901	3.056
0.020	0.063	0.485	0.485	0.761	1.373	4.051	4.266
0.040	0.250	0.808	1.053	1.600	3.364	x	x
0.080	1.000	2.069	2.077	2.121	x	x	x
0.160	4.000	x	3.797	x	x	x	x
f (mm/rev.)							

Table 5.8: Surface roughness R_a (μm) of the various micro-pins. Cells marked at grey meet the performance criteria of R_a (< 0.4 μm)

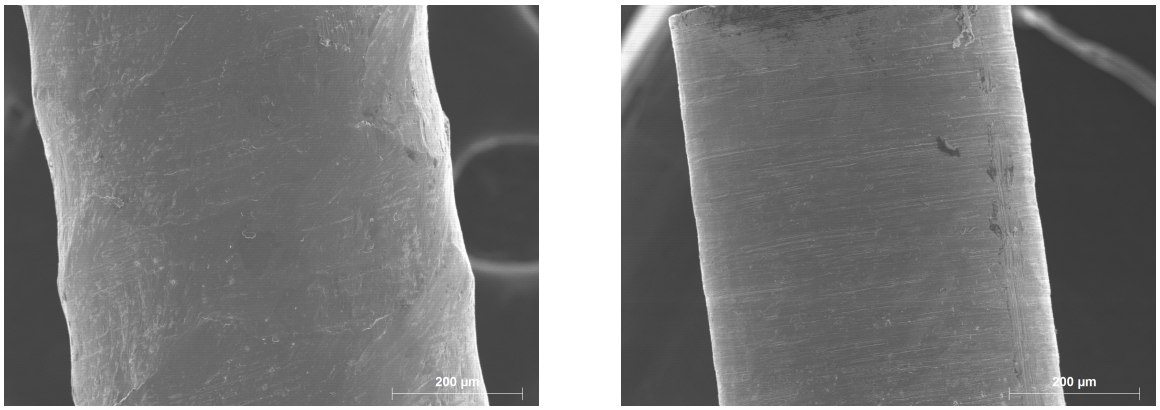

(a) (b)

Figure 5.7: SEM micrograph of micro-pin surface at constant a_p = 1.7 mm and (a) high *f* (0.040 mm/rev.) (b) low *f* (0.005 mm/rev.)

From the conducted trials results, two hypotheses can be put forward to try and explain the disagreement between the theoretical and measured R_a:

Hypothesis 1: Coupling effects

This is the same hypothesis as the one in in the previous section. Since vibration affects the true tool center position, the peaks and troughs of the surface are no longer regular as assumed by eq. 5.4. According to this hypothesis, vibration modifies the true a_p and *f* in a complex way (refer to fig. 5.8).

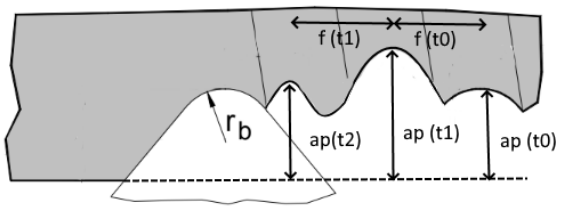

Figure 5.8: General behaviour of cutting tool center vibration and effect on R_a

As was explained in the previous section, it is clear that if the area of interaction increases, the coupling between process forces and vibration of the tool holder is increased. This can potentially generate a larger amplitude and/or frequency of peaks and troughs on the surface of the micro-pin. This is equivalent

to saying that

$$R_a = f(A_{interaction}) \tag{5.5}$$

To check which factor is more important for $A_{interaction}$, lets first take a look at the dependence on a_p (constant f). Fig. 5.9 presents the area of contact during fabrication of the micro-pins at constant f.

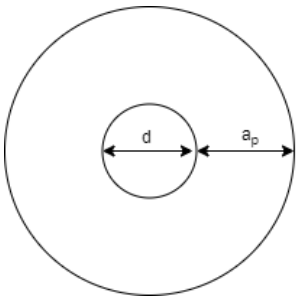

Figure 5.9: Area of contact during micro-pin manufacturing (frontal view) at constant f

Here, d is the diameter of the micro-pin, which is always constant, $d = 300\,\mu m$. The area of the annulus region is in turn given by

$$A_{annulus} = \pi\left(\left(a_p + \frac{d}{2}\right)^2 - \left(\frac{d}{2}\right)^2\right) = a_p^2 + a_p d \tag{5.6}$$

In the case of trials at constant a_p but variable f, then the area seen by the tool is different. From the fig. 5.10, it follows that (during 1 revolution)

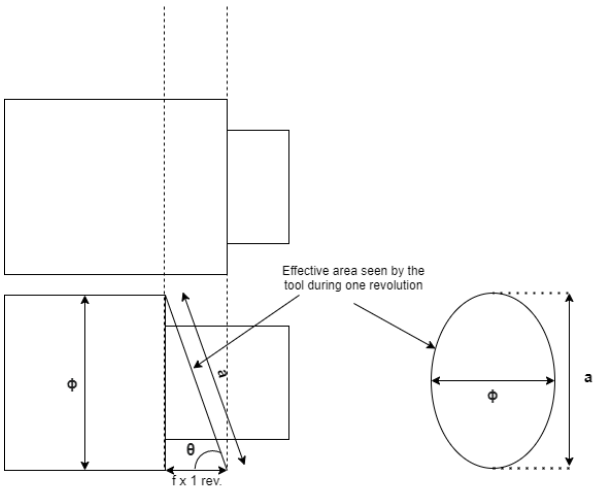

Figure 5.10: Effective area of contact encountered during 1 revolution during micro-pin manufacturing (top view) at constant a_p

$$\tan\theta = \frac{\phi}{f} \Leftrightarrow \theta = \arctan\left(\frac{\phi}{f}\right) \tag{5.7}$$

The area of contact in this case is no longer a circle but an ellipse, with a minor axis corresponding to the diameter ϕ. The major axis is given simply by

$$\sin\theta = \frac{\phi}{a} \Leftrightarrow a = \frac{\phi}{\sin\theta} \tag{5.8}$$

Combining eqs. 5.8 and 5.7 we arrive at the following expression

$$a = \frac{\phi}{\sin\theta} \propto \frac{1}{\sin\theta} = \frac{1}{\sin\left(\arctan\frac{\phi}{f}\right)} \propto \frac{1}{\sin\left(\arctan\frac{1}{f}\right)} \tag{5.9}$$

since ϕ is constant at constant a_p.

This last expression can be simplified to

$$\sin\left(\arctan\frac{1}{f}\right) = \frac{\left(\frac{1}{f}\right)}{\sqrt{1+\left(\frac{1}{f^2}\right)}} \tag{5.10}$$

Therefore,

$$a \propto \frac{\sqrt{1+\left(\frac{1}{f^2}\right)}}{\frac{1}{f}} = f\sqrt{1+\left(\frac{1}{f^2}\right)} = \sqrt{1+f^2} \tag{5.11}$$

Using the formula for the area of the ellipse, and combining the previous result, we obtain

$$A_{ellipse} = \pi a\phi = \pi\phi\left(\sqrt{1+f^2}\right) \propto \sqrt{1+f^2} \approx \begin{cases} 1 & \text{if } f \text{ is low} \\ f & \text{if } f \text{ is large} \end{cases} \tag{5.12}$$

Therefore, there is practically no effect of f on the interaction area (and therefore R_a) in the low f regime. Summarizing both results, the interaction area is proportional to

$$A_{interaction} \propto \begin{cases} a_p^2 + a_p d & \text{if trials at constant } f \\ f & \text{if trials at constant } a_p \text{ and large } f \end{cases} \tag{5.13}$$

From these results it is expected then that vibrations, which are some function of the interaction area $A_{interaction}$ under this assumption, are more strongly dependent on a_p than f. Under this hypothesis, we can modify eq.5.6 to include this term:

$$Ra_{exp} = Ra_{vib.}(a_p, f) \tag{5.14}$$

The theoretical term $Ra_{theo.}$ has been dropped since the assumption that a_p and f are constant during the trial is no longer true.

Hypothesis 2: Effects of finite stiffness

The micro-pin, unlike what is assumed when deducing the theoretical R_a value, is not infinitely stiff. Instead, the micro-pin deflection (recall fig. 5.2) is given by

$$\Delta y = \frac{128 F_y L^3}{6 E \pi D^4} \tag{5.15}$$

where *L* is the length of the overhanging pin (a function of the axial position of the tool), and *D* is its initial diameter, a function of a_p:

$$D = 0.3 + 2a_p \text{ (mm)} \tag{5.16}$$

The dependence on *L* is constant, since all pins have roughly the same length. While at the beginning of the trial the pin is at its most overhang, the actual a_p is not the expected, since the tool might not even be engaging the pin properly, instead sliding along the surface, potentially causing severe rubbing and adhesive wear and increasing R_a. By the end of the trial, the pin is at its lowest overhang, and this effect is less noticeable. In figs. 5.11a and 5.11b, an example of this effect is visible in the surface roughness of a micro-pin.

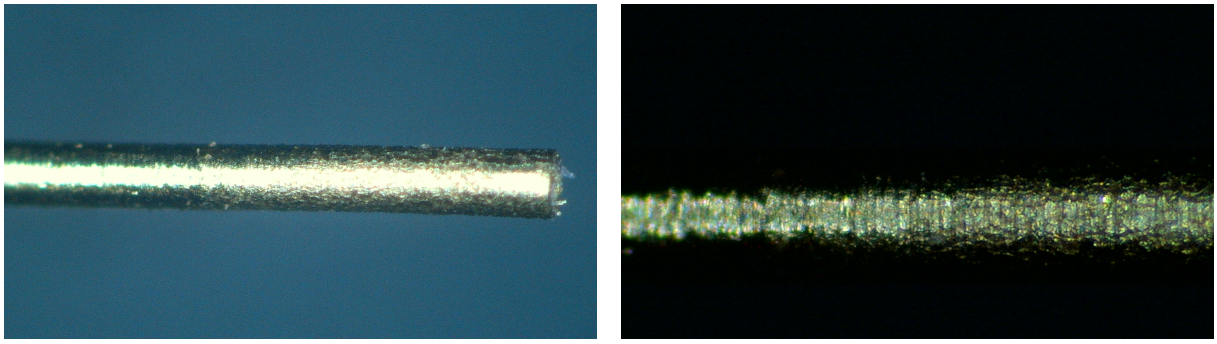

(a) (b)

Figure 5.11: (a) Fabricated micro-pin and surface roughness transition zone (b) Closeup of transition zone

Also, trials conducted at smaller initial pin initial diameter D will suffer higher deflections that those with larger diameters. This is equivalent to saying that smaller a_p will tend to produce larger deflections and therefore less true a_p, with the tool rubbing along the micro-pin surface.
This contribution is dependant on

$$\Delta y \propto \frac{1}{D^4} \propto \frac{1}{a_p^4} \tag{5.17}$$

Under this hypothesis.

$$Ra_{defl.} = f(\Delta y) \tag{5.18}$$

Therefore the full expression for R_a under these two hypothesis is

$$Ra_{exp} = Ra_{vib.}(a_p, f) + Ra_{defl.}(a_p) \tag{5.19}$$

with each term having the following general behaviour:

$$Ra_{vib.}(a_p, f) \begin{cases} \uparrow\uparrow \text{ as } a_p \uparrow \\ \uparrow \text{ as } f \uparrow \end{cases} \tag{5.20}$$

$$Ra_{deflection} \downarrow \text{ as } a_p \uparrow \tag{5.21}$$

Note on preceding derivations

Although the modification to the theoretical expression eq. 5.6 is a more complete model for the R_a figure, both hypothesis still stem from geometrical arguments. The exact dependence of R_a on a_p and f is still unknown and likely takes a complex form. Therefore, the major conclusion to take from this section is that **a_p should be a stronger estimator of R_a than f**.

General overview of the results in light of the developed model

A competition between these two potential mechanisms occurs: in the region where a_p is small (0.5 - 0.9 mm), the deflection term $Ra_{deflection}$ appears to dominate at low values of f (0.005 - 0.010 mm/rev.). Crossing from a_p = 0.5 mm to 0.9 mm, a reduction of R_a occurs due to an increase of the pin initial diameter, which lowers deflection and therefore lowers the contribution of $Ra_{deflection}$ towards the total Ra value. Contrary to the expected, from f = 0.005 mm/rev. to 0.010 mm/rev. R_a decreases. The difference between values is small enough that their difference can be merely statistical in nature, due to the small population of samples;

A transition at f (0.020 mm) to a zone where the vibration term $Ra_{vib.}$ takes over can be seen f (0.040 - 0.160 mm), since if the main contributor to R_a here was $Ra_{deflection}$, the total R_a value should be constant along the constant a_p (vertical) lines.

Independently of f, beyond a_p = 1.3 mm, the effect of $Ra_{vib.}$ overwhelms $Ra_{deflection}$.

Closing thoughts on obtained R_a

The first conclusion regarding these results is that although the ideal value of R_a < 0.1 μm was not reached, the fabricated micro-pins length, due to limitation on the equipment used to measure this value, had an aspect ratio $\frac{L}{D} = \frac{4}{0.3} \approx 13$. However, typical balance staff pivots are very short. As an example of this fact, in fig.1.1b, $\frac{L}{D} \approx 2$. Therefore, better values of R_a, according to the developed hypothesis, should be possible to achieve on micro-pins with $\frac{L}{D}$ comparable to balance staff pivots.

Further, looking into the reviewed literature, a wide range of operating regimes can be applied with satisfactory results (R_a < 0.4 μm). This work appears to be at the extreme end of a_p and f used. While the produced pins can be considered ”micro”, the optimal operating conditions in this work are orders of magnitude larger than the reviewed micro-turning works (with the exception of [9]). Two effects are important to analyze here. First is the hypothesized relationship between R_a and $A_{interaction}$. While this work and [9] have relative large $A_{interaction}$ (due to high a_p and f) and correspondingly high R_a, works

Source	R_a (μm)	a_p (μm)	*f* (μm/rev.)
[8]	$\ll 1$	5	0.012
[14]	0.06	20	0.2
[24]	0.055	75	1
[15] [16]	< 0.1	5	3
[9]	0.33	200	8
This work	0.240	900	10

Table 5.9: Comparison between developed machine and those of literature: R_a @ optimal a_p and *f*

at substantially lower values of these parameters have lower R_a values, which is further evidence to sustain this hypothesis.

Secondly, according to [17], the cutting regime is dependent on the ratio $\frac{f}{r_{edge}}$, and while the reviewed works do not present values of r_{edge}, in this work its value was estimated from images taken with a SEM (figs. 5.12a and 5.12b) at a value of approximately 5 μm (the manufacturer of the tool used also does not present this value).

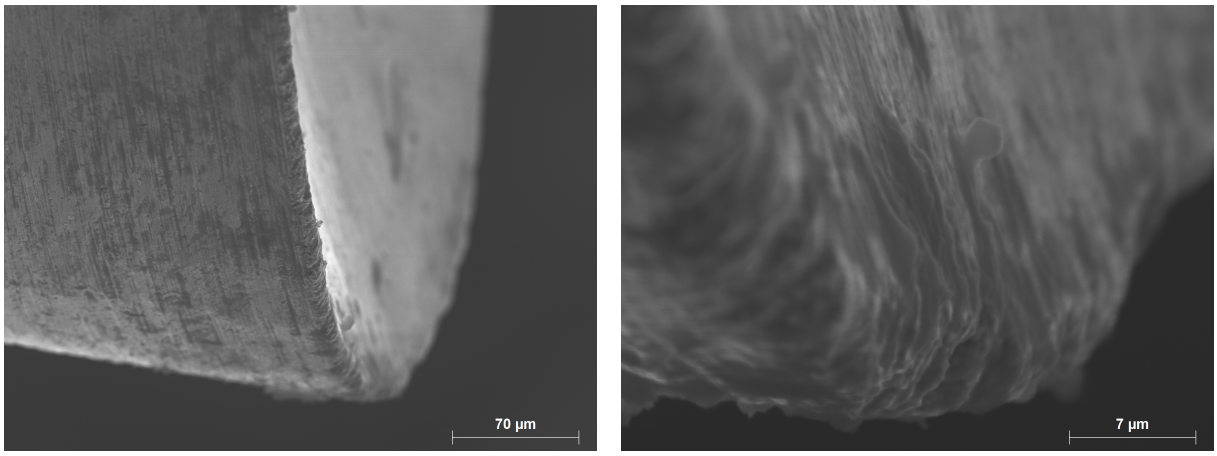

(a) (b)

Figure 5.12: (a) SEM micrograph of the (virgin) turning tool, showing the rounded edge radius (b) a closeup of the tool edge radius

The tool edge radius is evident, with the tool appearing quite blunt at this scale. Based on the best results obtained (*f* = 5 - 10 μm/rev.), $\frac{f}{r_{edge}} \sim 1 - 2$. Recalling figures 2.15c and 2.15d, this corresponds to the zone where the cutting mechanism is the concentrated shear deformation of the chip. In this zone, the obtained R_a for brass (R_a = 0.218 μm) is similar to the one obtained in this work. However, the best R_a is achieved only when the cutting mechanism transitions from shear deformation to burnishing ($\frac{f}{r_{edge}}$ = 0.01 - 0.1).

Assuming the reviewed works had $r_{edge} \geq 5\ \mu m$, then works [15], [16], [24] and [14] are likely inside the burnishing range given the low values of *f* and R_a, much smaller than those obtained in this work (and [9]). This assumption should be valid since: **(i)** tools utilized in these works are either cemented carbide ([15] and [16]) or PCD ([24] and [14]), with the only exception to this being [8], in which a monocrystalline diamond tool is used; **(ii)** although in these works no grain size is reported for the tool, according to [27], the finest grains for PCD and carbide tools are 0.5 and 0.2 μm, respectively. Since the tool cutting edge must be robust enough to support the cutting forces, it must be made of a large collection of grains, and

therefore the cutting edge is only well defined at a scale larger than the grain size. This assumption is not valid for [8], since in principle an atomically sharp and well defined edge can be made on a single crystal. However no definitive value for R_a is presented in this work.

Therefore, the goal of reaching R_a < 0.1 μm should be possible if this work was extended to lower *f* and a_p values than those tested, to a zone where the effect of vibration and deflection is small and where $\frac{f}{r_{edge}}$ is within the burnishing zone. This is problematic since **(i)** it is currently impossible to achieve lower *f* given that the developed machine has insufficient resolution and is based on high static/dynamic friction linear guideways; **(ii)** since $D = f(a_p)$, lowering a_p decreases D, which in turn might increase deflection of the micro-pins. A different cutting strategy or a different tool (with lower r_b) need to be used to prevent this.

5.3 Machining trials: Optimal operating zone

Given the performance criteria established in the previous chapter, it is possible to select an optimal operating zone, one where both diameter and R_a fulfill the performance criteria. This zone corresponds to the low-mid a_p (ranging from 0.5 to 1.7 mm) and low *f* (ranging from 0.005 to 0.010 mm/rev.), marked in table 5.8 with grey cells. This is also the region of the map where vibration was verified during trials to be less felt. This is useful for the following analysis since it limits the extreme effects vibration has on R_a, enabling a simpler and more accurate model of the dependence of this factor with a_p and *f*.

Although R_a figures are below 0.4 μm (excepting the value at a_p = 1.7 mm and *f* = 0.010 mm/rev., which was included in the following analyzes for completeness), the best value still fall short of the 0.1 μm figure. A further investigation was carried within this optimal operating zone to check if the introduction of ***lubricant*** during micro-turning would bring a reduction of R_a to $<$ 0.1 μm. The cutting oil available was a high performance machining oil from Mobil, the Mobilmet 27. Trials within the optimal operating zone were repeated now with the application of small amounts of this cutting fluid manually.

5.3.1 Surface roughness R_a inside optimal operating zone with lubricant

Measured R_a for each micro-pin is presented in table 5.10:

f (mm/rev.)	*a_p (mm)*			
	0.5	0.9	1.3	1.7
0.005	0.378	0.358	0.510	0.594
0.010	0.420	0.300	0.646	0.763

Table 5.10: Surface roughness R_a (μm) of the various micro-pins machined with lubricant. Cells marked at grey meet the performance criteria for R_a (< 0.4 μm)

The introduction of lubricant had the *opposite* effect, increasing R_a. The analysis of these results will be done in the following section, by comparing them with the previous results obtained during dry machining.

5.4 Machining trials: Optimal operating zone model

To evaluate the influence of the main factors and possible interactions between a_p, f and the presence of lubricant on R_a, a full factorial, 3 factor model was generated in a DOE software, with the following parameters:

- Factor A: a_p - 4 levels (0.5, 0.9, 1.3 and 1.7 mm)
- Factor B: f - 2 levels (0.005 and 0.010 mm/rev.)
- Factor C: Lubricant - 2 levels (yes and no)

In order to be able to study the derived model with confidence, it is necessary that the response variable (R_a) follows a normal distribution. This could pose a problem, since in the low R_a region, the measured value will asymptotically approach the ***noise floor*** of the instrument and the environment, which would mean that R_a fails to follow a Normal distribution. Since no noise floor measurement was made with the instrument initially, a distribution identification analysis was carried out to identify which type of distribution best describes the available data.

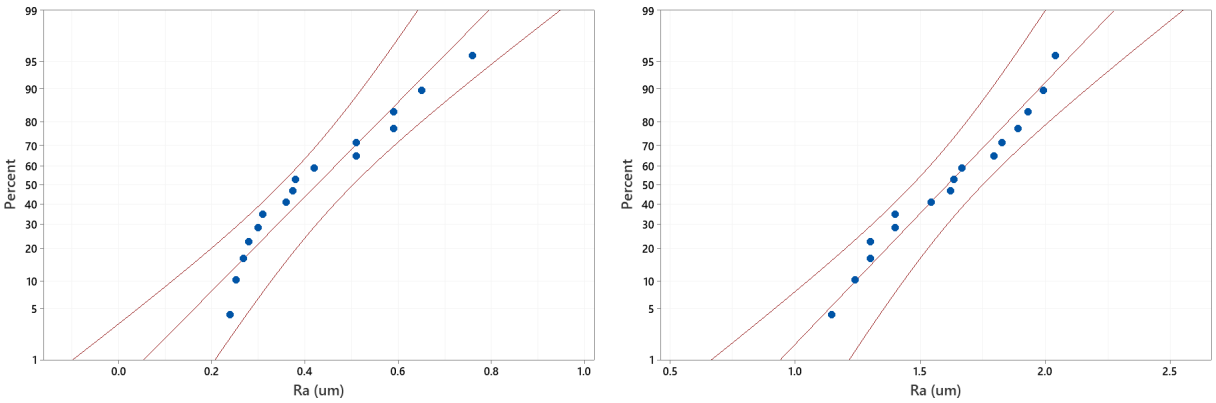

(a) (b)

Figure 5.13: (a) Probability plot for R_a, Normal distribution (b) Same, after Box-Cox transformation with λ = -0.5

As seen from figure 5.13a, while the p-value (**0.168**) for the fit of the response variable R_a to the Normal distribution suggest we should not reject the null hypothesis (that the response variable follows a Normal distribution) at the selected confidence level (**95%**), the results show a slight downward trend of R_a as values try to approach zero, as expected. After applying the distribution analysis test, a best fit was found when using a Box-Cox transformation with λ = -0.5,

$$Ra_{Box-Cox} = \frac{Ra^{\lambda} - 1}{\lambda}, \lambda = -0.5 \tag{5.22}$$

The modified response variable $Ra_{Box\text{-}Cox}$ (shown in fig. 5.13b) fits a Normal distribution with a better p-value (**0.542**). Using this new response variable, a general factorial regression was applied to it, with the following characteristics:

- Terms: A, B, C, AB, AC, BC (no extra degrees of freedom to test higher order dependencies, given the limited trial population);

- Stepwise: Backward elimination (α = 0.1);

5.4.1 Model: summary

- S = 0.03214;
- R^2 = 99.66%;
- $R^2_{adj.}$ = 98.74%;
- $R^2_{pred.}$ = 94.64%

Although R^2 and $R^2_{pred.}$ point out that the variation observed is well explained by the model and that the model has good predictive ability, since only one model was fitted (due to lack of repeated observations), no extra conclusions are made regarding these factors. Given the small number of samples, the following analysis will remain mainly qualitative, to try and understand the effect each factor has on R_a.

5.4.2 Model: Normal Probability Plot

The Normal probability plot, presented in fig.5.14a shows that the residuals are normally distributed, following closely along the straight line, with no evidence of outliers.

5.4.3 Model: Residuals vs. Fits

No patterns are observed in the residuals vs. fits graph (fig.5.14b), with points appearing to fall randomly on either side of the line.

5.4.4 Model: Residuals vs. Order

In the residuals vs. Order graph (fig. 5.14c), no pattern can be identified, which is sign that the residuals are uncorrelated.

5.4.5 Model: Residuals Histogram

In the residuals histogram (fig. 5.14d), the lack of sample size is noticeable. Given this fact, no conclusion regarding normality is taken from this histogram (the normality condition is better seen on fig.5.14a).

5.4.6 Model: Pareto chart and Factorial Plots

Referring to fig. 5.15a, at the selected confidence level, there are four main predictors.

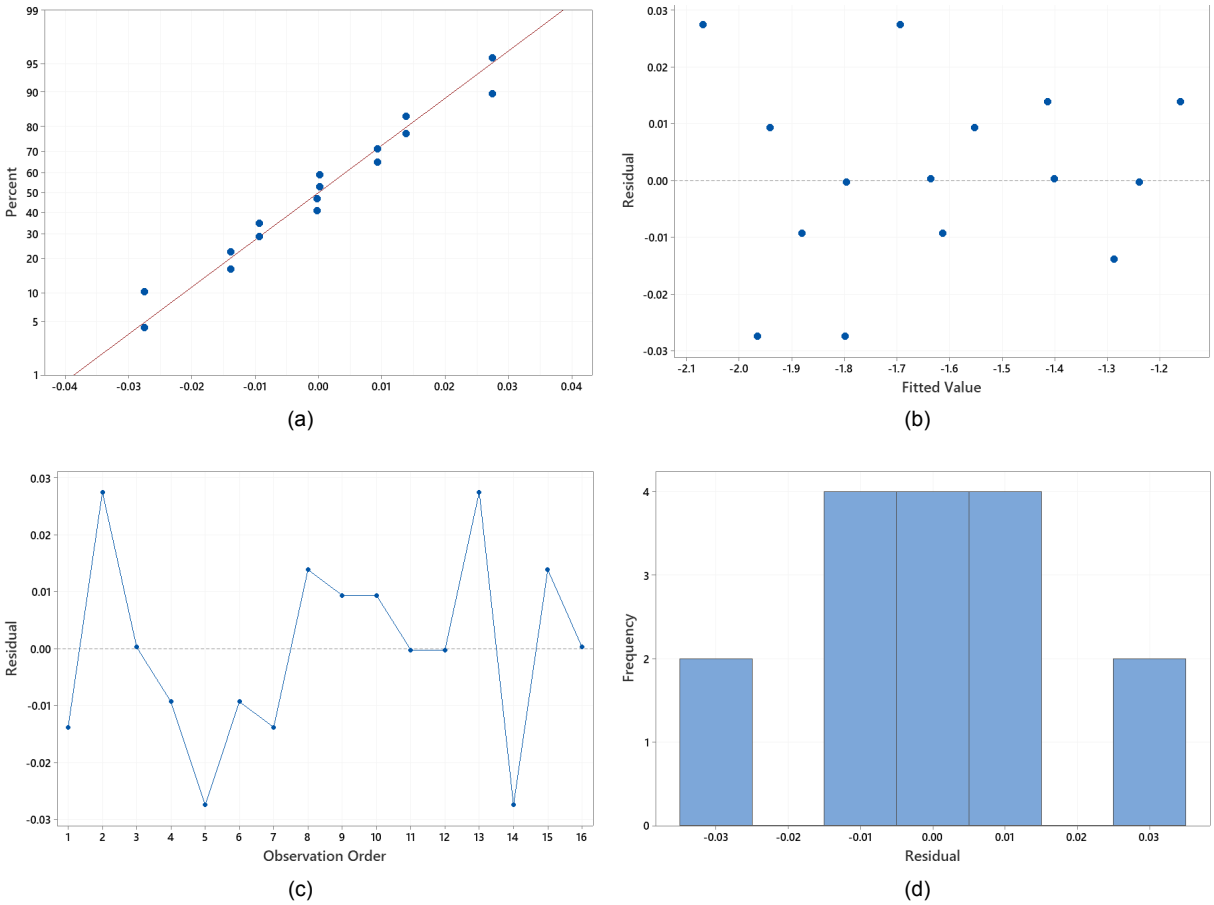

Figure 5.14: (a) Normal Probability Plot for R_a (b) Residuals vs. Fits for R_a (c) Residuals vs. Order for R_a (d) Residuals histogram for R_a

Strongest predictor: a_p

The results show that the strongest predictor of R_a is a_p (A in fig. 5.15a is the largest, as is the slope of a_p in 5.15b). Recalling the previous analysis, the hypothesis put forward,

$$Ra_{exp} = Ra_{vib.}(a_p, f) + Ra_{defl.}(a_p) \tag{5.23}$$

also generated a dependence of R_a on a_p, which was assumed to be the strongest based purely on the dependence of $A_{interaction}$ and Δy with a_p and f. In this regard, both model and hypothesis seem to coincide.

Second strongest predictor: Lubricant

The second most significant predictor of R_a is the ***lubricant*** (C in fig. 5.15a, and with the second steepest slope in 5.15b). The idea behind introducing a lubricant during turning of the micro-pins was to reduce friction in the interface between the cutting tool and the forming metal chip and the workpiece (more on this in section 5.5.1), which could result in an improved chip flow from the cutting area and in less dry rubbing of the tool against the workpiece, lowering R_a.

However, what was noticed during every trial with lubricant was that due to the *viscosity* of the cutting

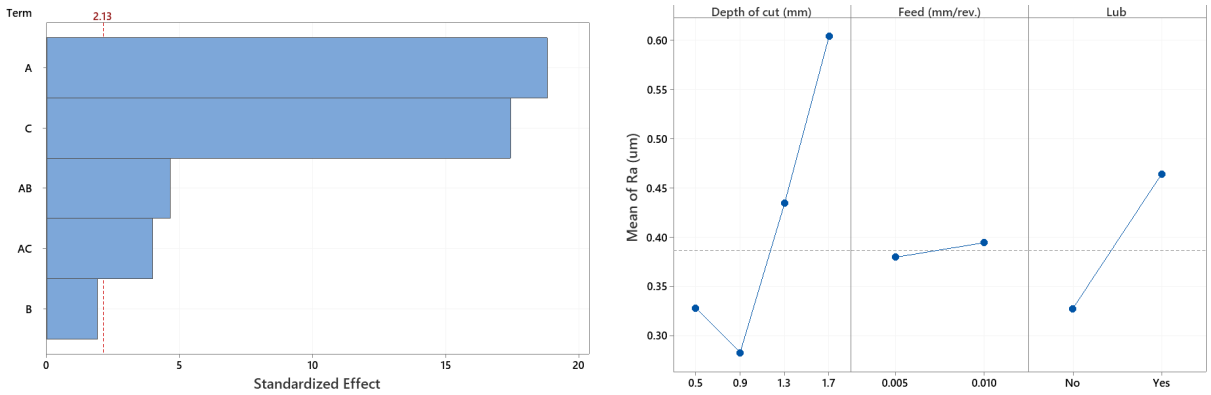

(a) (b)

Figure 5.15: (a) Pareto Chart of standardized effects (b) Main Effects Plot for R_a

fluid, chips could not be evacuated from the cutting zone at all, and accumulated along the cutting front and on the backside of the cutting tool, the region of the newly formed micro-pin. This, combined with the long *residence time* of the tool in the cutting area due to low *f*, increases the likelihood of chip contact with the micro-pin, in turn causing rubbing and increasing R_a.

Predictor interactions: a_p and *f*

Besides these two main predictors, there are also two less strong interactions which affect R_a. First, the effect of a_p is compounded by the increase in *f*. Calling attention to fig. 5.16a, which displays the interaction between a_p and *f*, gives further insight to the proposed hypothesis.

In the low a_p zone (0.5 - 0.9 mm), the effect of $Ra_{defl.}$ dominates over $Ra_{vib.}$. It decreases in strength as a_p increases (as expected), and the interaction between a_p and *f* is almost nonexistent, consistent with the hypothesis that $Ra_{defl.}$ is not a function of *f*, as the lines of *f* are very close and parallel. The reason that at higher *f* the R_a is slightly lower (not predicted by the hypothesis) might indicate that it is a statistical effect. If sample size increases, it is likely that the expected increase in R_a with *f* appears.

On the contrary, after the transition from a_p = 0.9 mm to 1.3 mm and larger, where $Ra_{vib.}$ starts to dominate, the lines are also parallel, but are much farther apart. This means that at high enough a_p, this parameter has an influence on how strong the effect of *f* is (a_p uplifts *f*). Most likely, if trials were executed with an higher range of *f*, this effect would further increase in importance.

This indicates that the particular relationship between $Ra_{vib.}$ and *f* is dependent both on a_p and *f* (through $a_p f$, according to this model).

Predictor interactions: a_p and presence of lubricant

The effect of a_p is also compounded by the application of lubricant (seen in fig. 5.16b), although the effect is subtle, making it hard to extract any useful explanation to what is in fact happening.. In this figure, the distance between the lines corresponding to trials without and with lubricant varies with a_p (highest at a_p = 1.3 mm, lowest at 0.9 mm and similar at 0.5 and 1.7 mm). If the effect was that the accumulation of the metal chips caused more contact between them and the surface of the micro-pin due to an increase in

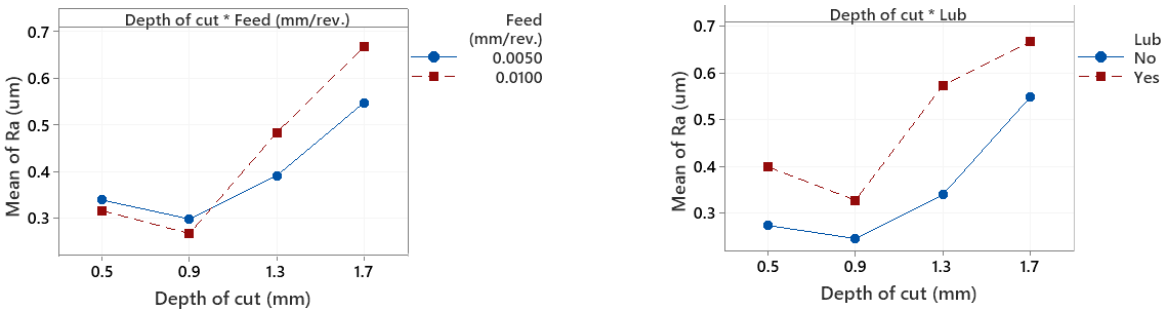

(a) (b)

Figure 5.16: Interaction Plot for R_a (a) a_p vs. f (b) a_p vs. lubricant

vibration, then the lines should diverge for increasing a_p. If this was not the case, and instead the effect was that the metal chips merely accumulated in the newly formed micro-pin zone, then no increase with a_p should be seen, and both lines should be parallel. More trials should be conducted to try and find the real mechanism behind this interaction.

The case of *f*

From the data available, it is not possible to conclude that f is an effective predictor of R_a by itself (B in fig.5.15a, shallow slope in fig.5.15b). Recall that under the developed hypothesis, R_a is assumed to be a function of the interaction area which, according to eq. 5.12, is roughly independent of f, if this factor is low enough. This is a strong indication that the hypothesis put forward might be correct.

Closing thoughts on the derived optimal operating zone model

The assumption that the dependence of R_a is not only that of theory, but to a more complex function of a_p and f (and the presence of ***lubricant***) seems to be correct.
The proposed relationship between

$$R_a \Leftrightarrow A_{interaction} \tag{5.24}$$

is validated by the strong dependence of this value on a_p and the lack of evidence of any influence on f by itself.
Given the limited degrees of freedom, no other models were fitted against the modified response variable. This lack of degrees of freedom also prevents the introduction of higher order terms in the analysis. If a mathematical formulation for the $Ra_{exp.}$ expression exists, then the introduction of these terms would be beneficial in trying to quantify it.

5.5 Machining trials: Forces in the optimal operating zone

The previous discussion focused on the diameter and the surface roughness obtained, which were the principal interest of this thesis. However, a brief overview of the forces obtained during the turning

operations in the optimal zone will be made.

5.5.1 Cutting forces results

	a_p (mm)			
	0.5	0.9	1.3	1.7
0.005	5.45	9.60	12.73	14.88
0.010	8.34	13.93	18.84	22.95
f (mm/rev.)				

Table 5.11: Cutting force results (N) - dry

	a_p (mm)			
	0.5	0.9	1.3	1.7
0.005	4.56	7.59	9.91	12.62
0.010	6.41	11.25	15.05	19.59
f (mm/rev.)				

Table 5.12: Cutting force results (N) - lubricated

From the results obtained (tables 5.11 and 5.12), the major observations to be made are that the introduction of lubricant during the trial did decrease the cutting forces experienced, and that the cutting force increases both with a_p and f.

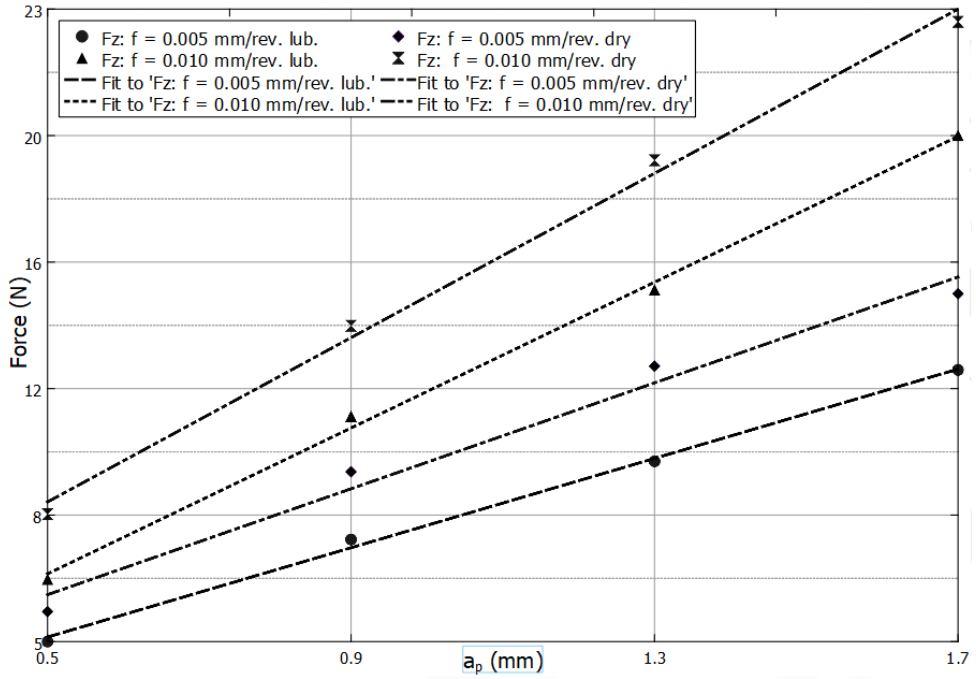

Figure 5.17: Linear regression of the results

Since the cutting force F_c can be expressed through

$$F_c = k_s a_p f \tag{5.25}$$

where k_s is the *specific cutting force*, the results were fitted with a linear expression,

$$y = c_0 + c_1 x \tag{5.26}$$

where $y = F_c$, c_0 an offset and $c_1 = k_s f$. The fitting results are presented in tables 5.13 and 5.14 (where the value under parenthesis corresponds to the relative reduction of k_s compared to the

corresponding value in table 5.13).

f (mm/rev.)	c_0 (N)	c_1 (N/mm)	k_s (N/mm^2)
0.005	2.025	7.855	1571
0.010	2.612	12.185	1219

Table 5.13: Fit coefficients - Dry

f mm/rev.)	c_0 (N)	c_1 (N/mm)	k_s (N/mm^2)
0.005	1.383	6.625	1325 (- 15.6%)
0.010	1.164	10.815	1082 (- 11.2%)

Table 5.14: Fit coefficients - Lubricated

Looking into the results, the following can be stated: that an increase in *f* decreases k_s, while the presence of lubricant also decreases this parameter. k_s is an experimental parameter, and therefore the formula for the cutting force, presented before, is exact. While no explicit dependence of k_s on material and process parameters was introduced, this factor is a reflection of the energy balance in the turning process, which, according to [31] is (in a simplified way)

$$dU_{ext} = dU_c + dU_f + dU_d \ (+ \ dU_{fw}) \tag{5.27}$$

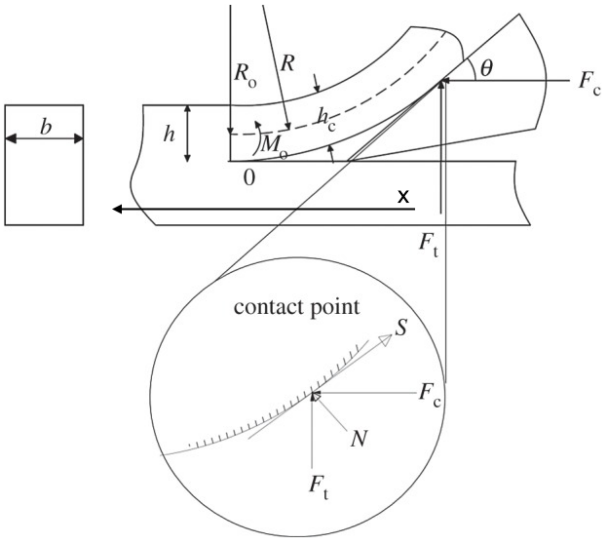

Figure 5.18: Interaction between tool and forming metal chip, adapted from [31]

where, during a movement of the tool dx in fig. 5.18, these terms can be expressed as: $dU_{ext} = F_c dx$ is the supplied energy, $dU_c = G_c b dx$ is the fracture energy (and G_c the *fracture toughness*) necessary to initiate fracture and create new surfaces, $dU_f = S dx$ is the friction dissipated energy (and S the *shear force*) and dU_d is the energy used in plastically deforming the material. The term under parenthesis, dU_{fw}, is not present in [31] but should also be considered, the friction between the tool and the workpiece.

The observed reduction of k_s with the introduction of lubricant can be seen as a reduction of the friction energy dU_f and dU_{fw}, dissipated at the tool-chip and tool-workpiece interfaces respectively, while both dU_d and dU_c remain constant, since the amount of material being removed is the same. The reason why k_s decreases with the increase in *f* is three-fold, due the relative importance of the terms in eq. 5.27. First, at the highest *f*, the ratio between new surface area created and deformed volume of material is lower than at low *f*, since higher *f* equates to higher initial chip thickness *h* (fig. 5.18). In other words, at a lower *f*, more surface area has to be created per unit of deformed material than at a higher *f*,

leading to higher k_s through an increase of dU_c. Second, this increased ratio between surface area and deformed volume at lower *f* means that chips are thinner, and therefore, to remove the same volume of material more chips have to flow across the cutting edge of the tool, increasing dU_f. Finally, at lower *f*, the residence time of the cutting tool in the cutting zone is greater, which increases the friction work dU_{fw}. All these mechanisms are responsible for the different relative reduction of k_s (15.6% vs. 11.2%). Clearly, both friction at the tool-chip and tool-workpiece interfaces and fracture of the material are important mechanisms in metal cutting, since k_s is significantly higher than the yield strength of brass ($\sigma_Y = 200$ MPa $Rp_{0.2}$).

5.5.2 Relationship between the cutting force and R_a

The results show that although optimal R_a values are obtained in a low F_c zone, the best R_a is not obtained at the lowest F_c, both in dry and lubricated regimes. This follows from the previous analysis as well as from the hypothesis regarding the dependence of R_a on a_p and *f*. The lowest F_c are obtained at a_p = 0.5 mm, which is the region where deflection is largest (recall eq. 5.17). and therefore, according to the hypothesis in eq. 5.21, R_a is degraded. This also means, under the developed hypothesis, that the true a_p is lower than 0.5 mm.

On the other hand, in light of the previous analysis of F_c, since a_p is lower than the expected, the chip thickness b in fig. 5.18 is lower, which in turn decreases the contribution of dU_c to dU_{ext}, or equivalently, decreases F_c.

Closing thoughts on the cutting forces

With respect to the reviewed works which measured the cutting forces,

Source	F_c *(N)*	R_a *(μm)*	*f(μm/rev.)*	k_s $\left(\frac{N}{mm^2}\right)$
[8]	0.013	$\ll 1$	0.012	$\sim$ 3000
[15] [16]	~ 1	0.1	3	-
[24]	3.59	0.055	1	-
This work	13.93	0.240	10	1219

Table 5.15: Comparison between this work and reviewed literature: cutting force @ optimal R_a

this work is on the extreme end of experienced cutting forces during micro-turning. A direct comparison of F_c and k_s can't be established since the specific alloy of brass used in these works is not the same of this thesis.

However, as a general remark, if we define the macro-turning regime as one where the term dU_d is the major contributor to dU_{ext} in eq.5.27, then this work seems to be positioned below it. According to [19], such macro-turning regime can be bounded near $f \sim 0.5 - 1$ mm/rev. (refer to fig.5.19) since $k_s \sim$ 600 - 500 MPa , which is roughly the same order of magnitude of σ_Y.

Throughout this document "micro-turning" was used to refer to this work merely due to the dimensions of the obtained pins. While at first sight, if we redefine micro-turning as a regime where the term dU_c is the major contributor to dU_{ext} in eq. 5.27, it might be tempting to describe the process taking place

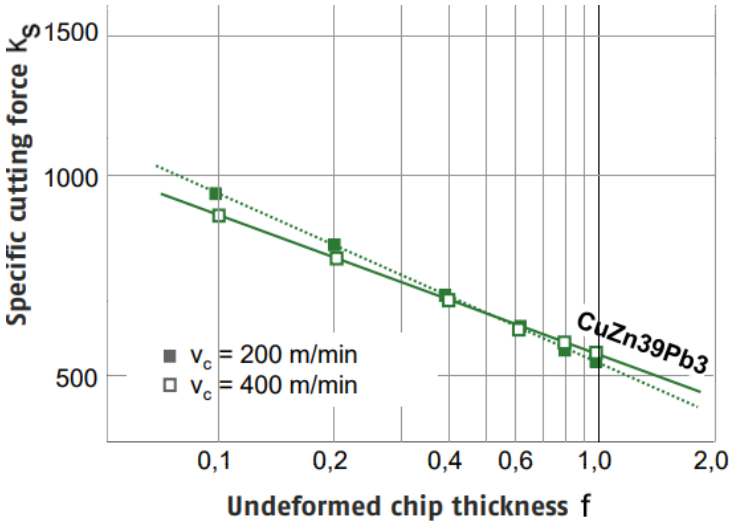

Figure 5.19: Evolution of k_s with f (r_b = 0.4 mm and a_p = 1 mm), adapted from [19]

as micro-turning (since the maximum $k_s = 1571$ MPa is around an order of magnitude greater than σ_Y), in [8] a value of $\mathbf{k_s}$ ***= 14000 MPa*** was obtained for extremely low values of f and a_p. Therefore, while the fabricated pins were quite small, this work appears to slot well between the micro and macro-turning regimes, with significant contributions from both dU_d and dU_c to dU_{ext}.

5.5.3 Radial force signature

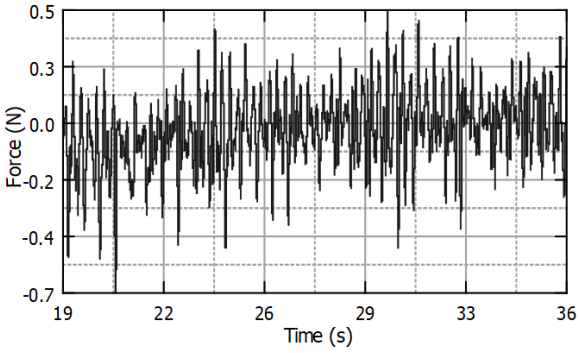

Figure 5.20: Radial force hovering around zero

Although in section 7.2.1 and 7.2.2, the radial force measured with the dynamometer was used to calculate the theoretical deflections, results were presented because the contribution of this force to the error in the micro-pin diameter is low.

In the optimal operating zone (recall fig. 4.3), some of the calculated average radial forces were very close to zero, although is is quite difficult to analyze and determine its direction or its absolute magnitude, due to the high frequency transients around zero. Therefore, it was quite complicated to extract any useful information from these experimental measurements.

6 Conclusion and future work

The existing 5 axis machining centre was successfully improved with a mechanical redesign and with the deployment of a modern CNC controller and electronics framework. An attempt was made to manufacture micro-pins with similar criteria as those used in balance staves for the watchmaking industry. While it proved possible to generate micro-pins by turning operations with a diameter that approached those typical of these parts, and that complied with $R_a < 0.4\ \mu m$, it was neither possible to guarantee the desired h4 tolerance nor reach $R_a < 0.1\ \mu m$. Two hypotheses were developed to try to explain the dependence of R_a on the operating factors. Using the available data, a factorial regression was performed to check what operating factors predicted better R_a, the result of which agreed well with the proposed hypotheses.

This work merits from further experiments, since **(i)** the micro-pins fabricated were much longer than balance staff pivots and therefore, according to the developed hypotheses, at shorter lengths, R_a should improve; **(ii)** the operating region is one where vibration is an important mechanism which degrades R_a according to the developed hypotheses.

These results are characteristic of the developed machine, the dimensions and geometry of the micro-pins, the tool used and the operating parameters. While manufacturers may establish that cutting tools are suitable for certain types of operations, with a wide range of operating parameters, without testing these on a particular machine, little can be expected. Therefore, although the mechanical redesign generated positive results, some future work opportunities can be identified which should be pursued if the machining centre is to perform micro-turning operations while holding tighter tolerances than those obtained during the micro-pin trials: **(i)** improve the dynamometer - X axis guide mounting configuration so that its stiffness is increased or, if there is no necessity of capturing process forces, do away with it and mount the toolholder directly into the X axis guide; **(ii)** regarding the kinematic precision and accuracy of the machine, at present time two outcomes can be envisioned for the machine. First, if the linear guideways are to be maintained, an overall refurbishment must be done to them to bring the utmost accuracy necessary for the small, precise and delicate work that the machine has the potential to do. The rigorous procedure is as follows: the machine should be stripped down to bare components. The base of the machine should have the X and Z planes checked for parallelism and corrected if needed. Afterwards, the hardened steel guideways should be mounted and this assembly should be mounted on its three mounting points on the table of a 5-axis jig grinding machine. All surfaces of the guideways can then be ground flat, parallel and square, producing an accurate base, which serves as the master for the next operations. Next, each carriage must be checked against the master rails, and scrapped or ground to make sure an high contact area between them and the guideways is produced. Another possibility is to virtually position (i.e, through means of a jig position it such that it floats with a small

clearance) the carriage such that it is parallel and square with the master guideway. Next, a replicating low friction material is injected, which when hardened replicates the surface of the master rail perfectly. The carriages are now aligned. Next the headstock is assembled and aligned such that its rotation axis is parallel to the X-axis. Next, the Y stage is adjusted for squareness with the headstock.

The better course of action is however to replace the sliding contact guideways with linear guideways with ball or roller bearings. This produces a machine with far better repeatability, less wear, virtually no maintenance and higher achievable accelerations and speeds (also far lower than the 5 mm/min now possible). To do so, the hardened steel guideway would be substituted by similar steel way with bolt patterns where the guideways would bolt on to. These should then be milled flat on a milling machine, and an accurate shoulder can be produced directly, to which the master rail would be clamped to. This guarantees straightness of the axes. The carriages would suffer minor modifications, where its bottom part would be milled off, resulting in a flat surface, which can be made parallel to the top surface easily. The bolt patterns of the bearing trucks would be drilled in the same milling operation; **(iii)** The headstock design should also be revised. Currently, due to the integrated motor and inferior cooling design, it cannot remove the heat produce directly into the spindle shaft. This means that during continuous operation, there is significant thermal expansion of the spindle, with detrimental effect on the accuracy achievable during a production or testing run. A simple idea is to remove the armature, lightening the spindle shaft, and mounting a pulley at its back. A small but an higher speed motor could then be mounted on top of the headstock, where a conveniently placed v-slot already exists. This would remove all the heat load from inside the casting from where, as it now stands, it cannot escape. The bearings should be removed and cleaned of excess grease, remounted and a small grinding spindle should be assembled in the fourth axis, where it can be indexed at the required cone angle to regrind the spindle W20 cone, to produce the most accurate mating surface for the collets. These should also be upgraded. Schaublin, the manufacturer, sells ultra precision (UP) variants, which should improve the runout error immensely.

In regards to the control and electronic framework, some future opportunities are also identified: **(i)** the electronic structure of the machine, although relatively cheap to implement, brings significant challenges. The communication standard, although digital, implies the use of multiple lines of communication, which need to be carefully laid out to prevent unwanted interference. The case of analog signals from sensors is even worse. Future maintenance is therefore dependent on the level of familiarity on the standards used and the availability of replacement parts. It makes sense therefore to do away with all the required intermediate hardware platforms, and move to a pure software solution. The best solution is to use a fieldbus network, through which all the signals flow, from controller to node, in digital format. ETHERCAT, the highest performance of these, is readily adaptable to LinuxCNC, and could mean that a similar configuration for this machine could be made only with four ETHERCAT-enabled servo amplifiers. This is possible since ETHERCAT can run on normal Ethernet infrastructure, and cabling is reduced to one communication line. With an upgrade to absolute encoders, even homing sensors could be eliminated and a purely digital implementation realized. Compared to the existing electronic framework, which requires 8 communication lines per servo amplifier, 3 lines per homing sensor and 1 line for the emergency button, for a total of 45 lines, the ETHERCAT solution only requires 1 communication line for all amplifiers

and sensors, plus 1 line for the emergency button, for a total of 2 lines.

This simpler solution is only offset by its high initial cost: a good Ethercat-enabled servo amplifier commands premium prices, over five times the cost of the servo amplifier used in this project. The cost of an Ethercat project, including the use of absolute encoders, would have been about five to ten times this project cost, which is somewhat prohibitive given the usage of the machine.

(ii) More importantly, the encoders resolution should be improved, and ideally a linear encoder should be included in each linear axis of the kinematic chain. As was verified during the micro-pin trials, most of the uncertainty in their final diameter is due to the lack of accuracy of the X axis stemming from the lack of resolution of the X encoder.

This thesis served as a great learning experience. Simultaneously to the thesis work, I had the opportunity to work in NOF, where I had access to conventional and CNC machine tools. All of the mechanical work for my thesis, with regards to part manufacturing, was done by me with the help of some colleagues, using the machines of NOF. This helped me greatly in gaining some sensibility to understating how hard things are to make and how much time it takes to bring them to the required tolerances. My initial idea, when I started this thesis, was that I would use it as a learning step to build my own machine to manufacture these parts. While I was certain, at the start of the work, that it would be possible to machine these types of parts with the strict quality requirements, using turning operations, this experience changed many of my views on this subject.

While it may be possible, albeit at great cost, the smarter approach to produce these types of parts is not to force the technology to achieve the desired results, but to think outside the box: how can these parts be modified to suit the many different technologies available. Watchmaking technique is deep rooted in century long history of advancements and knowledge which did not always accompany scientific advancements. While it might have been true that traditional machining techniques (turning, milling, etc...) were the best (really, the only) processes available a century ago, today it is not so. The manufacture of small parts, while maintaining the same relative ratio of part size/accuracy of macroscopic parts, requires a much higher degree of resolution, accuracy and control than those typically encountered in conventional technology. Non-conventional technology, such as electrical discharge machining (EDM), electrochemical machining (ECM), photo-chemical machining (PCM), laser assisted chemical etching (LACE), photolithography and electroforming are all examples of highly technological, high added value processes which can produce parts in many kinds of materials (even those were conventional techniques fail to work on, such as super-hard alloys, ceramics and semiconductors for instance) with increased resolution and improved surface finishes without any forces applied to the parts.

At the end of my thesis, my focus has shifted from trying to develop a conventional machine to produce the small parts needed for a watch, to exploring the potential these technologies have to produce these kind of parts. By the end of this new journey, hopefully not only will I have had success in producing these small and precise parts (and potentially a watch) but also, as a consequence, ended up producing a unique machine and/or process, one which can be applied to other areas which share similar requisites.

A Appendix

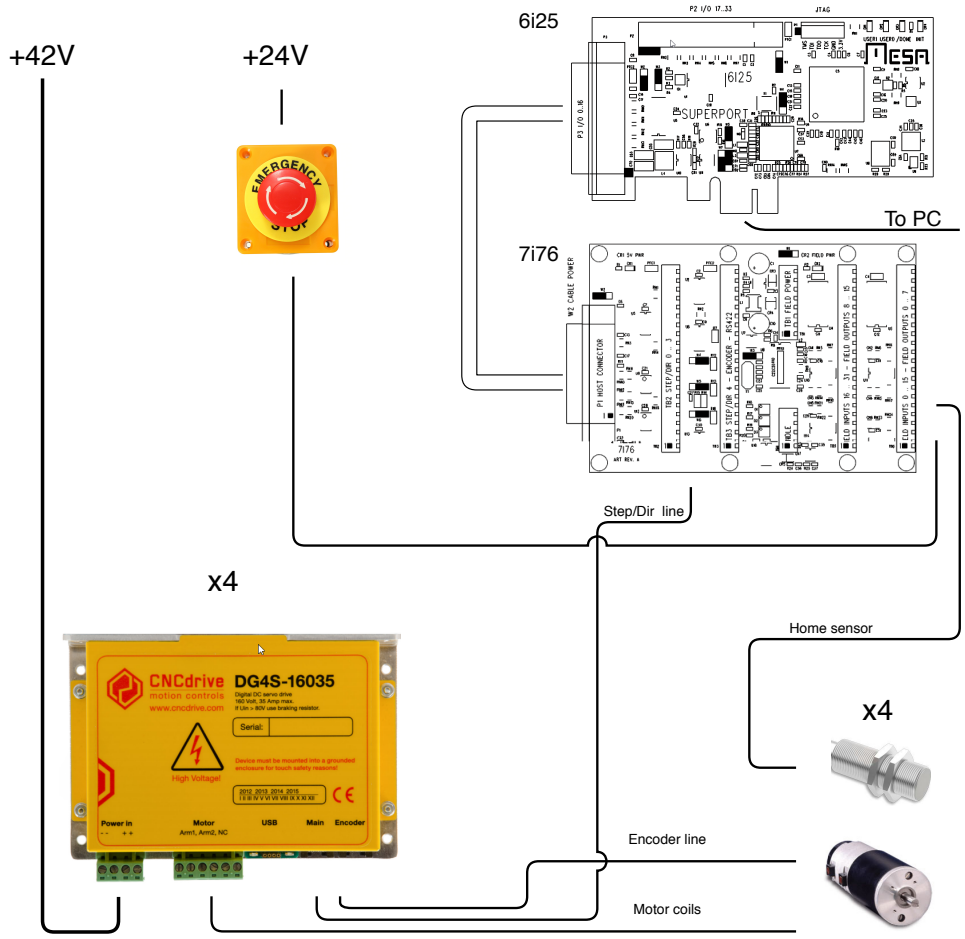

Figure A.1: Simplified schematic CNC control

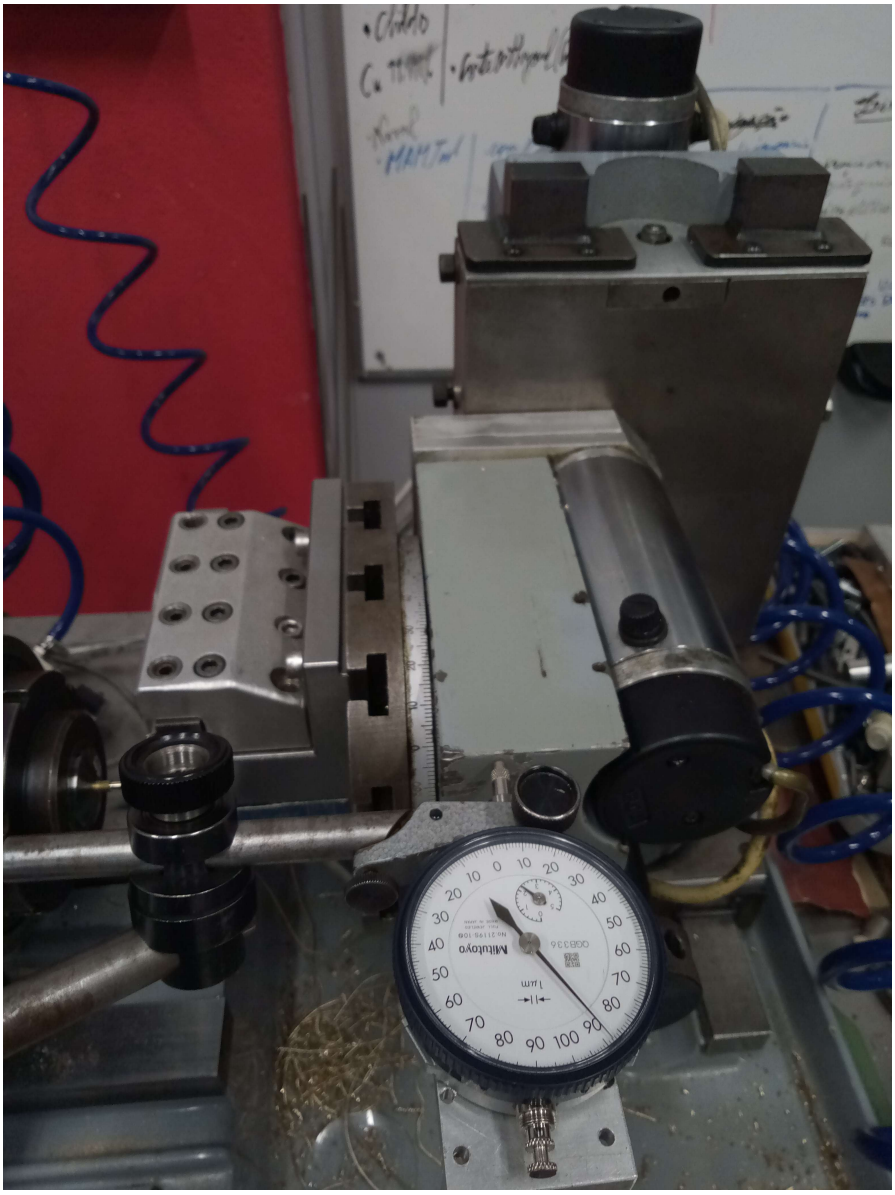

Figure A.2: Setup for X-axis accuracy measurement

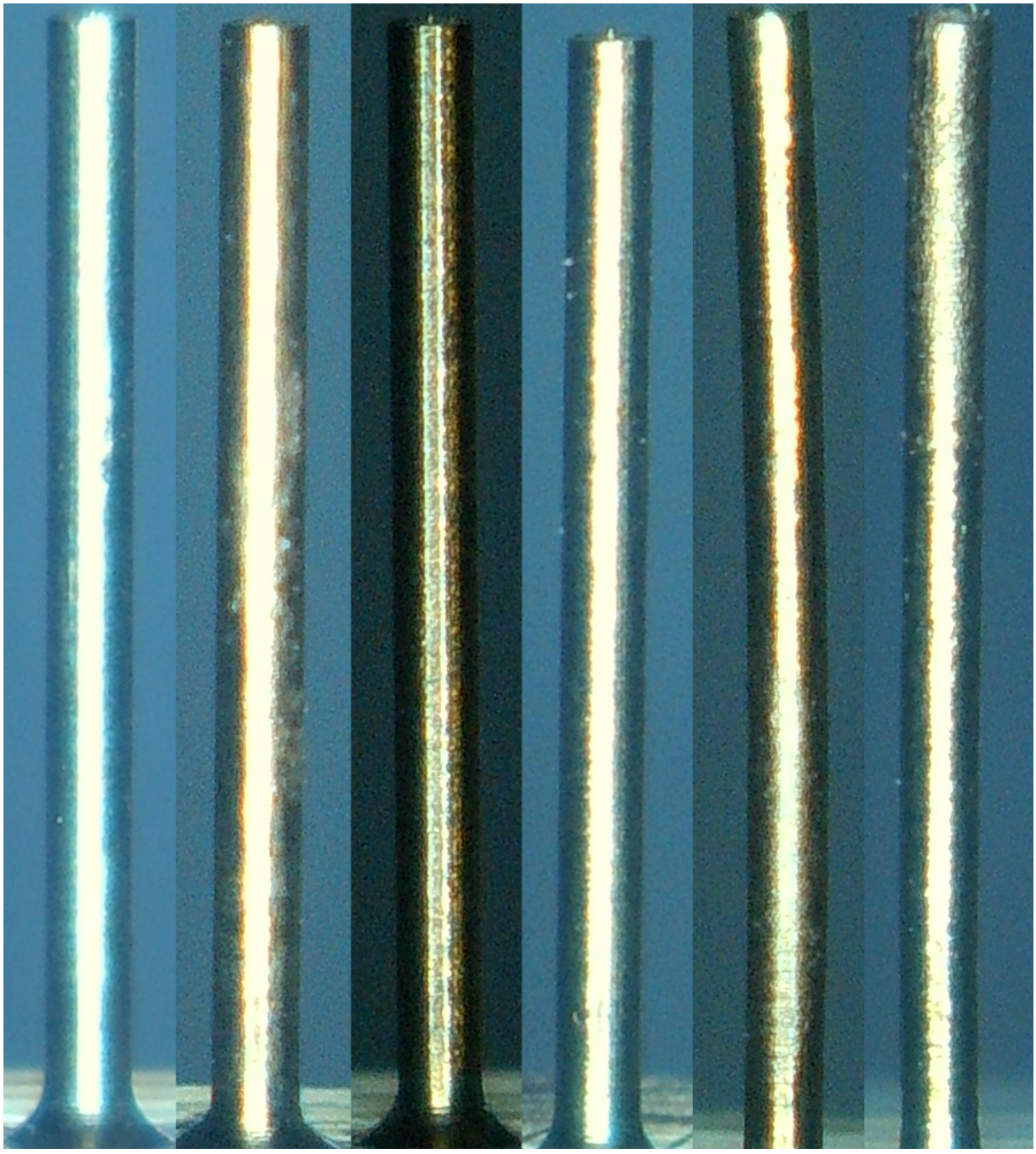

Figure A.3: f = 0.005 mm/rev.: From left to right, a_p increases

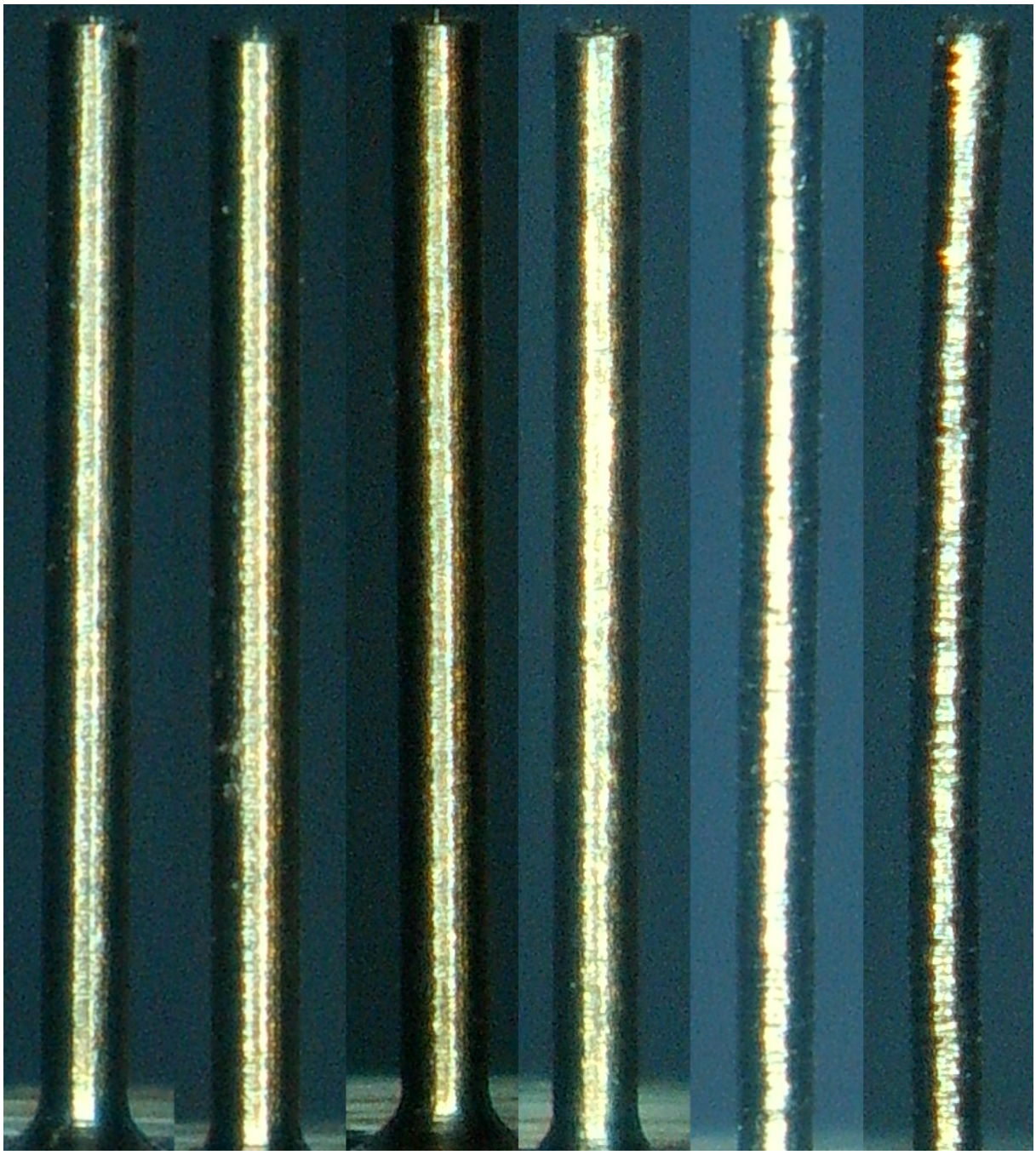

Figure A.4: f = 0.010 mm/rev.: From left to right, a_p increases

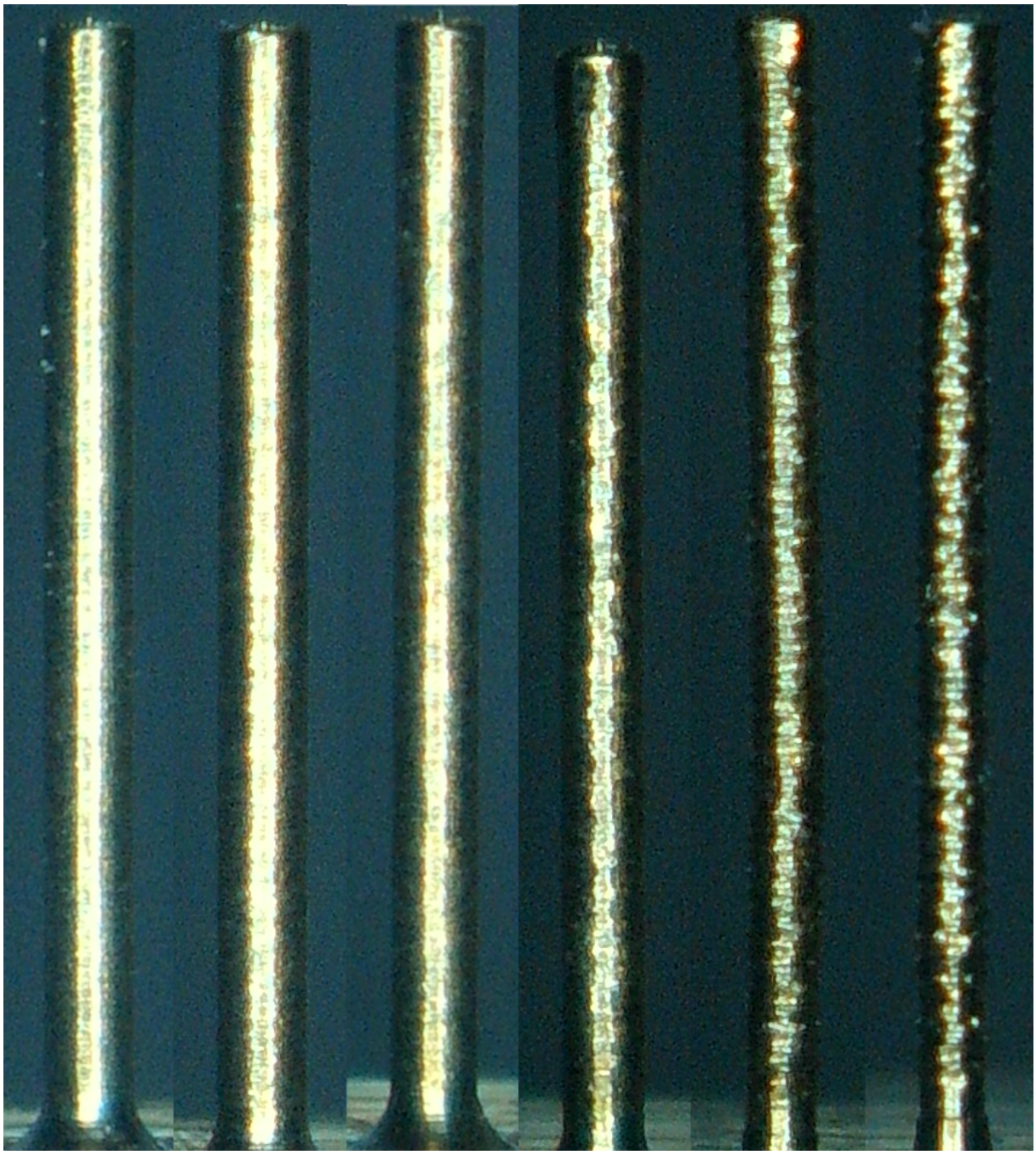

Figure A.5: f = 0.020 mm/rev.: From left to right, a_p increases

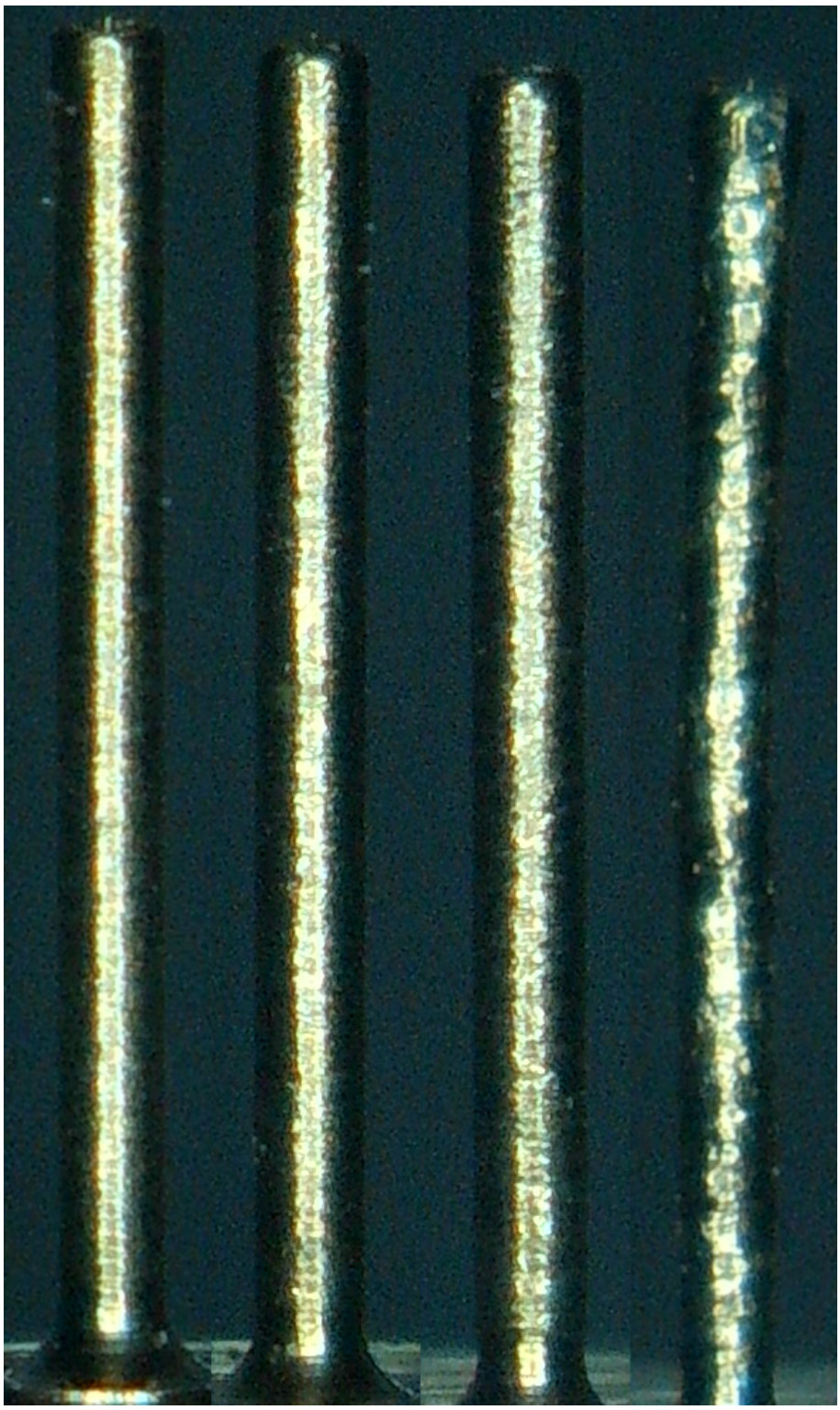

Figure A.6: f = 0.040 mm/rev.: From left to right, a_p increases

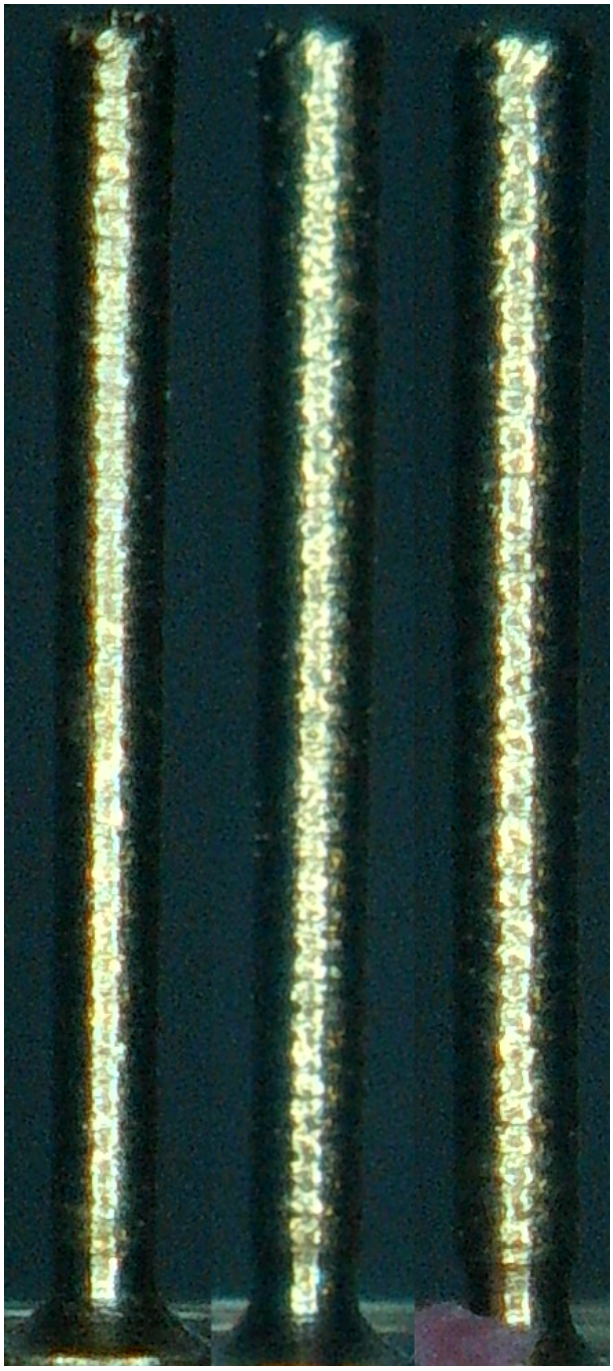

Figure A.7: f = 0.080 mm/rev.: From left to right, a_p increases

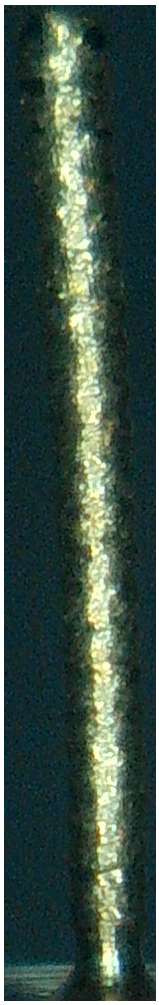

Figure A.8: f = 0.160 mm/rev.: a_p = 0.9 mm

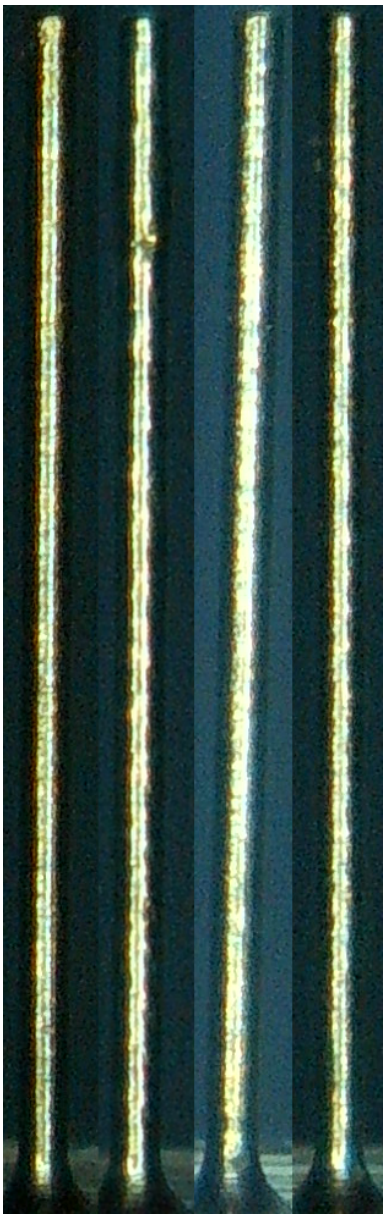

Figure A.9: Two most left: a_p = 0.5 mm, f = 0.005 mm/rev. to f = 0.010 mm/rev.; Two most right, a_p = 0.9 mm, f = 0.005 mm/rev. to f = 0.010 mm/rev.

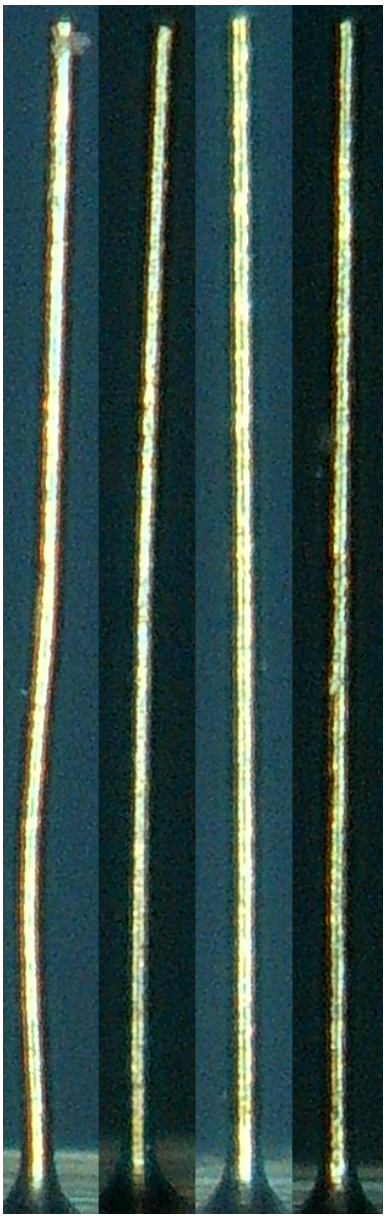

Figure A.10: Two most left: a_p = 0.5 mm, f = 0.005 mm/rev. to f = 0.010 mm/rev.; Two most right, a_p = 0.9 mm, f = 0.005 mm/rev. to f = 0.010 mm/rev.

Bibliography

[1] ASME. *ASME Engineering Landmark 123, Kingsbury Thrust Bearing*. 1987. URL: https://www.asme.org/wwwasmeorg/media/resourcefiles/aboutasme/who%5C%20we%5C%20are/engineering%5C%20history/landmarks/123-kingsbury-thrust-bearing-1911.pdf.

[2] Paul Baillio. *Jewel Bearings Solve Light Load Problems*. 2020. URL: http://cdn.thomasnet.com/ccp/00400419/38874.pdf.

[3] George Daniels. *Watchmaking*. A6 Salem Road London W2 4BU: Philip Wilson Publishers, 2014.

[4] Tony Griffiths. *Watchmaker lathes*. 2020. URL: http://www.lathes.co.uk/watchmaker/.

[5] Tornos Group. *SwissNano - Axle*. 2014. URL: https://youtu.be/D1xwDbUKH6A?t=17.

[6] Barnes Industries Inc. *How a Ball Screw Works*. 2020. URL: http://www.barnesballscrew.com/how-a-ball-screw-works/.

[7] S.P. Leo Kumar. "Measurement and uncertainty analysis of surface roughness and material removal rate in micro turning operation and process parameters optimization". In: *Measurement* 140 (2019), pp. 538–547.

[8] Zinan Lu and T. Yoneyama. "Micro cutting in the micro lathe turning system". In: *International Journal of Machine Tools and Manufacture* 39 (1999), pp. 1171–1183.

[9] Munira Lutfi et al. "Surface Roughness and Machining Accuracy when Micro-Turning Copper". In: vol. 76-78. 2009, pp. 532–537.

[10] Wivia Machinery. *Double Y axis Swiss Type CNC lathe W208*. 2020. URL: http://www.wiviamachinery.com.tw/double-y-axis-swiss-turn-machine-W208-8p.html/.

[11] MechaniCalc. *Beam Deflection Tables*. 2020. URL: https://mechanicalc.com/reference/beam-deflection-tables.

[12] Newport. *Motion Basics Terminology Standards*. 2020. URL: https://www.newport.com/n/motion-basics-terminology-and-standards.

[13] Brian O'Connor and Byron Fruit. *Minimum Incremental Motion and Holding Stability in Beamline Positioning*. Tech. rep. Aerotech Inc., 2020.

[14] Y. Okazaki and T. Kitahara. "Development and Evaluation of a Micro-Lathe Equipped with Numerical Control." In: *Journal of The Japan Society for Precision Engineering* 67 (2001), pp. 1878–1883.

[15] M. Rahman, A. Kumar, and H. Lim. "CNC microturning: an application to miniaturization". In: *International Journal of Machine Tools and Manufacture* 45 (2005), pp. 631–639.

[16] M. Rahman et al. “Development of micropin fabrication process using tool based micromachining”. In: *The International Journal of Advanced Manufacturing Technology* 27 (2006), pp. 939–944.

[17] Mohammad Azizur Rahman et al. “Effect of cutting edge radius on ’burnishing-like’ mechanism in micromachining”. In: *International Journal of Precision Technology* 8 (2018), p. 85.

[18] Renishaw. *VIONiC incremental encoder system with RESM20 rotary (angle) ring*. 2020. URL: https://www.renishaw.com/en/vionic-incremental-encoder-system-with-resm20-rotary-angle-ring--38324.

[19] WZL at RWTH Aachen University. *Recommended machining parameters for copper and copper alloys*. Am Bonneshof 5, 40474 Düsseldorf, Germany: Deutsches Kupferinstitut, 2010.

[20] Sandvik. *How to choose correct turning insert*. 2020. URL: https://www.sandvik.coromant.com/en-us/knowledge/general-turning/pages/how-to-choose-correct-turning-insert.aspx.

[21] TimeZone Watch School. *The Wheel Train*. 2020. URL: https://www.timezonewatchschool.com/WatchSchool/Glossary/Glossary%5C%20-%5C%20Wheels/glossary%5C%20-%5C%20wheels.shtml.

[22] TimeZone Watch School. *Watchmaking: cylindrical and conical pivots*. 2020. URL: https://https://www.timezonewatchschool.com/WatchSchool/Glossary/Glossary%5C%20-%5C%20Wheels/Glossary%5C%20-%5C%20Wheels%5C%20-%5C%20Jewel%5C%20Coni/glossary%5C%20-%5C%20wheels%5C%20-%5C%20jewel%5C%20coni.shtml.

[23] Bill Schweber. *Don’t Ignore the Humble Brushed DC Motor*. 2020. URL: https://pt.mouser.com/applications/dont-ignore-the-brushed-dc-motor/.

[24] Surinder Singh et al. “Effect of machining parameters on cutting force during micro-turning of a brass rod”. In: *Materials and Manufacturing Processes* 34.16 (2019), pp. 1816–1823.

[25] Alexander H. Slocum. *Precision Machine Design*. Pearson, 1992.

[26] Proteo SNC. *Manuale Provvisorio Per L’uso e la Manutenzione*. Via Lughese, 161 47010 Forli, 1993.

[27] Sumitool. *Insert Grades A1 to A38*. Sumitool, 2020.

[28] THK. *Ballscrew General Catalogue 511E*. THK, 2020.

[29] THK. *General Catalogue Support Book 512E*. THK, 2020.

[30] Hembrug Machine Tools. *Ultra Precision Hard Turning Machines*. Brochure. 2017. URL: http://www.mungermachinetool.com/PDF/Turning%5C%20Milling/Hembrug%5C%20website_Final_2017.pdf.

[31] J. G. Williams and Y. Patel. “Fundamentals of cutting”. In: *Interface Focus* 6.3 (2016).